Surface Engineering Using Layer-by-Layer Assembly of pH-Sensitive Polymers and Nanoparticles

by

DAEYEON LEE

Bachelor of Science, Chemical Engineering
Seoul National University, Seoul, Republic of Korea, 2001

SUBMITTED TO THE DEPARTMENT OF CHEMICAL ENGINEERING
IN PARTIAL FULFUILLMENT OF THE REQUIREMENTS FOR THE DEGREE OF

DOCTOR OF PHILOSOPHY IN CHEMICAL ENGINEERING
AT THE
MASSACHUSETTS INSTITUTE OF TECHNOLOGY
FEBRUARY, 2007

Signature of Author: _____
Department of Chemical Engineering
January 29, 2007

Certified by: _____
Robert E. Cohen
St. Laurent Professor of Chemical Engineering
Thesis Advisor

Certified by: _____
Michael F. Rubner
TDK Professor of Materials Science and Engineering
Thesis Advisor

Accepted by: _____
William M. Deen
Professor of Chemical Engineering
Chairman, Committee for Graduate Student

Surface Engineering Using Layer-by-Layer Assembly of pH-Sensitive Polymers and Nanoparticles

by

Daeyeon Lee

Submitted to the Department of Chemical Engineering

on January 29, 2007 in Partial Fullfilment of the

Requirements for the Degree of Doctor of Philosophy in

Chemical Engineering

Abstract

Surface engineering of a variety of materials including colloidal particles and porous membranes has been achieved by using layer-by-layer assembly of pH-sensitive polymers and nanoparticles. In the first part of this thesis, hydrogen-bonded multilayer coatings comprising poly(acrylic acid) and polyacrylamide were used to functionalize spherical colloidal particles. Multilayer-modified colloids showed an excellent resistance to cell adhesion. Hydrogen-bonded multilayer coatings on microspheres also could be utilized as templates for in situ nanoparticle synthesis enabling the formation of nanoparticle-loaded hollow microcapsules. Silver nanoparticle-loaded multilayer coatings were created on magnetic microspheres to create antibacterial agents that can be manipulated using a magnetic field. In the second part, the surfaces of track-etched polycarbonate membranes were functionalized with multilayer coatings that undergo discontinuous swelling transition. Multilayers comprising poly(allylamine hydrochloride) and poly(styrene sulfonate) were deposited at a high pH condition (pH > 9.0). These multilayer-modified membranes exhibited hysteretic gating behavior that could be useful for the separation of pH-sensitive materials such as proteins. The growth and swelling behavior of the multilayers in the cylindrical pores of TEPC membranes were also investigated. Heterostructured magnetic nanotubes could be created by further modifying the multilayer-coated TEPC membranes. These magnetic nanotubes were utilized for the separation and controlled release of anionic molecules including active pharmaceutical ingredients. In the last part of this thesis, all-nanoparticle thin film coatings were created by sequentially depositing oppositely charged nanoparticles. The fundamental investigation of all-nanoparticle multilayers revealed that a narrow processing window exists in which multilayers of oppositely charged nanoparticles can be assembled in a true layer-by-layer manner. It was also demonstrated that structure and properties of all-nanoparticle thin films could be varied by controlling the assembly conditions. All-nanoparticle thin film coatings consisting of titanium oxide and silica nanoparticles exhibited potentially useful antifogging, antireflection and self-cleaning properties.

Thesis Supervisors: Robert E. Cohen, St. Laurent Professor of Chemical Engineering

Michael F. Rubner, TDK Professor of Materials Science and Engineering

Acknowledgements

I could literally devote an entire chapter to acknowledge and thank numerous individuals who have made this thesis a reality. First and foremost, I thank my two research advisors, Professors Robert E. Cohen and Michael F. Rubner. I consider myself extremely fortunate to be a part of this collaborative effort. Their enthusiasm and excitement about new ideas have motivated me to think outside the box and develop research topics that I could truly enjoy working on. The different and often complementing characteristics of the two advisors have shown me the importance of working in a team-environment. Both of them have also been true mentors who have guided me through the difficult times that I faced during my study. I could not have asked for more from my advisors and am not hesitant to say that I would make the same decision to work for these two if I were to start my doctoral study all over again (of course, assuming that they would also take me as their student).

I would also like to thank my thesis committee members, Professors Paula T. Hammond and T. Alan Hatton for their time and constructive input. I have greatly benefited from interactions with Professor Hammond and her students/post docs on various aspects of my research projects. Professor Hatton has always brought a different perspective to my research with his expertise on transport phenomena and colloid science and has generously given me access to some important characterization tools in his lab.

One of the major reasons I decided to pursue a doctoral degree in the US was the encouragement and motivation of my undergraduate advisor, Professor Kookheon Char of Seoul National University. His philosophy on research and life has driven me to search for an interesting problem that no one has thought about.

I would also like to express my gratitude to my fellow group members with whom I have fully enjoyed interaction and from whom I have learned so much. I would like to thank Jeri'Ann Hiller, Jeff Abes, Yonathan Thio, Ed Kopesky, Prem Pavoor, Roger Aronow, Heejae Kim, Michelle Poliskie, Mike Berg, Jeeyoung Choi, Nobuaki Takane, Sung Yun Yang, Adam Nolte, Koji Itano, Toshi Takasaki, Hyunku Ahn, Lei Zhai, Zhizhong Wu, Xiaoxia Sheng, Jimmy Li, Zhi Li, Fevzi Çebeci, Javier Bravo, Ryan Bennett, Ben Wang, Sharon Soong, Andy Miller, Solar Olugebefola, Jenny Lichter, Zekeriyya Gemici, Al Swiston, Gary Chia, Erik Williamson, Marisa Beppu, Giovanna Machado, and Ray Turner. In particular, I would like to mention Adam Nolte with whom I have spent a lot of time arguing and discussing about different aspects of each other's research projects. I have thoroughly benefited from his expertise on subjects ranging from optics to numerical calculations. I will cherish the friendship that I have developed with Adam for years to come.

I have been extremely fortunate to have the opportunities to work with some of the brightest undergraduate students at MIT and visiting researchers. These include Allison Kunz, Damali Omolade, Leah Dancy, Emily Gullotti, and Megan Sherkow. They have been instrumental in a number of research projects that I have conducted. Special thanks goes out to Allison who has worked with me on several topics since her freshman year at MIT and Damali who was extremely enthusiastic and productive on projects that had nothing to do with her major, which happens to be psychology.

Without the existence of the so-called "Korean Mafia", my life at MIT would have been nothing but monotonic. In particular, I thank the PPST Korean connection: Heejae Kim for his help during my

early and struggling years in the lab, Jongseung Yoon for having all the answers to my questions regarding transmission electron microscopy, Juhyun Park for sharing his expertise on polyelectrolyte multilayers, and Junsang Doh for providing his insightful comments/suggestions on my research. Heejae, Juhyun and Junsang, especially, were always available to share the difficulties and joys of graduate life at MIT. Sunyoung Lee of Prof. Van Vliet's group has provided much needed help with atomic force microscopy.

The staff at the Shared Experimental Facilities of the Center for Materials Science and Engineering has provided crucial technical supports, making it possible to make important progress in my research. Mike Frongillo, Anthony Garratt-Reed, Libby Shaw, Tim McClure, and Patrick Boisvert were indispensable resources to discuss any problems with various characterization techniques. I also appreciate the administrative support of Greg Sands of PPST, Stephanie Hansen, Karyn Jones, Danielle Delgado and Carrie Casado. I thank my collaborators, Professor Jongyoon Han and his students, Hongchul Jang, Ying-Chih Wang, and Pan Mao, for introducing me to the world of microfluidics in recent years.

Most importantly, I thank my family for their unconditional love and support. I am not sure if I can find words to describe how grateful I am to my wife, Sunhee Jeon. She has shown me the true meaning of love and sacrifice. Like one baseball player said, I consider myself the luckiest man on the face of the earth to have Sunhee by my side. My daughter, Amy Eumin Lee, has given me happiness that I have never experienced before. Her smile would instantly light up my spirit no matter how bad things were going in life. I also appreciate the support and love of my parents, and parents-in-law. Without their love and support, it would not have been possible to start my study at MIT, let alone finish it.

Financial support of the research projects described in this thesis was provided by the MRSEC Program of the National Science Foundation and the DuPont-MIT Alliance.

Table of Contents

List of Figures

List of Tables

Chapter 1
Introduction

1.1 Surface Engineering

Surface engineering can be described as an enabling technology.[1] Rather than designing a material with discrete bulk and surface properties suitable for specific applications, it is often more efficient and desirable to create one that has appropriate bulk properties, and subsequently modify its surface with films or coatings that provide enhanced surface properties and functionalities. In many instances, however, advances in science and technologies are being constrained by surface requirements that cannot be readily satisfied. In this respect, the ability to precisely control and tune the surface properties of materials using simple means is extremely important.

Traditionally, surface engineering of materials has focused on improving the tribological and wear resistance of materials and also the corrosion resistance using protective coatings.[1] However, recent advances in bio- and nanotechnology have enabled and also demanded the creation of functional surfaces and coatings that are potentially useful in advanced fields including energy, biomedical, and microelectronics applications. Some examples of functional coatings include biocompatible coatings that enable the use of medical implants *in vivo*[2], antimicrobial coatings for medical purposes[3], and superhydrophobic coatings to control the wettability of fabrics[4-6].

Beyond improving the functionality of an existing material, surface engineering today offers opportunities in creating novel materials which could not be readily prepared using conventional synthetic schemes. Complex structures can be deposited onto surfaces enabling the utilization of coated materials in novel applications. For example, heterostructured thin films on polymer substrates have been heavily studied as means to produce flexible display devices[7,8], optical filters[9], and photonic band gap materials[10,11].

1.2 Surface Engineering Methodologies

A number of methods to modify and functionalize the surface of different materials have been developed. Ideally, a process should be easy and simple to implement onto surfaces with different chemistry and shapes, and also should be reliable and robust. In many cases, achieving uniformity and precise control over surface properties is extremely important but also challenging. Table 1.1 summarizes and compares the advantages and disadvantages of widely utilized surface engineering methods. While each technique has its own unique set of advantages, every method has drawbacks making it difficult to utilize one particular method as a universal means of surface engineering.

Table 1.1. Comparison of surface engineering methods.

Methods	Advantages	Disadvantages
Self-assembled monolayers (SAM)[12]	• Desired properties can be readily obtained with molecularly thin layers (typically < 2 nm)	• Often requires a specific type of surfaces such as Au; not compatible with many processes • Poor thermal stability of thiol compounds on Au surfaces
Chemical vapor deposition (CVD)[13]	• Solventless process • Environmentally friendly; no effluents or pollutants produced	• Requires high-cost vacuum apparatus • Difficult to extended to colloidal particles or porous materials
Surface grafting[14]	• High molecular weight polymers can be deposited onto surfaces • Covalent attachment of gaft chains; excellent adhesion and chemical stability	• Difficult to apply to confined geometries (e.g., high aspect ratio pores) • Usually requires surface functional groups
Langmuir-Blodgett (LB) technique[15]	• High uniformity with low defect density • Films with molecular thickness can be readily deposited	• Often tedious and time-consuming • Limited to macroscopically planar substrates

1.3 Layer-by-Layer Assembly

1.3.1 Multilayer Thin Films via Layer-by-Layer Assembly

Layer-by-Layer (LbL) assembly provides a versatile means to create multilayer thin films with a wide range of properties.[16-18] The LbL deposition technique involves the sequential adsorption of two materials that interact with each other through different types of intermolecular interactions including electrostatic attraction and hydrogen bonding. As shown in Figure 1.1, a substrate is alternately exposed to solutions containing oppositely charged species (polyelectrolytes are shown as example in Figure 1.1). Each deposition step leads to the spontaneous adsorption of materials and the charge reversal of the multilayer surface allowing the next layer of materials to be deposited through electrostatic interactions.[19-21] While deposition steps are usually achieved by dipping a substrate into each solution, other methods including spin coating[22,23] and spraying methods[24,25] also have been explored.

The LbL processing is an extremely versatile surface engineering tool which addresses a number of shortcomings of other surface modification techniques described above. Most of all, the technique is simple and easy. The structure and properties of multilayer thin films can be precisely controlled by varying the assembly conditions such as ionic strength and pH of each solution. In addition, a variety of materials can be readily incorporated into multilayer thin films including natural and synthetic polymers, nanoparticles, DNA, proteins and multivalent ions.[17] LbL technique is not limited to surfaces that exhibit specific chemical functionalities and also can be extended to create conformal coatings on non-planar geometries including colloidal particles[26,27], porous membranes[28-32], fibers[33,34] and living cells[35,36]. It should be noted that despite the prevalent usage of the term "multilayer", LbL assembled films do not exhibit stratified structures but rather

homogenous structures (resembling well blended polymer films without any phase separation) due to the copious interpenetration of polymer chains in the films as illustrated in Figure 1.1[16].

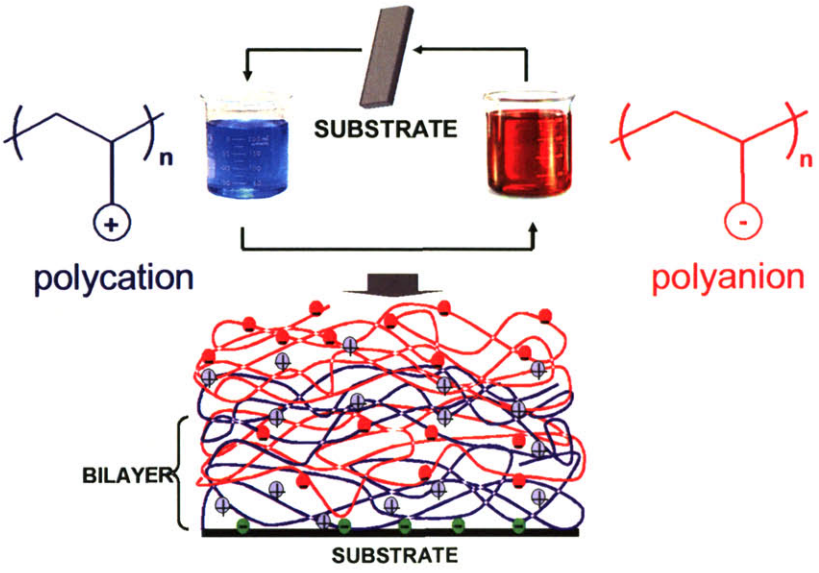

Figure 1.1. Schematic showing the fabrication of layer-by-layer deposition of oppositely charged polyelectrolytes. A bilayer denotes a pair of oppositely charged species (i.e., polyelectrolytes).

1.3.2 Weak Polyelectrolyte Multilayers

1.3.2.1 Weak Polyelectrolytes

Polyelectrolytes can be classified into two categories depending on their tendency to change their degree of ionization as a function of solution pH. While strong polyelectrolytes remains fully charged independent of pH, the degree of ionization of weak polyelectrolytes is highly sensitive to the solution pH.[37] The molecular structures of widely studied weak polyelectrolytes – poly(acrylic acid) (PAA) and poly(allylamine hydrochloride) (PAH) - are shown in Figure 1.2.

poly(acrylic acid) poly(allylamine hydrochloride)

Figure 1.2. Molecular structure of widely studied weak polyelectrolytes. poly(acrylic acid) (PAA) (left) and poly(allylamine hydrochloride) (PAH) (right).

The Henderson-Hasselbach equation modified to account for polyelectrolytes describes the relationship between pH of solution and the degree of ionization[38]:

$$pH = pK_0 + \log\left(\frac{\alpha}{1-\alpha}\right) + 0.434\left[\Delta Fe(\alpha, C_s)/RT\right] \qquad (1.1)$$

where pK_0 is the intrinsic ionization constant, α is the degree of ionization, ΔFe is the extra work required to add or remove a proton due to neighboring charge groups, C_s is the ionic strength of the solution, R is the gas constant, and T is temperature.

The changes in the degree of ionization of weak polyelectrolytes in solution have been studied in detail by a number of research groups using different methods. Choi and Rubner recently have demonstrated that the degree of ionization of PAA and PAH can be readily estimated by Fourier Transform Infrared (FT-IR) spectroscopy[39]. They also have compared their results with those obtained by others. As shown in Figure 1.3, the pK_a (defined as the pH value at which 50% of functional groups are ionized) for PAA and PAH are 6.5 and 8.8, respectively, which is in good agreements with previous studies by others.

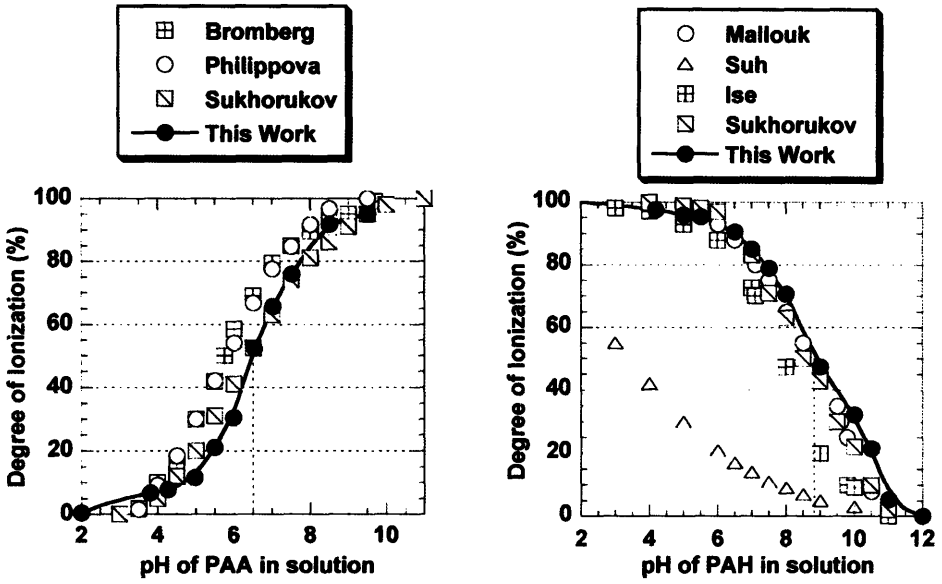

Figure 1.3. Estimated degree of ionization of PAA (left) and PAH (right) in solution as a function of pH. Data from other studies are also plotted for comparison. Adapted from the work of Choi and Rubner[39].

Changes in the degree of ionization of weak polyelectrolytes have a drastic effect on the solution properties of these weak polyelectrolytes. The conformation of weak polyelectrolytes is drastically changed due to the change in the linear charge density of the polymers. Their interaction with oppositely charged species (e.g., polyelectrolytes and nanoparticles) is also significantly altered as a function of solution pH.[38] More pertinent to this thesis, changes in the degree of ionization of weak polyelectrolytes have enormous effect on the structure and properties of polyelectrolyte multilayers as will be discussed below.

1.3.2.2 Weak Polyelectrolyte Multilayers

Recently, polyelectrolyte multilayers containing weak polyelectrolytes have received enormous attention because it is possible to precisely tune the film structure and properties by simply controlling the pH of polyelectrolyte solutions. Rubner et al. have shown that the chemical

composition and the growth behavior of multilayer thin films consisting of weak polyelectrolytes, PAA and PAH, can be varied by changing the pH of each polyelectrolyte solution[40,41]. Figure 1.4 shows that the average bilayer thickness (consisting of a pair of PAH and PAA layers) of multilayers comprising PAH and PAA can range from 6 to 140 Å depending on the pH of each polyelectrolyte solution. The molecular structures of these multilayers are also dramatically influenced by the assembly conditions as shown in Figure 1.5[42]. Depending on the degree of ionization of each weak polyelectrolyte, the conformation of adsorbed chains and the number of uncompensated functional groups (e.g., free carboxylic acid groups as shown in Figure 1.5 (B)) in the multilayer can be varied.

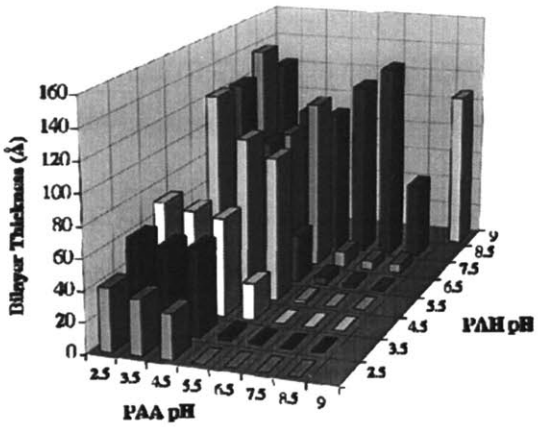

Figure 1.4. Complete pH matrix showing the average incremental thickness contributed by a PAH/PAA as a function of dipping solution pH. Adapted from the work of Shiratori and Rubner.[40]

Multilayer thin films containing partially ionized weak polyelectrolytes have been shown to exhibit interesting and potentially useful functionalities. Wang et al. have demonstrated that multilayer thin films containing partially ionized PAA (Figure 1.5 (B)) can be used as templates for in situ nanoparticle synthesis[43-45]. By utilizing so-called nanoreactor chemistry[43,46], the size and concentration of metal nanoparticles synthesized within multilayers could be controlled. Also the multilayers containing a large number of uncompensated functional groups have shown to exhibit excellent resistance toward cell-adhesion because these films tend to undergo a large degree of

swelling under physiological condition[47,48]. Rubner et al. also have shown that stimuli responsive thin films can be fabricated by assembling multilayers with partially ionized weak polyelectrolytes (i.e., PAA and PAH). Stimuli responsive weak polyelectrolyte multilayers that undergo reversible porosity transition or swelling transition as a function of solution pH have been investigated[49,50].

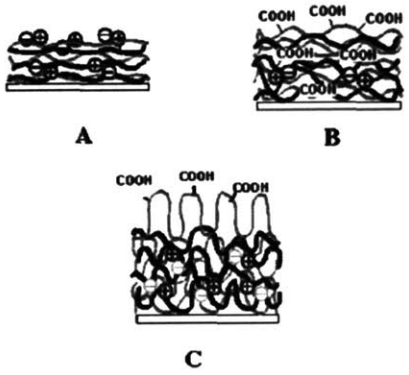

Figure 1.5. Schematic of molecular structure of PAH/PAA multilayers at different assembly conditions. (A) pH 6.5/6.5, (B) pH 2.5/2.5 and (C) pH 3.5/7.5. Adapted from the work of Choi and Rubner.[42]

1.3.3 Nanoparticle-Containing Multilayers

1.3.3.1 Polyelectrolyte/Nanoparticle Multilayers

Layer-by-Layer assembly also has been extensively utilized to create nanoparticle-containing multilayer thin films[51-53]. Analogous to the multilayers comprising oppositely charged polyelectrolytes, charged nanoparticles can be assembled into multilayers paired with an oppositely charged polyelectrolyte. Kotov et al. and Lvov et al. have shown that a variety of nanoparticles with unique optical, magnetic, catalytic and electronic properties can be readily assembled into thin films using LbL technique. Unlike the composite thin films comprising polymer and nanoparticles fabricated using conventional methods (e.g., spin coating), LbL coatings are highly homogeneous. Also by controlling the concentration of nanoparticle suspension, the size of nanoparticles, and the

ionic strength and pH of nanoparticle suspensions, the structure and properties of nanoparticle-containing multilayers could be precisely tuned[51-53]. The method also has been extended to create conformal nanoparticle-containing coatings on colloidal particles which are not readily achievable by other means[26,54,55].

A number of potentially useful multilayer thin films have been generated based on the LbL assembly of charged nanoparticles and polyelectrolytes. By taking advantage of the unique properties of nanoparticles, thin film devices for photovoltaic[56,57], biosensor[56,57], and photochromic applications[56,57] have been investigated. Most recently, surfaces exhibiting extreme wetting behaviors were prepared by creating nanoporous multilayers containing silica nanoparticles and titanium oxide nanoparticles[58,59].

1.3.3.2 All-Nanoparticle Multilayers

Despite the enormous attention the layer-by-layer deposition technique has received since the early 1990's when Decher and co-workers developed the technique[60], researchers have primarily focused on creating polymer-containing multilayer thin films. It is interesting note, however, that the very first study involving LbL assembly was reported in 1966[18]. Ralph K. Iler (Figure 1.6), who was a silica chemist at DuPont, reported that multilayers of oppositely charged colloidal particles can be readily assembled. In a typical example, he showed that negatively charged spherical silica nanoparticles and positively charged colloidal boehmite fibrils can be assembled onto glass substrates as shown in Figure 1.6[18]. Although this work did not receive immediate attention at the time, it was the one of the first studies that successfully demonstrated that thin films of nanoparticles can be readily assembled without any organic processing agents. In this study, he also showed qualitatively that various parameters including pH of particle suspension and the size of particles influence the growth behavior of the multilayers.

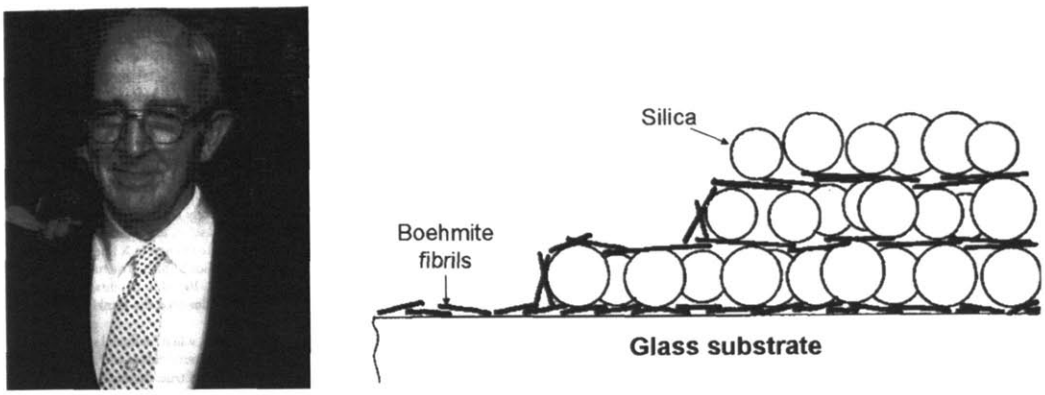

Figure 1.6. Photo image of Ralph K. Iler (left) and the first cartoon representation (right) of multilayers consisting of silica nanoparticles and colloidal boehmite fibrils deposited on a glass substrate. Adapted from the work of Iler[18].

1.4 Thesis Objectives and Oultline

The main objective of this thesis is to utilize the LbL technique to modify and engineer the surface properties of various substrates. pH-Sensitive materials including weak polyelectrolytes and nanoparticles are incorporated into multilayer thin films to create functional thin films on planar and non-planar geometries. It will be shown that by controlling the assembly conditions, mainly the pH of polyelectrolyte or nanoparticle solutions, different types of functional coatings can be generated and that this approach is an extremely versatile means to engineer surface properties of supports with different geometries. The thesis consists of three major parts divided by the geometry of the substrates that are under consideration.

In the first part (Chapters 2 and 3) of the thesis, multilayer thin film coatings based on hydrogen-bonding interaction is assembled onto spherical colloidal particles. Hydrogen-bonded multilayers, which can only be assembled at a low pH condition, were stabilized against dissolution using a solution-based crosslinking chemistry. Solution-crosslinked hydrogen-bonded multilayers exhibit interesting and potentially useful cell-adhesion resistance. Also these coatings can be utilized as

templates for in situ nanoparticle (e.g., silver and palladium) synthesis enabling the formation of nanoparticle-loaded hollow microcapsules. By creating silver-nanoparticle loaded multilayer coatings on magnetic particles, antibacterial microparticles that can be delivered to specific locations using a magnetic field are prepared.

In the second part (Chapters 4 and 5), the surface of track-etched polycarbonate membranes is functionalized using multilayer thin films that undergo pH-responsive swelling transition. The growth behavior of multilayer thin films in the cylindrical pores of track-etched polycarbonate membranes is studied using electron microscopy. Also the swelling behavior of the multilayers in such cylindrical confinement is investigated by monitoring the changes in the trans-membrane flux as a function of solution pH. A novel type of stimuli-responsive membrane that shows hysteretic gating behavior is generated, which potentially could be useful for the separation of pH-sensitive materials such as proteins and nanoparticles. In Chapter 5, it will be shown that the multilayer-coated track-etched polycarbonate membranes can be further modified to create heterostructured magnetic nanotubes that can be used in separation and drug delivery applications.

In the last part of this thesis (Chapters 6, 7, and 8), it will be demonstrated that multilayers consisting of oppositely charged nanoparticles can be assembled without the use of any organic processing agents such as polyelectrolytes. As a model system, positively charged TiO_2 and negatively charged SiO_2 nanoparticles are used to assemble all-nanoparticle multilayers on planar geometry. Historical and fundamental reasons that may explain the lack of research activities in making all-nanoparticle multilayers are also investigated by studying the effect of assembly conditions (i.e., pH of nanoparticle suspension) on the assembly behavior of TiO_2/SiO_2 nanoparticle multilayers. These all-nanoparticle thin films exhibit potentially useful antifogging, antireflection and self-cleaning properties.

Chapter 2
Hydrogen-bonded Multilayer Coatings on Colloidal Particles

2.1 Introduction

Single particle coatings based on layer-by-layer (LbL) assembled polyelectrolyte multilayers show great promise in engineering the surface properties of colloidal particles. Since the initial reports[26,27] that it is possible to deposit uniform coatings on colloidal particles with polyelectrolyte multilayers and subsequently remove the colloidal cores to produce hollow capsules, this new approach has witnessed rapid development. Most of this work to date, however, has been restricted to the use of fully or nearly fully charged polyelectrolytes due to the tendency of particles coated with partially charged polymers to flocculate during sample preparation as observed with slightly charged weak polyelectrolytes.[61,62] According to studies by Caruso et al. [61] and McClements[62], the adsorption of partially charged polyelectrolytes onto colloidal particles results in the decrease of electrostatic repulsion between the suspended particles, and eventually leads to irreversible aggregations. Caruso and coworkers recently attempted to overcome this problem by using copper-assisted LbL deposition of poly(acrylic acid) and poly(allylamine hydrochloride).[63] However, colloidal particle coatings based on weak polyelectrolyte multilayers that exhibit specific functional properties have not studied extensively. As described in Chapter 1, a number of polyelectrolyte multilayers containing partially ionized weak polyelectrolytes have been shown to exhibit properties not readily achievable with multilayers based on strong polyelectrolytes such as reversible porosity

transitions, discontinuous swelling transitions and nanoreactor capability suitable for the in-situ fabrication of nanoparticles.[44,45,47,49,50] In addition, it has been demonstrated that excellent long-term cell adhesion resistance is possible from weak polyelectrolyte multilayers assembled under such conditions.[47] The ability to create colloidal particle coatings with the functional attributes of certain weak polyelectrolyte multilayers is clearly a desirable goal for a number of applications.

Hydrogen-bonded multilayer systems containing pH-sensitive weak polyelectrolytes will be investigated in this chapter. The conditions needed to assemble weak polyelectrolytes via hydrogen bonding interactions are ideally suited for colloidal particle coating since the weak polyelectrolyte component must be maintained in a weakly ionized form during assembly to prevent dissolution of the multilayer.[64] Under these conditions, the particles may maintain a persistent positive or negative charge during the assembly process thereby preventing flocculation by electrostatic repulsion. In order to realize the full potential of H-bonded weak polyelectrolyte multilayers, however, it is necessary to introduce chemical crosslinks that prevent dissolution under pH conditions that ionize the functional groups of the weak polyelectrolyte. Such stabilization has previously been accomplished with thermal- or photo-crosslinking schemes,[65] although such dry-state approaches are not feasible in the colloidal coating process.

This chapter consists of three major parts. In the first part, it will be demonstrated that H-bonded multilayer coatings containing a weak polyelectrolyte (i.e., poly(acrylic acid)) and a neutral polymer (i.e., polyacrylamide) can be assembled colloidal particles and subsequently be stabilized by a simple solution-based crosslinking method. This method which uses carbodiimide compound has been previously used to crosslink electrostatically assembled multilayers by others.[63,66,67] This solution based crosslinking scheme enables the use of the hydrogen-bonded systems in various applications that involves pH greater than 4.0.

In the second part of the chapter, the interaction of mammalian cells (i.e., fibroblasts) with multilayer-modified colloidal particles will be studied. This particular hydrogen-bonded multilayer system has been shown to exhibit an excellent cell-adhesion resistance on planar surfaces[48]; thus, the same functionality would be expected for the multilayer coatings on microparticles. Unlike poly(ethylene glycol) based coatings[68] which have been extensively studied as the model bioinert coatings, the hydrogen-bonded multilayer studied in this Chapter offers greater stability against oxidative degradation[69] under physiological conditions. This multilayer system is a promising candidate for surface modification of medical implants and colloidal particles including drug particles and drug carriers.

As briefly described above, polyelectrolyte multilayers containing weak polyelectrolytes can be used as templated for in situ nanoparticles synthesis.[44,45] The methodology is an extension of previous work in which carboxylic acid functionalized block copolymers provided nanoreactor templates for inorganic cluster synthesis.[43,70,71] The LbL assembly conditions were tuned so that the multilayer thin films have a significant content of non-ionized carboxylic acid groups that have not been compensated by positive functional groups (e.g., charged amine groups). Protons of these carboxylic acid groups are then replaced by metal ions by a simple aqueous exchange procedure. Subsequently, the metal ions are converted into metal or semiconductor nanoparticles creating nanoparticle-loaded thin films. Nanoreactor chemistry is a versatile method in which a single template can be used to synthesize various inorganic nanoparticles and at the same time, control the size, concentration and spatial location.

The extension of nanoreactor chemistry to create uniform nanoparticle-loaded thin film coatings on colloidal particles, however, has been troublesome due to the difficulty faced in forming LbL assembled coatings with a high amount of uncompensated carboxylic acid groups as described above. In this respect, hydrogen-bonded multilayer systems containing pH-sensitive polyacids provide an

alternative opportunity for creating nanoparticle-loaded thin films on colloidal particles without the aggregation problems. As will be demonstrated in the third part of this chapter, the high content of free carboxylic acid groups in these systems make this hydrogen-bonded multilayer coatings ideally suited for nanoreactor chemistry. It will be shown that nanocomposite coatings consisting of polymer matrix and metal nanoparticles can be created on colloidal particles using the nanoreactor chemistry. I will also show that nanoparticle-loaded hollow microcapsules can be prepared by dissolving the core particles.

2.2 Experimental Methods

Materials. Poly(acrylic acid) (PAA) (M_W ~ 90 000, 25% aqueous solution) and polyacrylamide (PAAm) (M_W ~ 800 000, 10% aqueous solution) were purchased from Polysciences. 1.7 μm melamine formaldehyde (MF) particles (10 % aqueous solution) were purchased from Sigma-Aldrich, and two samples of amine functionalized polystyrene (Amine-PS) spherical particles (2.5 wt.% aqueous solution) were purchased from Polysciences; the particle diameters were specified as 3.18 and 5.8 μm by the supplier. 1-ethyl-3-(3-dimethylaminopropyl)carbodiimide hydrochloride (EDC) was purchased from Pierce Biotechnology. Silver acetate, tetraaminepalladium (II) chloride monohydrate ($[Pd(NH_3)_4]Cl_2 \cdot H_2O$), dimethylamine borane (DMAB), and sodium borohydride ($NaBH_4$) were purchased from Sigma-Aldrich. All chemicals were used as received.

Multilayer Coating of Colloidal Particles. All solutions were adjusted to low pH (pH < 3.5) to prevent dissolution of the film during assembly. With colloidal particles, the best results was obtained with assembly and rinsing solutions at pH lower than 3.5. At pH 3.0, which has been mainly used for film preparation previously[64,65], the 1.7 μm colloidal particles started to flocculate after a few layers were adsorbed. Therefore, the pH of each solution was adjusted to pH 3.5 using 0.01M HCl. It should be noted that the average bilayer thickness assembled (ca. 10 Å) at pH 3.5 measured on flat

substrates was only about 10 % of the film thickness that was obtained at pH 3.0. Larger microspheres (i.e., 5.8 μm) could be coated with pH 3.0 polymer solutions without any aggregation problems. Polymer solutions were prepared with a concentration of 0.04 M (based on repeat units) in deionized water. All polymer solutions were filtered using 0.45μm cellulose nitrate filters. To deposit hydrogen-bonded multilayers on colloidal particles, particles were suspended in a low pH polymer solution (pH < 3.5) with agitation for 10 ~ 15 minutes and then settled by using a centrifuge. After the polymer solution was removed by decantation, the colloids were rinsed with pH adjusted-water (the same pH as the polymer solution) three times with brief sonication (< 1 min). The colloidal particles were then re-suspended in the next polymer solution and the process was repeated to deposit multilayer coatings. In all cases, PAA was the first polymer adsorbed as particles were positively charged.

Crosslinking of PAA/PAAm coating. A 100 mg/mL EDC stock solution (at the same pH as the assembly condition) was made and 30 ~ 60 μL of the stock solution was added into a 1 mL dilute suspension of coated colloidal particles. The suspension was agitated overnight (~ 10 hr) and washed with deionized (DI) water (pH 5 ~ 6) several times. The quenching of EDC was achieved using 2-mercaptoethanol; however, this step was not absolutely necessary. For core template dissolution, the coated particles were resuspended in tetrahydrofuran (THF) or toluene for 30 min or less and then washed with respective solvent twice and with DI water 2 times.

Zeta-potential measurement. The zeta-potentials of the coated particles were measured with a ZetaPals (Brookhaven Instruments) and averaged over 10 runs. All the measurements were carried out in pH-adjusted deionized water.

FT-IR Spectroscopy. A Nicolet Fourier transform infrared (FT-IR) spectrophotometer equipped with Omnic software was used to obtain absorbance spectra (in transmission mode) after depositing

the polyelectrolyte multilayers onto ZnSe crystals. In order to enhance the intensity of the FT-IR spectra, the multilayer films were deposited at pH 3.0 and crosslinked in pH 3.0 adjusted EDC solution.

Fluorescence and Confocal Laser Fluorescence Microscopy. 1.7μm MF particles were coated with 10 bilayers of PAA and PAAm at pH 3.5. Carboxylic groups of PAA, which were activated with EDC, were subsequently reacted with 5-(aminoacetamido) fluorescein in dimethyl sulfoxide (DMSO) and phosphate buffered saline (PBS) 50/50 (v/v) solution. 10 μl of a 10 % colloidal solution was dropped on a glass slide to take Zeiss fluorescence microscopy images. Confocal laser microscopy experiments were conducted at the W. M. Keck Foundation Biological Imaging Facility at the Whitehead Institute.

Cell Cultures on Colloidal Surfaces. NR6WT mouse fibroblast cells were cultured on tissue culture polystyrene (TCPS) in α-minimal essential medium (α-MEM) supplemented with 7.5 % fetal bovine serum (FBS), 1 % (v/v) non-essential amino acids (10 mM), 1% (v/v) L-glutamine (200 mM), 1% (v/v) pyruvate sodium salt (100 mM), 1% (v/v) penicillin (10,000 U/ml, Sigma), 1% (v/v) streptomycin (10 mg/ml, Sigma) and 1% (v/v) Geneticin (G418) antibiotic (350 μg in 10 ml PBS) at 37 °C in a humidified atmosphere of 95% air and 5% CO_2. The pH of the medium was adjusted to 7.4. For attachment and proliferation assays on colloidal surfaces, fibroblasts were removed from their growth surface by trypsin. The cells were then seeded onto the sterilized colloidal particle-adsorbed TCPS dishes at a population density of ~10 000 cells/cm^2 for cell-adhesion investigations. Prior to cell adhesion studies, the colloids were sterilized by spraying with 70 % ethanol and dried under ambient condition in bio-safety hood. A Nikon inverted phase contrast microscope with Openlab 3.0 software was used for all experiments to capture images of the cell density, morphology, and spreading on the bare colloids and the multilayer-coated colloids for 5 days. Cell viability was tested with 0.4% trypan blue (Sigma) and counted with a hemocytometer.

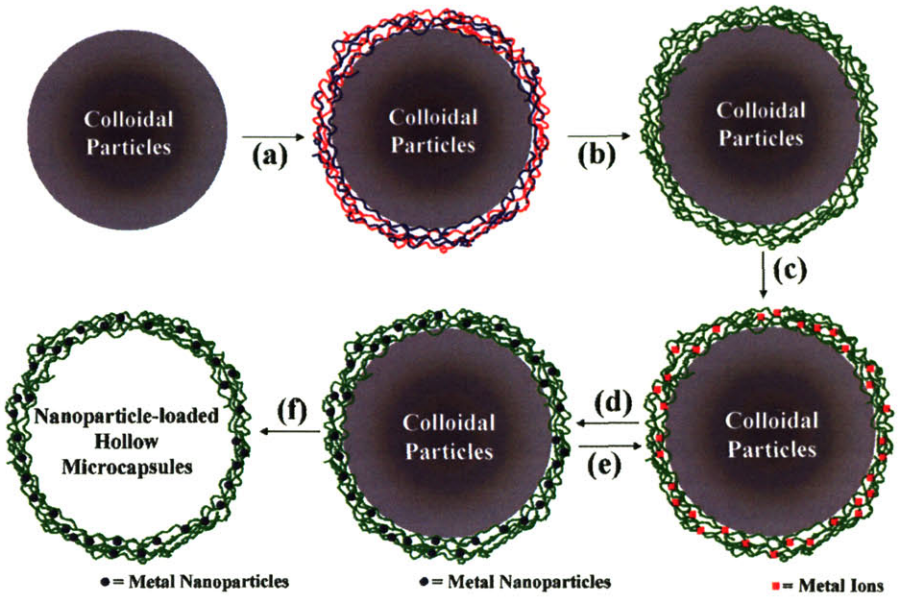

Figure 2.1. Formation of nanoparticle-loaded hollow microcapsules based on hydrogen-bonded multilayers. (a) Layer-by-layer assembly of (PAA/PAAm) multilayer thin film coatings, (b) crosslinking using water-soluble carbodiimide (i.e., EDC), (c) binding selective metal ions from aqueous solutions, (d) reduction of metal ions to zerovalent nanoparticles in $DMAB_{(aq)}$ or $NaBH_{4(aq)}$ and regeneration of carboxylic acid groups for further loadings[43,46], (e) reloading selective metal ions from aqueous metal ion solutions, and (f) dissolution of the amine-PS particles using an organic solvent (e.g., THF or toluene).

in situ Synthesis of Nanoparticles via Nanoreactor Chemistry. After the thin film coatings were crosslinked by EDC treatment, metal ions were bound to the carboxylic acid groups within the thin film coatings by suspending the coated amine-PS particles in metal ion containing aqueous solutions. Specifically, particles were suspended in 5 mM aqueous solutions of silver acetate or tetraaminepalladium(II) chloride for 30 min. After metal ion loading, the particles were washed thoroughly with DI water three times with brief sonication. Rinsed particles were then resuspended in 1 mM $DMAB_{(aq)}$ or 1 mM $NaBH_{4(aq)}$ for 5 min. The solution pH of 1 mM $DMAB_{(aq)}$ and 1 mM $NaBH_{4(aq)}$ was measured to be 7.5 and 9.5, respectively. The color of coated particles loaded with silver and palladium turned to reddish brown and dark black after 5 min, respectively. The coated

particles after reduction were rinsed with DI water three times. For multiple loadings [43,46], rinsed particles were subjected to the original sequence of treatments. Nanoparticle-loaded hollow microcapsules could be obtained by treating the particles with nanoparticle-loaded coatings with THF or toluene for at least 30 min. Figure 2.1 shows the steps involved in creating nanoparticle-loaded thin film coatings on colloidal particles and subsequently the microcapsules.

Transmission Electron Microscopy (TEM). TEM images were generated on a JEOL 200 CX operated at 200kV. The suspension of colloidal particles with metal nanoparticle-loaded thin film coatings was dehydrated and subsequently embedded in epoxy for microtoming. Ultrathin sections (70~100 nm) for TEM observation were microtomed at room temperature with a glass or diamond knife using a RMC MT-X ultramicrotome and collected on copper grids. To image microcapsules in plan view, THF treated particles were re-suspended in DI water and then deposited on carbon coated copper grids and allowed to dry in ambient conditions.

UV-Visible (UV-VIS) Spectroscopy. A Varian Cary 6000i UV-VIS-NIR spectrometer was used to measure the UV-VIS spectra of multilayer thin films deposited on quartz slides (both sides). To enhance the absorbance intensity, $(PAA/PAAm)_{10}$ multilayer thin films were assembled at pH 3.0 with a PAH layer as a primer layer to ensure the film assembly. After the films were assembled, the nanoparticles were created in the thin films following the same procedure as for the polyelectrolyte multilayer coated colloidal particles.

2.3 Results and Discussion

2.3.1 Solution-Crosslinking of Hydrogen-Bonded Multilayers

Crosslinking of PAA/PAAm multilayers to create stability in high pH solutions was achieved by aqueous carbodiimide chemistry. In typical carbodiimide chemistry, activated carboxylic acid groups

are reacted with a suitable amine or hydrazine reagent to create amide or imide bonds. When PAAm is used as the non-ionizable hydrogen bonding polymer, it has been found that a single immersion into the carbodiimide solution is sufficient to produce a multilayer film that is stable at physiological pH (7.4). In this case, crosslinks are formed between PAA and PAAm resulting in a cross-polymer network.

Methylene blue, a cationic dye that binds to free carboxylic acid groups, was used to confirm that the crosslinked multilayer films were stable at high pH condition. PAA/PAAm multilayer films as-assembled on glass or tissue culture grade polystyrene slides and after carbodiimide treatment were immersed in a pH 7.0 aqueous solution (for 10 minutes) and then immersed into a methylene blue solution also at pH 7. As expected, the as-assembled multilayer film dissolved quickly at pH 7.0, and therefore was not stained with methylene blue. In sharp contrast, the carbodiimide-treated multilayer film was uniformly stained with the dye indicating that the film had not dissolved during the pH 7.0 treatment. The crosslinked films are also stable at physiological conditions (buffered pH 7.4) for at least two weeks. This stability at physiological pH was also confirmed by fluorescent-dye labeling experiments carried out on coated colloidal particles.

FT-IR measurements of carbodiimide (EDC) treated films confirm the crosslinking of the PAA/PAAm multilayer. As shown in the spectrum B of Figure 2.2, new peaks appeared around 1710 cm^{-1} (two peaks overlapping with the free acid peak) and 1180 cm^{-1}, which correspond to the formation of imide bonds between PAA and PAAm. These peaks become more intense when a higher concentration of carbodiimide (spectrum d in Figure 2.2) was used. The peaks appearing at 1805, 1780 and 1042 cm^{-1} at the early stage (30 min) of the reaction (spectrum c in Figure 2.2), correspond to anhydride peaks. As the reaction continued, the anhydride peaks diminished and completely disappeared after overnight treatment in the EDC solution. The peaks associated with the

imide bonds also remain intact after exposure to high pH conditions. Similar spectral changes with thermally crosslinked films of PAA/PAAm have been observed previsouly.[65] However, the thermal crosslinking method has a limitation on the choice of substrate (highly depends on its glass transition or deformation temperature). This new carbodiimide chemistry, on the other hand, takes place at room temperature and the degree of crosslinking is readily controlled by the amount of carbodiimide added (Figure 2.2). The low level of inter-chain crosslinking achieved with the low concentration of EDC (not easily detectable by FT-IR) is still sufficient to render the multilayer film stable when the acid groups become ionized at physiological pH condition. In fact, this multilayer system exhibits excellent resistance to the attachment of many types of cells (e.g, fibroblasts, hepatocytes and epithelial cells) as well as certain proteins.[47,48] The high level of "bioinertness" exhibited by this multilayer is due in part to its ability to swell substantially at physiological pH[47,48]; a property that would be diminished with excessive crosslinking. If desired, however, additional crosslinking can be promoted with the use of a higher concentration of EDC or an extra crosslinker such as a dihydrazine or diamine.

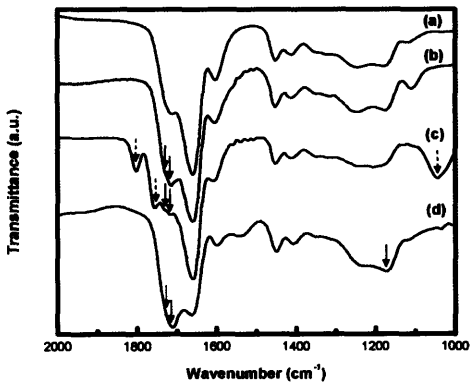

Figure 2.2. FT-IR spectra of PAA/PAAm 10 bilayer films; (a) as assembled, (b) EDC-crosslinked ([EDC] = 0.005 M) (c) EDC-crosslinked (early stage of (b)) and (d) EDC-crosslinked multilayer

([EDC] = 0.05 M) (solid line arrows indicate imide peaks and dotted line arrows indicate anhydride peaks).

Figure 2.3 shows fluorescence and confocal microscope images of colloidal particles coated with fluorescent dye-labeled PAA/PAAm multilayers (EDC coupling with 5-(aminoacetamido) fluorescein). The micron-sized particles were coated with 10 bilayers of PAA/PAAm that were crosslinked by the carbodiimide chemistry.

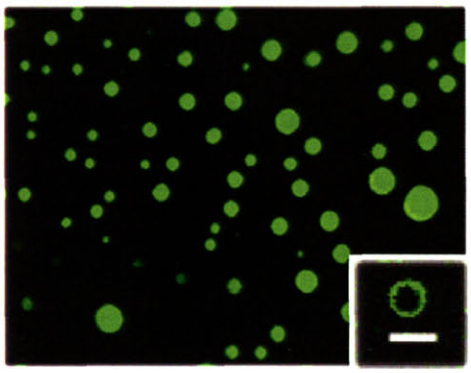

Figure 2.3. Fluorescence and confocal laser (inset) microscope images of fluorescent dye-labeled PAA/PAAm multilayer-coated microspheres dispersed in aqueous solution. (10 bilayers, scale bar = 2 μm)

This labeling reaction was performed at pH 7 and the labeled particles were exhaustively rinsed and dialyzed against neutral water for several days. As shown in Figure 2.3, the microspheres are uniformly coated with the H-bonded multilayers. In addition, the multilayer-coated microspheres did not coagulate but mostly existed as well separated single particles. In this case, the surfaces of the particles are coated with multilayers that are H-bonded and contain a small fraction of ionized acid groups during the entire assembly process. This persistent net negative charge helps to prevent the particles from flocculating.

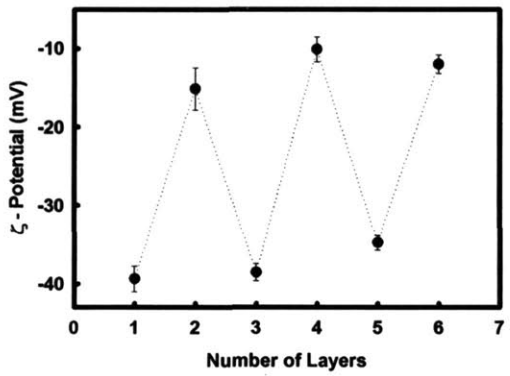

Figure 2.4. ζ-potential variation of PAA/PAAm-coated MF particles (1.7 μm diameter) as a function of layer number at pH 3.5. (Error bars represent standard deviations)

The fact that the particles maintain negative charge during the assembly process was confirmed by zeta-potential measurements. Zeta (ζ) potentials of coated particles were measured to monitor the layer-by-layer deposition of PAA and PAAm on 1.7μm MF particles at pH 3.5. The ζ –potential of the particles as a function of layer number is shown in Figure 2.4. The ζ-potential of the bare particles was +67 mV. As the polymers were adsorbed onto the particles, the ζ-potentials of the particles alternated between two negative values of approximately -37 mV and -11 mV. The former value corresponds to the case in which the outermost layer is PAA and the latter value corresponds to that of the PAAm. In contrast to alternating reversals in the sign of ζ –potentials found in most studies where polycation and polyanion pairs were used, the values stayed in the negative range throughout the layer-by-layer process. This result indicates that when the PAAm layer is adsorbed onto a preceding PAA layer, the negative surface charge is partially screened by the neutral polymer. On the other hand, when PAA adsorbs on top of the PAAm layer, the ionized carboxylic acid groups of PAA contribute to the highly negative surface charge. The colloidal particles did not undergo any irreversible flocculation after the deposition of layers of either PAA or PAAm. It is noteworthy that PAAm alone has been reported to sterically stabilize colloidal particles.[72] In addition, the high

degree of hydration of the multilayers may play an important role in preventing irreversible aggregation and enable the LbL coating process to be performed successfully.

2.3.2 Bioinert properties of solution crosslinked hydrogen-bonded multilayer coatings on colloidal particles

As mentioned earlier, this particular multilayer system has been shown to exhibit excellent resistance to cell adhesion. In many of the biomedical applications envisioned for multilayer-coated particles, the property of "bioinertness" is essential. To demonstrate that particles coated with PAA/PAAm multilayers exhibit this important property, particles with and without the crosslinked multilayer coating were deposited onto tissue culture grade polystyrene (TCPS) dishes and their interaction with mammalian cells were observed. Specifically, wild-type NR6 fibroblasts in serum containing media were seeded onto the dish. Prior to the cell study, the multilayer-coated colloids were dialyzed against deionized water to remove any residual chemicals from the crosslinking procedure. Figure 2.5 shows the fibroblast response to loose-packed and close-packed particles after the cells were seeded. In the case of the bare particles, the fibroblast cells readily attach to surface regions containing the particles and appear to cluster and engulf them (Figure 2.5-1a and 1b). In contrast, the cells clearly avoid the surface regions containing the multilayer-coated particles (Figure 2.5-2a and 2b) and instead prefer to attach to regions devoid of particles. This behavior continued until at least day 3 of cell seeding (more than 80% cell confluence). With surfaces containing highly close-packed particles, cells again readily attached to the surface coated with bare particles (Figure 2.5-1c), but resisted attachment to the surfaces coated with multilayer-coated particles (Figure 2.5-2c). Cell viability testing confirmed that the multilayer-coating was not cytotoxic.

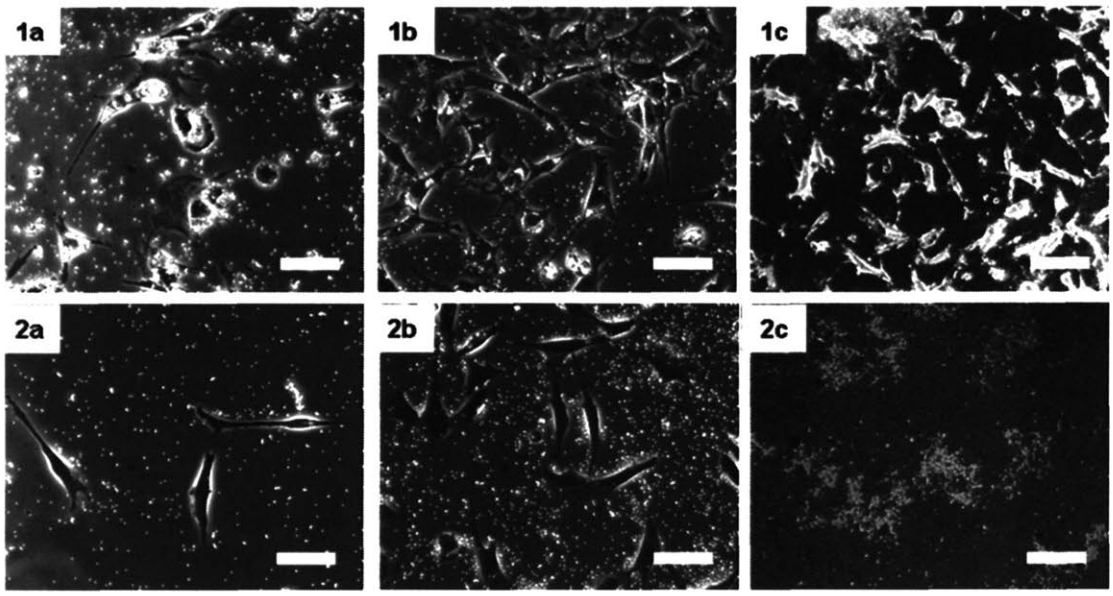

Figure 2.5. Phase contrast optical microscope images of fibroblasts on bare colloids (1a-c) and multilayer-coated colloids (2a-c); cells with loose-packed bare colloids on day 1 (1a) and on day 2 (1b), cells with close-packed bare colloids on day 2 (1c), cells with loose-packed multilayer-coated colloids on day 1 (2a) and on day 2 (2b), and cells with close-packed multilayer-coated colloids on day 2 (2c) (cells were seeded with a density of 10,000 cells/cm^2 in both surfaces, scale bar = 100 μm).

2.3.3 Formation of nanoparticle-loaded hollow microcapsules

The feasibility of using the solution-crosslinked hydrogen-bonded (PAA/PAAm) multilayer thin films as templates for nanoreactor chemistry was first examined and confirmed by UV-VIS spectroscopy of the crosslinked multilayer thin films on quartz slides. As shown in Figure 2.6, when the EDC-crosslinked $(PAA/PAAm)_{10}$ multilayer thin films are loaded with metal ions, the UV-VIS spectra for Ag^+ loaded thin films do not show any significant peaks, whereas the $[Pd(NH_3)_4]^{2+}$ loaded films show a broad peak around 320 nm corresponding to palladium ions in the polymer thin film. Upon reduction, the UV-VIS spectra of the silver-loaded films show the appearance of a surface plasmon resonance (SPR) peak at 450 nm.[73] A slight red shift in the SPR peak compared to the value reported (~ 435 nm) in a previous paper[44] suggests that the solution-reduced Ag

nanoparticles grow to larger sizes in the hydrogen-bonded multilayers compared to the hydrogen-reduced Ag nanoparticles in multilayers composed of PAA and PAH, or that small nanoparticles agglomerate into larger clusters in the hydrogen-bonded templates.[74] Formation of somewhat larger Ag nanoparticles is also corroborated by TEM observation as described below. As for palladium nanoparticles, it is known that the UV-VIS spectrum is influenced only by Mie scattering without any SPR peak. The Mie scattering leads to an increase in the absorbance throughout the entire UV-VIS region.[75,76]

To confirm the multiple loading capability of the hydrogen-bonded multilayer thin films, Ag and Pd nanoparticles were loaded and reduced up to three times. As can be seen in Figure 2.6 (a), the intensity of the SPR band of the nanoparticle-loaded films increased with the number of loading and reduction cycles of Ag similar to a previous report by Wang et al. [44] The SPR band of the Ag nanoparticles also shifts to higher wavelength reflecting the fact that the size as well as the interparticle interaction of the nanoparticles increased as the number of loading and reduction cycles was increased.[74] Figure 2.6 (b) shows that, in the case of Pd nanoparticles, the absorbance intensity of a broad band across the entire UV-VIS region increases, reflecting the increase in the amount of Pd nanoparticles within the film. The UV-VIS spectra of Ag and Pd nanoparticle-loaded films do not show significant change after one month in ambient air, which suggests that in situ synthesized Ag and Pd nanoparticles were stable against oxidation within the films.

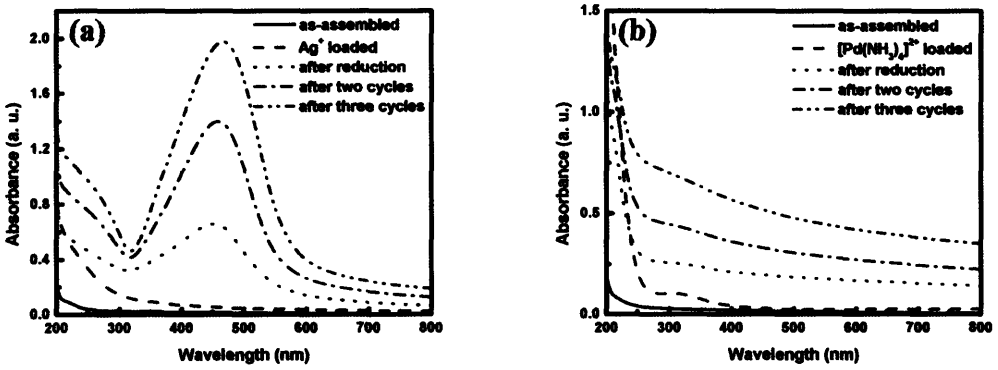

Figure 2.6. UV-VIS spectra of $(PAA/PAAm)_{10}$ multilayer thin films assembled on quartz slides. (a) Ag and (b) Pd loaded and reduced films.

Depending on the size of amine-PS particles, irreversible aggregation of the multilayer coated particles during LbL assembly could be eliminated by tuning the solution pH of each polymer solution. For 5.8 μm amine-PS particles, the films were assembled with up to twelve layers (six bilayers) without any aggregation problems at pH 3.0. When the 3.18 μm amine-PS particles were coated at pH 3.0, however, the particles showed some degree of aggregation after the eighth layer. In order to avoid the aggregation of the 3.18 μm amine-PS particles during the LbL process, the pH of each polymer solution as well as the rinse solution was raised to pH 3.2. At this pH, aggregation was not observed up to six bilayers. A slight increase in the assembly pH imparts an additional small amount of negative charge on the surface of coated colloids, which is sufficient to maintain the colloidal stability against irreversible aggregation as was discussed in Section 2.3.1. However, a decrease of ca. 25 % in the film thickness is expected based on quartz crystal microbalance (QCM) experiments (not shown) conducted at the two different pH conditions. If the size of the colloidal particles is further reduced below 1 μm, the colloidal suspension becomes more susceptible to irreversible aggregation during the LbL assembly. As shown in Figure 2.7 (a), as-assembled $(PAA/PAAm)_6$ multilayer coatings on particles were intact even after the amine-PS particles were

dissolved away by THF treatments, and microcapsules that retain the approximate size of the original amine-PS particles were obtained.

As was reported previously, the crosslinking of PAA/PAAm multilayer thin films with a low concentration of EDC at low pH renders the multilayer thin films stable even at high pH conditions above pH 7 as discussed in Section 2.3.1. Figure 2.7 (b) demonstrates that microcapsules were stable against dissolution after crosslinking the coatings with EDC and treating them with pH 7 adjusted DI water. Non-crosslinked hydrogen-bonded multilayer coatings dissolved away in pH 7 adjusted DI water and I could not observe any capsules after the amine-PS particles were dissolved away in THF or toluene. The surface topologies of microcapsules before and after crosslinking are strikingly different. As can be clearly seen in Figure 2.7, the as-assembled capsules have a few folds and creases after they were dried on TEM grids, whereas the EDC-crosslinked microcapsules have many folds and creases after drying. I believe that the crosslinking of the (PAA/PAAm) multilayer coatings prevents the chains from rearranging while the capsules are being dried and, in turn, decreases the ability of the capsule wall to respond to abrupt changes in the environment such as would occur during dehydration. Additionally, Pavoor et al. and Nolte et al. have recently reported that the wet-state modulus and hardness of thermally-crosslinked polyelectrolyte multilayer thin films composed of PAA and PAH are significantly higher than observed for wet, un-crosslinked (PAA/PAH) multilayer thin films.[77,78] The crosslinking of hydrogen-bonded (PAA/PAAm) multilayers is expected to have a similar effect on the mechanical properties of these capsule walls leading to significantly different capsule morphologies as they are dried from aqueous suspension. On the other hand, as-assembled hydrogen-bonded multilayer hollow capsules without crosslinking may find use in applications where the coatings are intact at low pH conditions and then dissolve away exposing the core at high pH conditions.

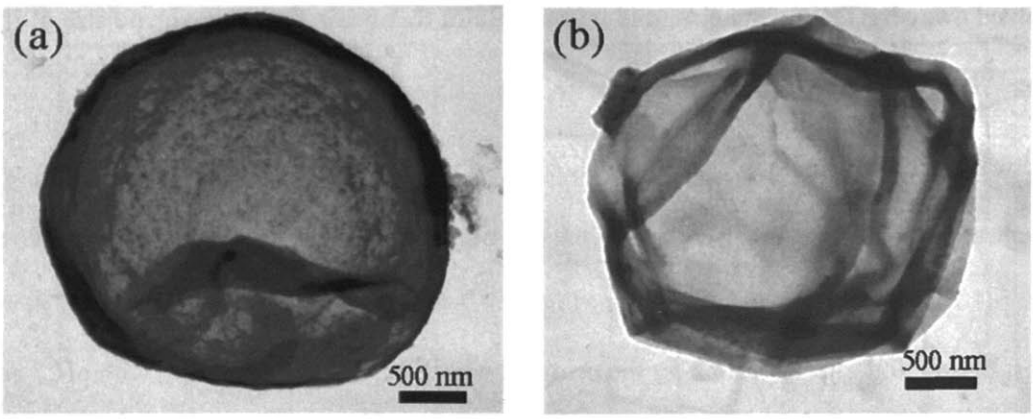

Figure 2.7. TEM Images of (PAA/PAAm) microcapsules (5 bilayers) assembled at pH 3.0 (a) without crosslinking and (b) with crosslinking. The diameter of the extracted amine-PS particles was 3.18 μm. (Each figure represents majority of microcapsule morphologies observed under TEM.)

The presence of Ag nanoparticles within the EDC crosslinked (PAA/PAAm) multilayer thin film coatings was confirmed by TEM. Figure 2.8 shows the cross-section TEM images of the nanoparticle-loaded thin film coatings on 3.18 μ amine-PS particles. The nanoparticle-loaded coating conformably coats the entire surface of the amine-PS particles. Also the magnified images clearly show that the particles are highly dispersed within the multilayer coating. As the number of loading cycles was increased, the density as well as the size of the Ag nanoparticles increased. The size of the particles is greater than that observed in a previous study where the loaded metal ions in electrostatically assembled weak polyelectrolyte multilayer thin films of PAA and PAH on planar substrates were reduced in $H_{2(g)}$.[44] It is suspected that the aqueous phase reaction imparts more mobility to the metal ions during reduction. In addition, the crosslinked (PAA/PAAm) multilayers are known to swell in a high pH aqueous environment. The solution pH of both of the reducing agents was above 7.0. The swelling of the coatings can provide more mobility within the polymer matrix thereby allowing larger particles to form compared to the denser polymer matrix present in the gas phase reduction.

Cross-section TEM images in Figure 2.8 provide additional information about the nanoparticle-loaded coatings on the microparticles. First of all, the thickness of the thin film coatings on the particles can be estimated by measuring the thickness of the nanoparticle-loaded coatings. The thickness measured from the TEM images for a 6 bilayer coating of PAA/PAAm assembled at pH 3.0 after one loading and reduction cycle is approximately ~ 28 nm (Figure 2.8 (a)), which is a bit larger than the thickness of the same multilayer thin film assembled on a planar substrate without any metal nanoparticle incorporation (~ 26 nm). The thickness of multilayer thin films increases as the number of loading and reduction cycles in a multilayer coating is increased, which was also observed by Wang et al.[44] In addition, it has been previously reported that ultramicrotomy can increase a film thickness by 10 % compared to that measured using an ellipsometer.[10,44] The slight increase in the thickness of multilayers on spherical particles compared to that of multilayers on planar substrates is in contrast to a previous report by Kozlovskaya et al. They reported that the thickness, determined by electron energy loss spectrometry (EELS), of hydrogen-bonded multilayers (composed of poly(ethylene oxide)/poly(methacrylic acid) and poly(ethylene oxide)/poly(N-vinylpyrrolidone)) assembled on cadmium carbonate ($CdCO_3$) spherical particles was substantially less than that of the same multilayers assembled on planar Si substrates. It should also be noted that the nanocomposite coated particles appear to have experienced some longitudinal deformation during the sectioning process. The long axis of the resultant deformed ellipsoid is perpendicular to knife marks visible on the thin sections, which corroborates the fact that ultramicrotomy caused deformation of the embedded particles. Similar deformation due to ultramicrotoming has been observed for PAH/SPS multilayer coated colloidal particles.[27] Also it is possible that the ultramicrotomy of metal-ion stained multilayer coatings on spherical particles will provide a means to measure the thickness of these coatings.

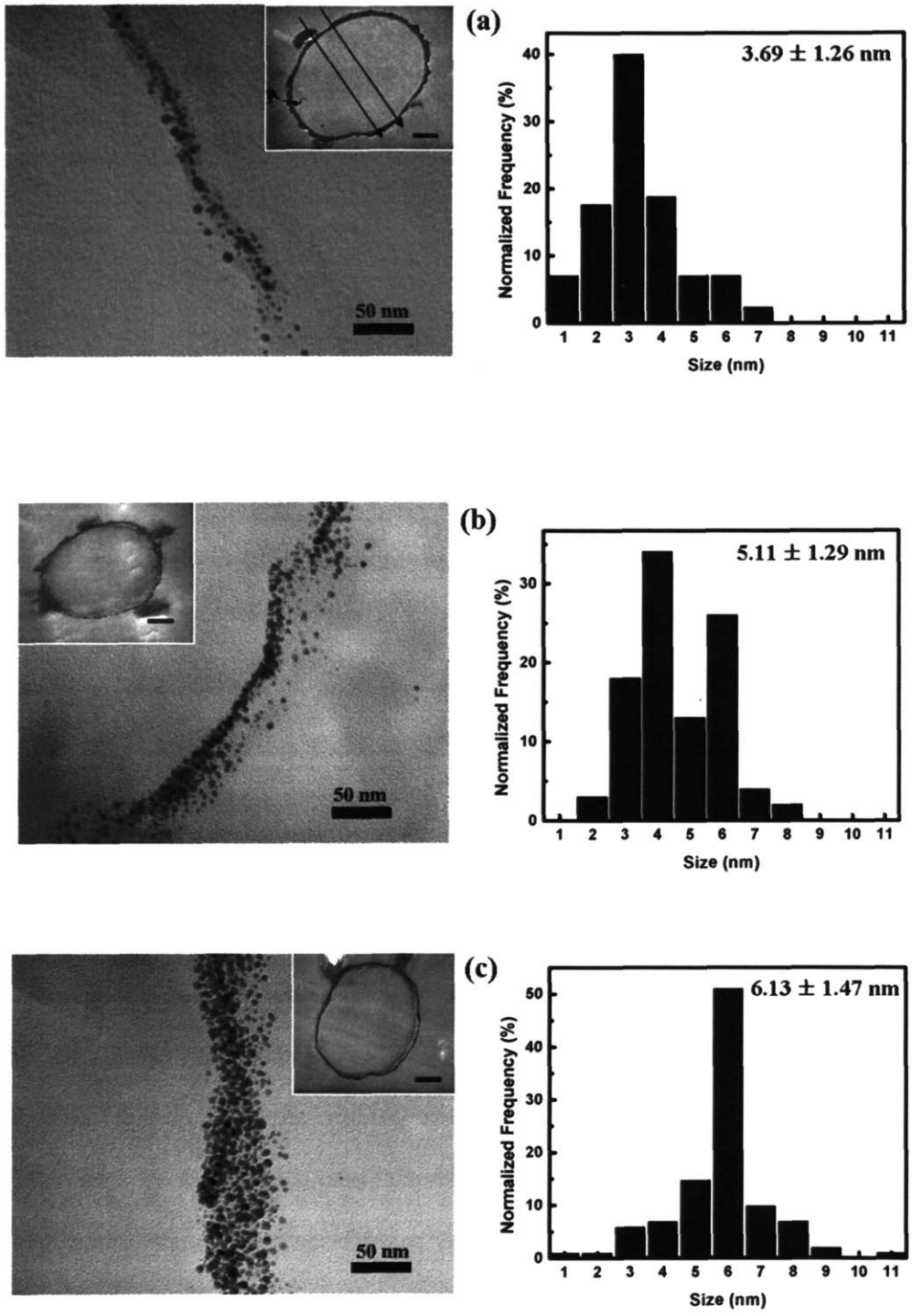

Figure 2.8. Cross-section TEM Images of $(PAA/PAAm)_6$ Ag nanoparticle-loaded coatings assembled at pH 3.0 on 3.18 μm amine-PS particles (a) after first loading and reduction cycle (arrows show the

direction of knife marks), (b) after the second cycle and (c) after the third cycle. Inset scale bars are 500 nm. Histograms show the size distribution of Ag nanoparticle measured from each TEM image. Average particle size is denoted in each histogram along with standard deviation (approximately 100 nanoparticles were measured to produce the histograms; while showing the size distribution of Ag nanoparticles, these histograms are not necessarily the true statistical representation of the entire Ag nanoparticle size distribution.).

Hollow microcapsules with nanoparticles dispersed within the capsule walls could be obtained by treating the nanocomposite coated particles with THF or toluene for at least 30 min. Figure 2.9 (a) and (b) show that nanoparticles of Ag and Pd are well dispersed within the capsule wall; however, some loss in the amount of Ag nanoparticles was observed within the crosslinked (PAA/PAAm) multilayer thin films if THF treatment was prolonged beyond 24 hr. UV-VIS spectra of the Ag nanoparticle-loaded thin films on glass slides that were immersed in THF for 24 hr showed a decrease (more than 10 %) in the intensity of the silver SPR peak around 450 nm (not shown). After a week in THF, the Ag nanoparticle density (based on UV-VIS measurement) was roughly half of its original value. When Pd nanoparticle-loaded coatings are exposed to THF for more than 1 hr, the density of Pd nanoparticles in the capsules was substantially less (ca. 30%) than that found in 30 min-treated capsules based on TEM observation. A similar trend was seen when toluene, which is less polar than THF, was used for core template extraction. The fact that use of these two different organic solvents gives similar results indicates that the nanoparticles are diffusing out of the multilayer rather than being dissolved by organic solvents during the organic solvent treatment. Therefore, in order to retain the nanoparticles within the nanocomposite coatings, it is essential to minimize the time required to extract the amine-PS particles out of the multilayer coating.

The size and the density of nanoparticles within the capsule walls differ for different systems. Figure 2.9 (a) shows that when loading and reduction cycles were repeated twice for Ag loaded hollow capsules, the size of particles is approximately 5 ~ 6 nm, which is close to the size of

nanoparticles seen in the cross-section images in Figure 2.8 (b). The size of Pd nanoparticles is approximately 1 ~ 2 nm, which is smaller than that of the Ag nanoparticles after one loading and reduction cycle (Figure 2.8 (a)). The amount of divalent cations that can be exchanged with the protons of the carboxylic acid groups is half the amount of monovalent ions. Also the mobility of divalent metal ions in a carboxylic acid rich polymer thin film matrix is expected to be considerably lower than that of monovalent ions which, in turn, prevents the growth of larger particles. Clay et al. have reported that the diffusion of divalent metal cations is much slower than that of monovalent cations within carboxylic acid group rich domains of microphase separated block copolymers.[46] Kane et al. also have presented models that predict the size of in situ synthesized nanoparticles to be dependent on the diffusion of metal ions within polymer matrix.[79]

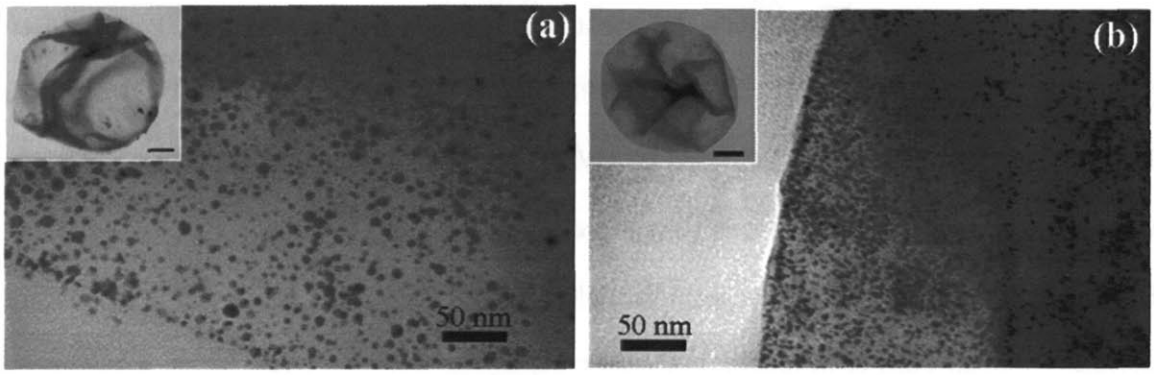

Figure 2.9. TEM Images of EDC-crosslinked (PAA/PAAm)5 multilayer hollow capsules assembled at pH 3.0 and loaded with (a) two loading and reduction cycles of Ag nanoparticles (the diameter of extracted amine-PS particles was 5.8 μm; inset scale bar = 1.2 μ), and (b) one loading and reduction cycle of Pd nanoparticles (the diameter of extracted amine-PS particles was 3.18 μm; inset scale bar = 700 nm).

2.4 Conclusions

Hydrogen-bonded multilayers containing PAA and PAAm were assembled successfully onto colloidal particles and subsequently crosslinked with a single step carbodiimide reaction. The

resultant multilayer coatings are stable to physiological pH and cell culture media and exhibit the ability to resist cell attachment. A general methodology for creating nanoparticle-loaded thin film coatings on micron-sized colloidal particles based on the layer-by-layer assembly of hydrogen-bonded multilayer thin films and subsequent nanoreactor chemistry was also demonstrated. This technique enabled control over the size as well as the amount of loaded metal nanoparticles within the thin film coating. Crosslinked hydrogen-bonded multilayer thin film coatings are robust enough to withstand the high pH environment during the reduction step. Subsequent core particle extraction can be used to obtain hollow capsules with a high dispersion of nanoparticles within the capsule walls. In the next chapter, the antimicrobial properties of Ag nanoparticle-loaded coatings will be investigated.

Chapter 3

Antibacterial Properties of Ag Nanoparticle-loaded Multilayers and Formation of Magnetically Directed Antibacterial Microparticles

3.1 Introduction

The adhesion of bacteria onto the surfaces of various materials such as medical implants (e.g., urinary catheters) and industrial pipelines can lead to the formation of biofilms and the outbreak of infectious diseases[80]. Antibacterial coatings that can be easily applied to different types of surfaces to prevent harmful microorganisms from proliferating would minimize such undesirable situations. Antibacterial coatings on colloidal particles could be even more beneficial in various applications due to their high surface-to-volume ratios[81-84]. Such antibacterial colloidal particles, for example, could be incorporated into materials that are processed from suspension or emulsion such as powder coating materials and pigments, and they could also be used as fillers in various medical devices.[84] Furthermore, by using particles that respond to external fields such as magnetic fields, it would be possible to deliver antibacterial agents to specific locations where bacteria tend to adhere and form biofilms without contaminating the bulk fluid of industrial and food processing pipelines with high concentrations of the antibacterial agent.[85]

Silver has been known to have extraordinary inhibitory and bactericidal properties since ancient times.[86,87] While being relatively non-toxic to human cells, silver possesses antibacterial properties for a broad spectrum of bacterial strains that are found in industrial processes as well as in the human body.[88] Because of these characteristics, silver in various forms is ideally suited for a

wide range of applications in consumer, industrial and medical products. Various devices and products such as urinary catheters, suture rings, and food packaging elements have silver as an antiseptic component. It is believed that silver ions interact with sulfhydryl groups, or thiol groups (-SH) on the membranes of bacteria causing disruption of their permeability thereby leading to microbial cell death.[88] Because of the mechanism by which silver acts as a biocidal agent, the likelihood of bacteria becoming resistant to silver-based antibiotics is believed to be low.[88] While numerous reports have suggested that silver-based coatings can be useful in this regard, a disadvantage of these systems is that conformal coatings on different substrates with precise control over the thickness, content of silver and sustained release of silver is often difficult.[89,90] Also many of these antibacterial coatings are rigid inorganic films preventing their use on flexible materials.[89,91,92] In addition, creating antibacterial coatings on colloidal particles such as pigments or magnetic microparticles with precise control over the surface properties cannot be easily achieved with conventional techniques.

In Chapter 2, it was demonstrated that by using the hydrogen-bonded multilayer consisting of poly(acrylic acid) (PAA) and polyacrylamide, and the nanoreactor chemistry, silver nanoparticle loaded multilayer coatings can be created on colloidal particles. [93] This methodology provides a means to control the weight (or volume) fraction and size of nanoparticles in the thin film coatings.[44,93] Such versatility will be essential in designing antibacterial coatings on various substrates. The first report of silver nanoparticle-containing polyelectrolyte multilayers that exhibit antibacterial properties was published by Dai and Bruening.[94] Grunlan et al. have also studied the antimicrobial activity of silver ion and/or cetrimide-loaded polyelectrolyte multilayers.[95]

In this chapter, it will be demonstrated that Ag nanoparticle-loaded hydrogen-bonded multilayers assembled on planar and curved supports such as magnetic microspheres show excellent antibacterial properties. The widely used Kirby-Bauer method[96] was utilized to test the antibacterial properties

of the nanocomposite thin films on planar substrates. The antibacterial properties of the nanocomposite multilayer on planar supports were studied as a function of the thickness of multilayers and the number of silver loading and reduction cycles against the Gram-positive strain, *Staphylococcus Epidermidis* (*S. Epidermidis*) and the Gram-negative strain, *Escherichia Coli* (*E. Coli*). The zone of inhibition (ZoI) determined by the disc-diffusion test increases as the thickness of the multilayer film is increased. Results obtained for the values of the ZoI as a function of film thickness can be described adequately with a simple diffusion model. The effect of multiple silver loading and reduction cycles is not as pronounced as that of the thickness of the multilayers. It will be shown, however, that conversion of Ag ions to zerovalent Ag nanoparticles is needed to achieve sustained release of antibacterial silver from these multilayer thin films; unlike the zone of inhibition, the duration of the sustained release depends on the total supply of silver in the film, and therefore is strongly affected by the number of silver loading and reduction cycles employed in the film preparation.

Magnetic microparticles have been studied extensively over the last two decades as delivery vehicles for localizing therapeutic agents to a specified target site by magnetic means.[85,97-99] It is demonstrated that magnetic microspheres coated with antibacterial multilayers can be delivered to a specific region to localize a high concentration of antibacterial silver while maintaining a low concentration of silver in the bulk solution. The minimum concentration of the nanocomposite-coated magnetic microparticles that is required to completely inhibit the growth of bacteria was also determined by the agar dilution technique.[96] The minimum inhibitory concentration (μg of nanocomposite coated magnetic microparticles per g of entire suspension, or ppm) of magnetic microparticles measured by this test decreases as the total supply (weight or volume fraction) of Ag nanoparticles within the multilayer coatings increases.

3.2 Experimental Section

Materials. Poly(acrylic acid) (PAA) (M_w ~ 90 000, 25% aqueous solution) and polyacrylamide (PAAm) (M_w ~ 800 000, 10% aqueous solution) were purchased from Polysciences. Carboxylic acid functionalized magnetic microspheres (COMPEL™, 5 wt% aqueous solution) were purchased from Polysciences; the particle diameter measured by a scanning electron microscope (SEM) was ~ 2.5 μm. Poly(allylamine hydrochloride) (PAH) (M_w ~ 70 000), sulfonated polystyrene (SPS) (M_w ~ 70 000), silver acetate (Ag(Ac)), and borane dimethylamine complex (DMAB) were purchased from Sigma-Aldrich. Non-pathogenic *Staphylococcus Epidermidis* (*S. Epidermidis*) and *Escherichia coli* (*E. Coli*) were purchased from ATCC. The bacterial strains were kept at -80 °C in a freezer before use. 1-Ethyl-3-(3-dimethylaminopropyl)carbodiimide hydrochloride (EDC) and Live/Dead® BacLightTM Bacterial viability kits were purchased from Molecular Probes. Luria-Bertani (LB) broth and LB agar medium were purchased from EMD chemicals. 15-cm Mueller-Hinton (MH) agar plates were purchased from Hardy Diagnostics and were used within two weeks after arrival. All chemicals were used as received.

Formation of Ag nanoparticle-loaded Multilayer Coatings on Planar Substrates and on Magnetic Microspheres. Details about the deposition and crosslinking of PAA/PAAm multilayer thin film coatings as well as the in situ Ag nanoparticle synthesis within the multilayers on colloidal particles have been published previously.[93,100] In brief, all solutions (20 mM based on the repeat unit) were adjusted to pH 3.0 with HCl. Magnetic microspheres were suspended in a PAH solution with agitation for 20 minutes and then settled by using a centrifuge. It is also possible to rapidly separate (< 1 min) coated magnetic particles by using a magnetic field. After the polymer solution was removed by decantation, the magnetic beads were rinsed with pH 3.0 adjusted deionized (DI) water two times with brief sonication (< 1 min). The microspheres were then re-suspended in a pH

3.0 PAA solution for 10 min followed by two rinse steps and then re-suspended in a pH 3.0 PAAm solution also followed by two rinse steps. The process was repeated to deposit multilayer coatings. All future references to the multilayer thin films in this report will be denoted as "PAH(PAA/PAAm)$_x$ Ag$_n$" where the x and n are the number of deposited bilayers and the number of Ag loading and reduction cycles, respectively. n = + denotes Ag ions loaded but not subjected to the reduction step. For crosslinking of the coatings, 40 μL of a 100 mg/mL EDC stock solution (at pH 3.0) was added to a 1 mL dilute suspension of coated magnetic beads. The suspension was agitated overnight (~ 10 hr) and washed with DI water (pH 5 ~ 6) several times. The same protocol was used to create multilayer thin films on 22-mm planar round coverglass slides (VWR International) or Thermanox® coverslips (Electron Microscopy Sciences) by using an automated dipping machine.

After the thin film coatings were crosslinked by EDC treatment, silver ions were bound to the carboxylic acid groups within the thin film coatings by suspending the coated magnetic particles in 5 mM aqueous solutions of Ag(Ac) for 30 min. After the metal ion loading, the magnetic microspheres were washed thoroughly with DI water three times with brief sonication. Rinsed particles were then resuspended in 1 mM $DMAB_{(aq)}$ for 15 min for reduction of Ag ions.[a,b] The coated particles after reduction were rinsed with DI water three times. For multiple loadings, rinsed particles were subjected to the original sequence of treatments.

---

[a] Essentially complete reduction of the available Ag ions in the hydrogen-bonded multilayers is achieved after 10 min as determined from the asymptotic behavior of the intensity of the surface plasmon band near 445 nm.

[b] There was no measurable loss of silver during the reduction process. Inductively coupled plasma atomic emission spectrometer measurement of the reducing agent (1 mM DMAB) showed that < 100 ppb (detecton limit) of silver is present in the solution after the reduction step. This translates to the loss of less than 4 ng of Ag per mm^2 of the multilayers.

For film thickness measurements, the multilayers were assembled on silicon wafers as described above. The thicknesses of multilayer films were then measured by a Gaertner ellipsometer equipped with a He-Ne source at 633 nm (70° angle of incidence).

Disc-Diffusion Test of Ag nanoparticle-loaded multilayers on planar supports. PAH(PAA/PAAm)$_x$ (x = 2, 5, 8, and 10) multilayer thin films were assembled on planar round substrates (22 mm in diameter). Crosslinking of these films was achieved thermally by curing the films at 90 °C for 12 hr.[48] E. Coli and S. Epidermidis were spread onto MH agar plates with cotton swabs from bacterial suspension (~ 5×10^6 cells/ml). The inoculated agar plates were allowed to dry for 5 ~ 10 min after inoculation and then the round discs with Ag-loaded multilayer films were placed on top of the inoculated MH agar. The agar plates were highly hydrated; thus, the surface tension of water in the agar ensured conformal contact between the agar plates and multilayer-coated discs. The agar plates were then inverted and incubated at 37 °C for 20 hours as shown in Figure 3.1. The zone of inhibition (ZoI), where no visible bacterial colonies formed, was measured using a digital caliper. At least three separate experiments were performed to obtain average values for each strain. For the sustained antibacterial activity study, the discs coated with PAH(PAA/PAAm)$_5$ Ag$_n$ (n = +, 1, 3) were immersed in 20 ml of pH 7.4 phosphate buffered saline (PBS) solution at 37 °C under dark conditions (to prevent auto reduction of Ag ions) and samples were taken out every 24 hours. Each disc was rinsed in DI water briefly (< 10 s) and dried before performing the disc-diffusion test with *S. Epidermidis*. It is well known that small changes in experimental conditions (e.g., bacterial strains, composition of agar medium etc.) can affect the values of zone of inhibition[96]; therefore, the data obtained in this study will not be compared with previous results by others.

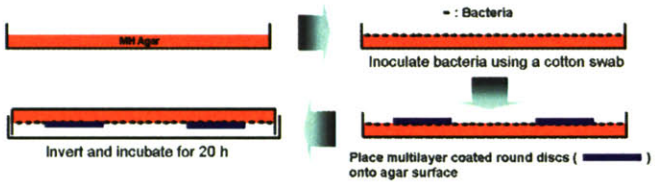

Figure 3.1. Schematic representation of Kirby-Bauer method (disc diffusion test).

Magnetic Field-Directed Delivery of Antibacterial Magnetic Particles. *E. Coli* suspension that had been incubated at 37 °C in LB broth was diluted to ~ 5×10^6 cells/ml in LB broth. 5 ml of the bacterial suspension was poured into a 6 cm-Petri dish. The bacteria were allowed to grow and adsorb onto the bottom of the Petri dish at 37 °C. After 8 hours of incubation, the LB broth was removed and the bottom of Petri dish was rinsed with a quarter-strength Ringer's solution (NH_4Cl 0.8 g, $NaHCO_3$ 0.01 g, $CaCl_2 \cdot H_2O$ 0.08 g, KCl 0.105 g and NaCl 2.25 g/L) three times to remove weakly attached bacteria. A Neodymium magnet (3 mm in diameter, K&J Magnetic, Inc.) was taped under the Petri dish in the center and the Petri dish was then filled with 5 ml of Ringer's solution and 50 µl of antibacterial magnetic bead suspension (~ 0.4 wt. %). The Petri dish was slightly agitated for a few minutes to allow the magnetic particles to be attracted to the magnet and then incubated at 37 °C for 5 hours. To distinguish between the dead and live bacteria, the bacteria were labeled with BacLight™ Bacterial viability kit and were observed under an inverted fluorescence microscope.

Determination of Minimum Inhibitory Concentration (MIC) via Agar Dilution Technique. Dilution of magnetic particles coated with Ag-loaded multilayers was achieved by a series solution technique. The concentration of the particle suspension was determined manually by using a hemacytometer. Dilutions of the Ag-loaded multilayer coated magnetic microsphere suspensions were prepared in sterile DI water at a concentration 20 times that desired in the actual test. The Luria-Bertani (LB) agar medium was sterilized and cooled down to ~ 60 °C. The diluted particle suspensions are added to the agar medium in a ratio of 1 part antibacterial particle suspension to 19

parts medium (i.e., 200 μl antibacterial particle suspension to 3.8 ml of agar). The medium was then mixed gently by inverting the tube a couple times and the mixture was poured into six-well plates. The six-well plates are then set aside and allowed to solidify at room temperature for 6 hours. Each strain of bacteria was inoculated on LB agar by streaking cotton swab from bacterial suspensions whose concentration was adjusted to ~ 5×10^6 cells/ml. The six-well plates were incubated at 37 °C for 20 hours. The MIC was taken as the lowest concentration (μg of nanocomposite-coated magnetic microparticles/g of agar, or ppm) at which bacterial growth was inhibited. The MIC measurement was done in duplicate to confirm the value of MIC for each type of bacteria.

3.3 Results and Discussion

3.3.1 Antibacterial Properties of Ag Nanoparticle-loaded Multilayers.

The antibacterial properties of hydrogen-bonded multilayers comprised of PAA and PAAm with different amounts of silver in either ionic or zerovalent form were evaluated by using the disc-diffusion test (also known as Kirby-Bauer method).[96] This test provides a means to study the influence of the film thickness as well as the amount of silver in the films on the antibacterial capability determined from the zone of inhibition. As reported in Chapter 2, the weight (or volume) fraction of Ag nanoparticles in the hydrogen-bonded multilayer films as well as the size of the Ag nanoparticles can be varied by the number of Ag loading and reduction cycles.[93] The thickness of hydrogen-bonded multilayers comprised of PAA and PAAm exhibits a non-linear growth behavior as can be seen Figure 3.3. This behavior was also confirmed by quartz crystal microbalance (QCM) measurements (Figure 3.3). The non-linear growth of multilayer films also has been observed with other systems.[101,102] Hydrogen-bonded multilayers with four different thicknesses and different numbers of Ag loading and reduction cycles were created on round discs. Since the hydrogen-bonded

system exhibits non-linear growth behavior, the use of the thickness of multilayers rather than the number of bilayers as one of the independent variables is appropriate. The round discs with the nanocomposite coatings were placed atop bacteria inoculated agar plates (Experimental section). After 20 h of incubation at 37 °C, the zone of inhibition (ZoI) was measured from the edge of the nanocomposite multilayer coated disc to the edge of the inhibited zone. Figure 3.2 shows some typical images of ZoI formed around the discs coated with Ag containing multilayers. The edge of the zone of inhibition is formed when a critical amount of Ag ions (amount that is just capable of inhibiting microbial growth) reaches a density of bacteria too large for it to inhibit.[96] Silver ions diffused out of the multilayer thin films uniformly and formed circular zones around the discs where no bacterial colonies were seen.

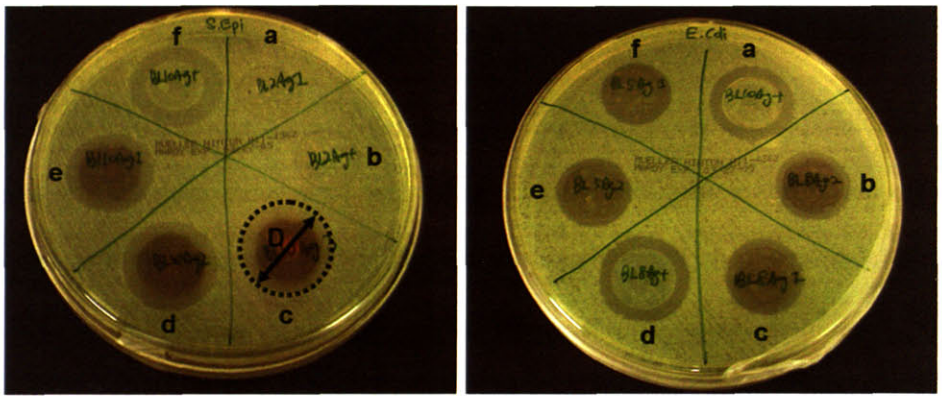

Figure 3.2. Images of MH agar plates after disc-diffusion tests were performed. *S. Epidermidis* (left) and *E. Coli* (right) were incubated for 20 hours. The zone of Inhibition is defined as [ZoI] = [D-diameter of disc (22mm)]/2. Each round disc is coated with PAH(PAA/PAAm)$_x$ Ag$_n$ films and placed on *S. Epidermidis* inoculated Mueller-Hinton (MH) agar (a) a: $x = 2$, $n = 1$, b: $x = 2$, $n = +$, c: $x = 10$, $n = 3$, d: $x = 10$, $n = 2$, e: $x = 10$, $n = 1$, and f: $x = 10$, $n = +$ and on *E. Coli* inoculated MH agar a: $x = 10$, $n = +$, b: $x = 8$, $n = 2$, c: $x = 8$, $n = 1$, d: $x = 8$, $n = +$, e: $x = 5$, $n = 2$, and f: $x = 5$, $n = 1$.

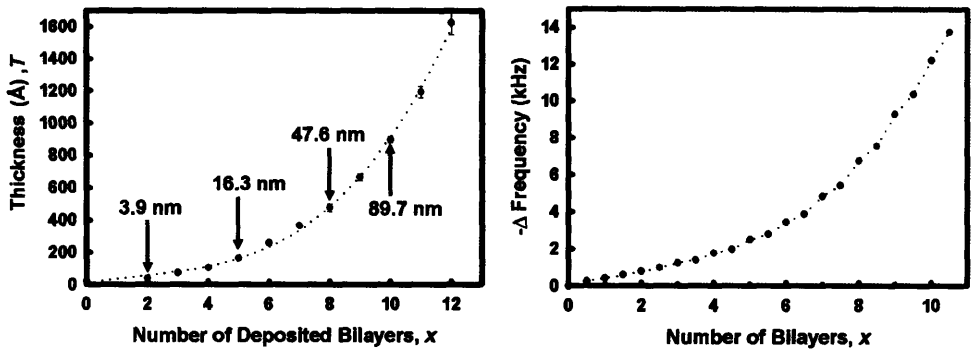

Figure 3.3. Thickness (T) (left) and frequency shift of QCM (right) of the hydrogen-bonded multilayer comprised of PAA and PAAm as a function of the number of deposited bilayers, x. Poly(allylamine hydrochloride) (PAH) was used as a primer layer to assist the adsorption of the first PAA layer. Each number in the figure indicates the thickness of x = 2, 5, 8, and 10 (PAH(PAA/PAAm)$_x$) multilayers assembled on silicon wafers, respectively. The thickness of multilayers was measured using an ellipsometer.

Figure 3.4 and Figure 3.5 show the ZoI determined by the disc-diffusion test as a function of film thickness for *E. Coli* and *S. Epidermidis*, respectively. For both types of bacteria, Figure 3.4 and Figure 3.5 show that, for a given value of n (the number of loading and reduction cycles), the experimentally determined ZoI (closed circles) increases with thickness of the Ag ion/nanoparticle-loaded multilayers. Increasing the film thickness increases the number of free carboxylic acid groups that are available within the films for Ag ion binding. The increased ZoI values for the thicker films (larger x) are consistent with a larger amount of silver ion released during incubation leading to a larger ZoI value. It is interesting to note that while the ZoI increases quite steeply as a function of film thickness below 50 nm, the increase in the ZoI slows down substantially as the thickness of films is increased above 50 nm ($x \geq 8$).

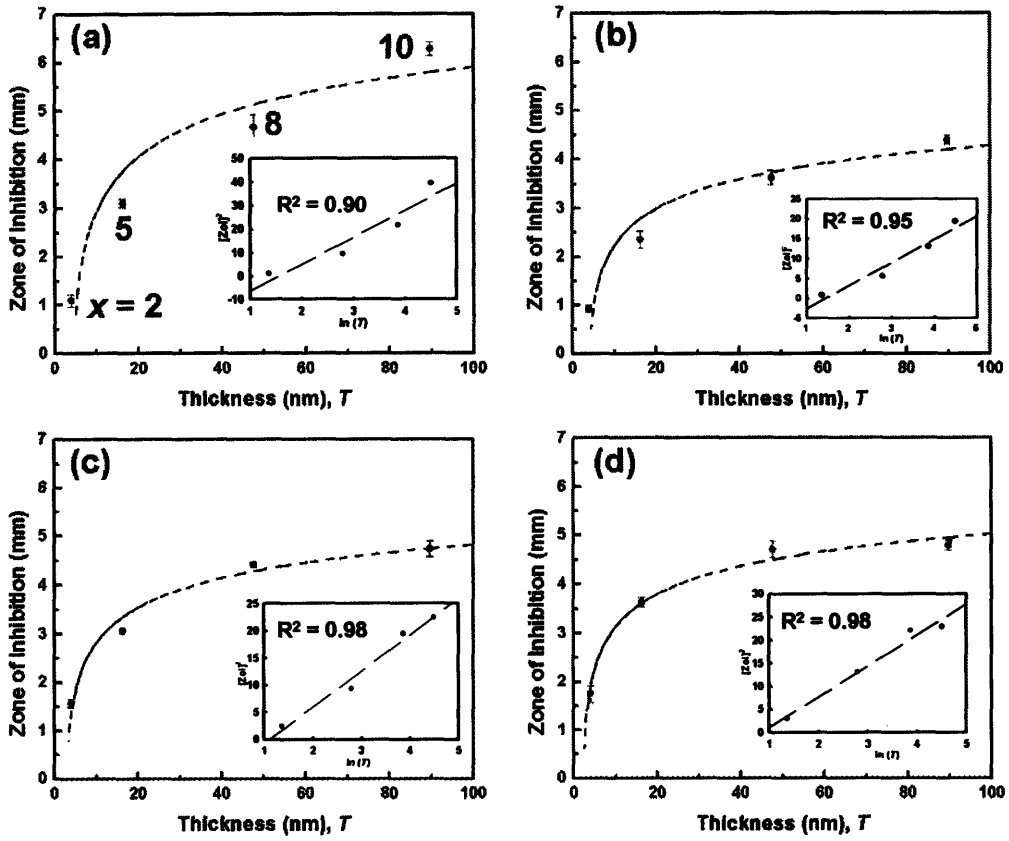

Figure 3.4. The zone of inhibition (ZoI) as a function of the film thickness (T) determined by the disc-diffusion test (•) for *S. Epidermidis* (after 20 h incubation). Error bars represent standard deviations. Figures (a), (b), (c), and (d) correspond to n = +, 1, 2, and 3, respectively. Numbers in the Figure (a) represent the number of deposited bilayers, x. Inset in each figure shows the regression line of a $[ZoI]^2$ vs. ln (Thickness) plot (dashed line) that was fitted to four points obtained from the disc-diffusion tests. R^2 values for each regression line are shown in each inset. The dotted curves in each figure were created by translating the corresponding linear regression lines in inset into the [ZoI] vs. thickness (T) linear plots.

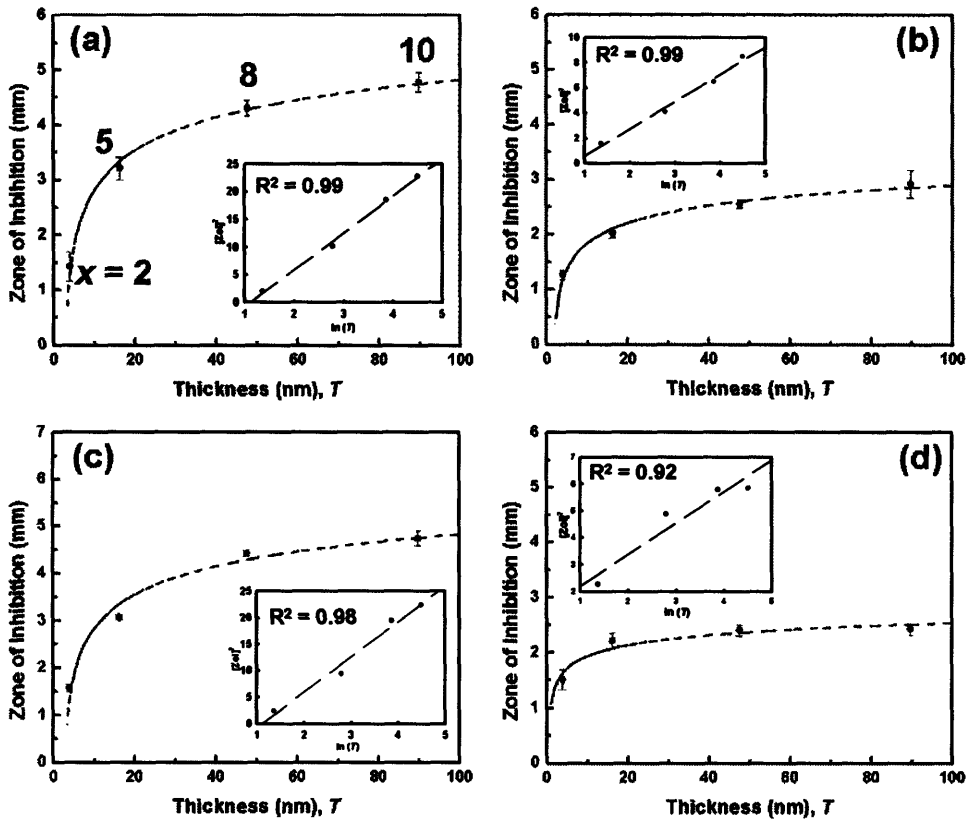

Figure 3.5. The zone of inhibition (ZoI) as a function of the film thickness (T) determined by the disc-diffusion test (•) *E. Coli* (after 20 h incubation). Error bars represent standard deviations. Figures (a), (b), (c), and (d) correspond to n = +, 1, 2, and 3, respectively. Numbers in the Figure (a) represent the number of deposited bilayers, x. Inset in each figure shows the regression line of a $[ZoI]^2$ vs. ln (Thickness) plot (dashed line) that was fitted to four points obtained from the disc-diffusion tests. R^2 values for each regression line are shown in each inset. The dotted curves in each figure were created by translating the corresponding linear regression lines in inset into the [ZoI] vs. thickness (T) linear plots.

The ZoI as a function of the film thickness can be described by a simple diffusion equation.[103,104] Assuming one-dimensional diffusion of Ag ions from the source (disc) in the radial direction, the diffusion process can be modeled by eq 3.1[103,104]:

$$\ln\left(\frac{m}{m'}\right) \sim \frac{[ZoI]^2}{Dt} \qquad (3.1)$$

where, D is the diffusion coefficient of Ag ions through the agar medium under the test conditions, t is the critical time at which point the position of the ZoI is determined (usually less than the incubation time), m' is the critical amount of Ag ions that is just capable of inhibiting microbial growth under the test condition and m is amount of Ag ions in the multilayer film. m' can be also considered as the theoretical amount of Ag ions within the multilayer below which no ZoI is formed around the disc and should represent the critical concentration at the edge of the zone of inhibition.[96] Assuming that the amount of Ag ions bound to the multilayer is proportional to the film thickness[c], the ratio of m to m' can be equated with that of film thickness (T) to "critical film thickness" (T') leading to Eq. 3.2:

$$\ln\left(\frac{T}{T'}\right) = \ln\left(\frac{m}{m'}\right) \sim \frac{[ZoI]^2}{Dt} \qquad (3.2)$$

T' can be considered conceptually as the thickness of a silver ion/nanoparticle-loaded multilayer below which no ZoI is formed. Eq 3.2 makes it possible to model the disc-diffusion test results without the information on the actual values of m or m'. It can be seen from Eq 3.2 that a plot of $[ZoI]^2$ vs. ln T should yield a straight line. A number of models have been used to describe the results obtained from the disc-diffusion test.[104] All of these models indicate that the relationship between the square of the zone of inhibition and the logarithm of the amount of antibiotic is linear as shown above. The insets in Figure 3.4 and Figure 3.5 show regression lines that have been fitted to four

---

[c] Mass uptake obtained by QCM measurements indicate that the ratio of PAA in the entire multilayer film does not vary by more than 4% for x = 2, 5, 8, and 10. Free carboxylic acid groups of PAA provide the binding sites for Ag ions.

points obtained from the disc-diffusion test. As can be seen from the R^2 values, the regression shows reasonably good linearity (i.e., $R^2 \geq 0.90$) between $[ZoI]^2$ and ln T in all cases. The observed deviations from linearity can be caused by various factors (e.g., water flow and salt movement within the agar medium) not considered by the diffusion model.[104] When these regression lines were translated to the original [ZoI] vs. thickness (T) plots (dotted curve in each figure), the curves also adequately described the trends observed. In short, the experimental data and the model indicate that in order to incrementally increase the ZoI, an exponentially increasing amount of Ag is required within the multilayers.

From the slope of each regression line, it is possible to compare the magnitude of the diffusion coefficient of Ag ions through the agar medium (slope $\sim Dt$). Although the critical time (t) is not known, it should remain constant for each bacterial strain; thus, the lumped parameter Dt can be used to compare the magnitude of apparent diffusivity, D. For either bacterial strain, the magnitude of the apparent diffusivity of Ag ions through the agar medium that is estimated from the $n = +$ data is larger than the $n = 1$ case (Table 3.1). It is believed that the decrease in apparent diffusivity is due to a slower release of Ag ions from the nanocomposite coatings when the loaded Ag ions in the film are reduced to zerovalent nanoparticles, i.e. in the case of $n \geq 1$.

Table 3.1. Values of Dt estimated from the slopes of the regression lines of ln (thickness) vs. $[ZoI]^2$ plot.

Dt (mm^2)	*S. Epidermidis*	*E. Coli*
$n = +$	12.75	6.71
$n = 1$	6.11	2.19

To compare the effect of multiple loading and reduction cycles, the values of the ZoI were plotted as a function of the number of bilayers as shown in Figure 3.6. For a given value of x (number of bilayers), multilayers that have been loaded with silver ions without the reduction step (n = +) always exhibit a larger ZoI compared to films with a single loading and reduction cycle of Ag nanoparticles (n = 1). This observation suggests that, in general, the amount of Ag ions released during the duration of the test from n = 1 samples is substantially smaller than from n = + samples for a given value of x. In the case of Ag nanoparticle-loaded multilayer thin films (i.e., $n \geq 1$), an increase in the values of the ZoI with n is observed for each x to a small extent, particularly for *S. Epidermidis* (Figure 3.6a). When Ag nanoparticles are present within the multilayers, the Ag ions that are produced at the surfaces of the nanoparticles are the source of antibacterial activity.[88] The oxidation of zerovalent Ag to Ag ions, would occur to a greater extent when a larger total surface area of silver nanoparticles is present in the nanocomposite thin films.[82,89,105] The fact that the formation of Ag nanoparticles reduces the amount of Ag ion released from the nanocomposite films (as indicated by a decrease in the values of the ZoI from n = + to n = 1) suggests that the oxidation of zerovalent Ag into Ag ions at the surface of the nanoparticles is the rate limiting step and that the diffusion of Ag ions out of the multilayers is rapid compared to the ionization process under the test condition. Cioffi et al., who studied the antifungal properties of Cu nanoparticle-containing polymer thin films, also found that the ionization of zerovalent Cu at the nanoparticle surface is the slow step compared to the Cu ion transport process within the nanocomposite films.[105]

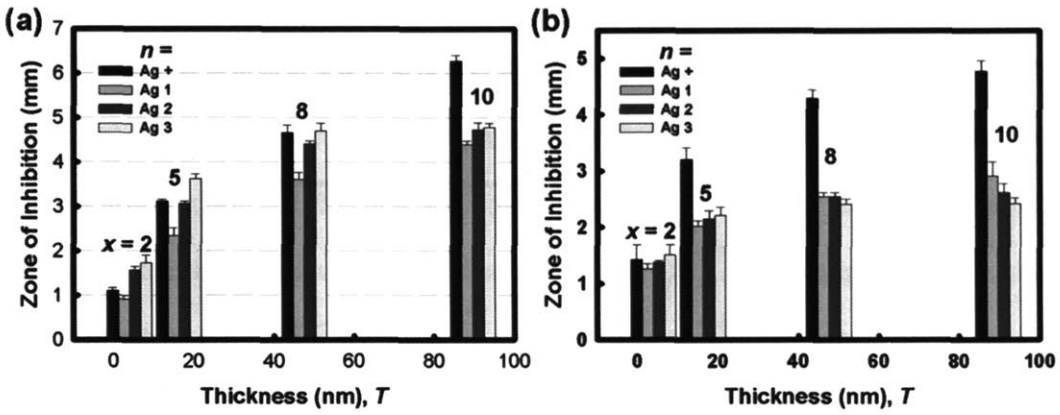

Figure 3.6. The zone of inhibition (ZoI) as a function of the number of bilayers, x for (a) *S. Epidermidis* and (b) *E. Coli.* Error bars represent standard deviations. The numbers in the legend represent n, the number of Ag loading and reduction cycles (Ag+ represents Ag ion-loaded films without the reduction step). The numbers over the bars in each figure represent x, the number of bilayers.

The weak dependence of the ZoI on n (the number of loading and reduction cycles) seen in the case of *S. Epidermidis* in Figure 3.6a also suggests that much of the added silver in successive loading and reduction cycles (for $n \geq 2$) is consumed in the growth of existing Ag nanoparticles rather than in the nucleation of new particles. Nucleation of new particles would increase the total surface area of Ag nanoparticles present within the multilayer films substantially, therefore, resulting in a larger amount of Ag ions released (a stronger dependence of ZoI on n). Previous studies based on transmission electron microscopy have also shown that nanoparticles tend to grow larger upon multiple loading and reduction cycles.[44,93] This explanation of the weak dependence of the ZoI on n, however, does not satisfactorily explain the *E. Coli* data of Figure 3.6b where no clear correlation between n and ZoI is seen. A faster growth rate of the *E. Coli* may have overwhelmed the effect of the larger total surface area of Ag nanoparticles in the multilayer matrix. The generation time (the time interval required for bacteria to divide) for *E. Coli* and *S. Epidermidis* are reported to be about

~20 and ~40 min, respectively.[106] The larger decrease in the ZoI from n = + to n = 1 seen for *E. Coli* compared to *S. Epidermidis* could also have been caused by the faster growth rate of *E. Coli*.

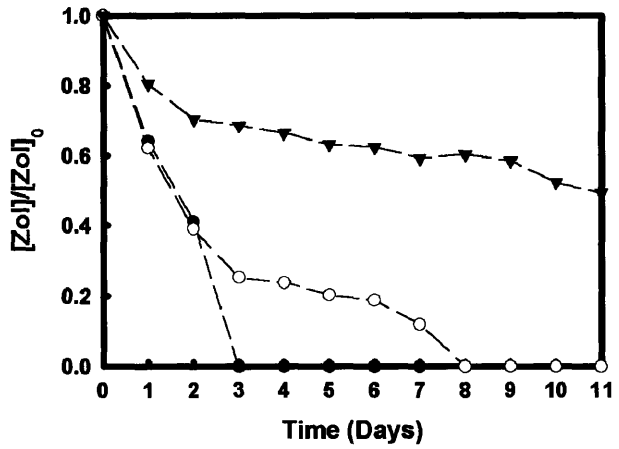

Figure 3.7. The normalized zone of inhibition of PAH(PAA/PAAm)$_5$ Ag$_n$ (n = +, 1, 3) determined for *S. Epidermidis* as a function of time in pH 7.4 PBS at 37 °C: the ZoI values were measured for n = + (●), 1 (○), and 3 (▼). $[ZoI]_0$ = 3.0, 2.5, and 3.4 mm for n = +, 1, and 3, respectively.

Sustained release of antibacterial agents is an essential property that needs to be considered in the application of antibacterial coatings. PAH(PAA/PAAm)$_5$ Ag$_n$ samples assembled on round discs with different Ag loadings (n = +, 1, 3) were tested for their sustained antibacterial properties. Samples with different Ag loadings were immersed in pH 7.4 PBS solution and incubated at 37 °C. Samples were taken out every 24 hours and the ZoI for these samples was measured with *S. Epidermidis*. Figure 3.7 shows that while the multilayers with Ag ions exhibit antibacterial activity only up to 2 days, the samples that have been loaded with a single loading of Ag nanoparticles still exhibit about 20% of their original efficacy after 6 days. These observations support the earlier contention that the zerovalent form of the Ag nanoclusters regulates the amount of antibacterial Ag ions that are being released via an oxidation step at the nanoparticle surfaces. The PAH(PAA/PAAm)$_5$ Ag$_3$ samples retained ~ 50% of their original antibacterial capability after 11

days indicating that a larger amount of zerovalent silver within the multilayers prolongs the antimicrobial activity. After 25 days, the ZoI of the PAH(PAA/PAAm)$_5$ Ag_3 multilayers decreased to ~35% (1.2 mm) of the initial value. This approach provides a means to vary the sustainability of the antibacterial effect as well as the zone of inhibition by controlling the amount of zerovalent Ag nanoparticles in the thin films via nanoreactor chemistry. To create coatings that can provide an initial burst of silver ion release followed by sustained release of the silver ions for long times, a strategy of in situ synthesizing Ag nanoparticles multiple times followed by a final loading with Ag ions without reduction would be effective.

3.3.2 Magnetically Directed Antibacterial Microparticles.

One potential application of the Ag nanoparticle-loaded hydrogen-bonded multilayers is in the targeted delivery of antibacterial silver using magnetic microparticles as the supports for multilayer assembly. Nanocomposite coated magnetic microparticles can be delivered to specific targets or separated from bulk solution by external magnetic fields. To demonstrate this concept, 2.5 μm diameter magnetic microspheres were coated with the nanocomposite coatings and directed by magnetic fields to test the localized biocidal activity. Specifically, a primer layer of PAH followed by four bilayers of PAA and PAAm were assembled at pH 3.0 onto the magnetic microparticles using either a centrifuge or a magnetic separator as the means to separate the magnetic beads from solutions. Figure 3.8 shows the variation of the zeta potential of the coated particles as a function of the number of deposited polymer layers. The original negative surface charge of the magnetic particles was overcompensated by the PAH primer layer. As reported in Section 2.3.1, the alternation of the zeta potential between two negative values after the deposition of the primer layer indicates that each polymer layer was successfully deposited onto the magnetic microspheres via a hydrogen-bonding mechanism. Recently, a similar variation in zeta-potential for a hydrogen-bonded multilayer

system involving poly(ethylene oxide) (PEO) and poly(methacrylic acid) (PMAA) was reported by Kozlovskaya et al.[107] The hydrogen-bonded multilayers on the magnetic microspheres were cross-linked using the method described in Chapter 2.[100] The color of the particle suspension became darker brown as the number of Ag loading and reduction cycles was increased, indicating that a larger amount of Ag nanoparticles was being synthesized within the multilayer coatings on the magnetic microspheres. SEM confirmed that while no significant surface topological changes took place, all the magnetic microspheres were very well dispersed without any irreversible aggregation after three loading and reduction cycles.

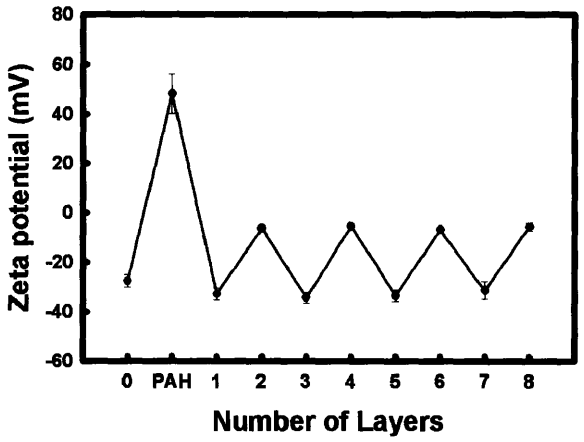

Figure 3.8. Zeta-potential variation of PAA/PAAm-coated magnetic microspheres as a function of the number of deposited layers. All measurements were made in pH 3.0 adjusted DI water. Each data point was averaged over 10 runs and the error bars represent the standard deviations.

The possibility of using the magnetic particles to deliver antibacterial silver to specific targets was tested by using a strong magnet to attract the nanocomposite-coated magnetic microspheres to a small area where bacteria had been previously adsorbed. *E. Coli* were incubated in a Petri dish and allowed to adhere to the bottom of the dish for 8 h. A strong neodymium magnet (3 mm in diameter) was placed under the center of the Petri dish followed by the addition of $PAH(PAA/PAAm)_4$ Ag_1

multilayer-coated magnetic microparticles. Figure 3.9 shows the experimental set up and the images that were taken from different locations in the Petri dish after 5 h incubation. With gentle agitation, most of the nanocomposite coated magnetic microspheres were attracted to the center of the Petri dish by the magnetic field. The fluorescence microscope image taken at location (i) in Figure 7b clearly shows that *E. Coli* on this spot are dead. Moving away from the center to the outer area of the Petri dish (from location (i) to (iii)) led to an increase in the proportion of live bacteria, whereas the proportion of dead bacteria decreased. When magnetic microspheres with silver free multilayer coatings were used in the same experimental set up, a high proportion of bacteria remained alive, and no difference was seen in the ratio of live/dead bacteria throughout the entire area of the Petri dish. Since the concentration of magnetic microspheres used in the test (~ 50 ppm) is below the minimum inhibitory concentration (discussed below) value for $PAH(PAA/PAAm)_4$ Ag_1 samples, the concentration of antibacterial silver ions throughout the bulk solution is below the concentration that is needed to kill the bacteria on the entire surface. However, by directing the magnetic microspheres with Ag nanoparticle-loaded multilayer coatings to a specific location, it was possible to increase the local concentration of antibacterial Ag high enough to achieve spatially localized antibacterial behavior.

As a potential application, these magnetic microspheres could be used to prevent the formation of biofilms in the "dead volume" of pipelines or reactors by localizing a high concentration of antibacterial silver while maintaining the concentration of Ag in the bulk fluid to a minimal value. This approach eliminates the need for a high dosage of antibacterial agent throughout the entire system. Also, these magnetically manipulable antibacterial particles can be removed readily from pipelines or reactors by using magnetic fields. Although silver is known to have excellent antibacterial properties, reports have shown that a high concentration of silver can be toxic to certain mammalian cells.[89,108] By optimizing the size and the biocompatibility of core particles,[109,110]

the magnetic microparticles with Ag nanoparticle-loaded multilayer coatings could be used to deliver antibacterial Ag to specific regions of the human body while keeping the concentration of Ag low except in the immediate vicinity of the target.

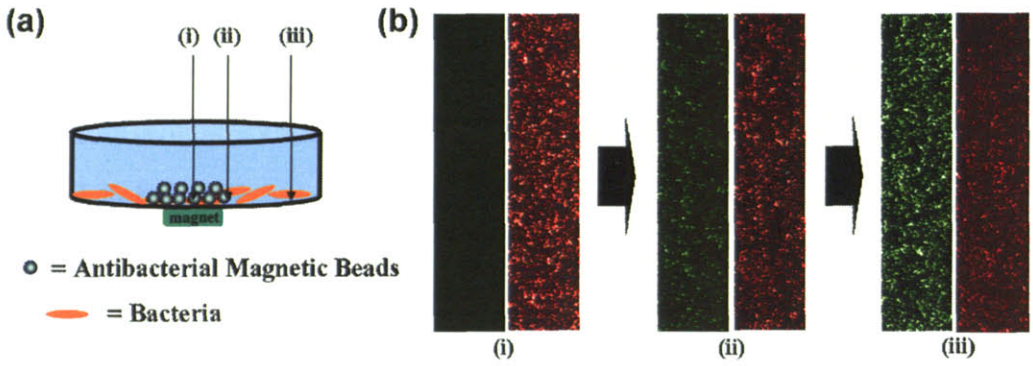

Figure 3.9. Localized delivery of PAH(PAA/PAAm)$_4$ Ag$_1$ coated 2.5 μm magnetic microparticles by magnetic fields: (a) the scheme of the experimental set-up and (b) fluorescence microscope images taken from different locations (marked by Roman Numerals) in the Petri dish. Each pair of red and green images was taken from the same location. Live and dead *E. Coli* were stained with green and red fluorescence dyes, respectively. Distance from spot (i) to (ii) and (iii) are ~ 3 mm and ~ 15 mm, respectively. The width of each image is 60 μm.

From a practical point of view, it would be important to determine the lowest concentration of antibacterial agent (in this case, the concentration of the nanocomposite coated magnetic particles) that is required to completely inhibit the growth and survival of bacteria. This concentration also known as the minimum inhibitory concentration (MIC) was determined by the agar dilution technique.[96] Ag nanoparticle-loaded multilayer coated magnetic microspheres were incorporated into a liquefied LB agar medium which was then mixed and solidified. Bacteria were inoculated onto the agar plates. After overnight incubation (20 h), the MIC values were read as the lowest concentrations which completely inhibit the growth of bacterial colonies. Figure 3.10 shows an image of the agar plates used in the MIC determination. It can be seen that above a certain

concentration of antibacterial particles with varying amount silver, no colonies is observed indicating that the growth of bacteria was completely inhibited. Table 3.2 summarizes the MIC of magnetic microspheres with different concentrations of Ag nanoparticles. For both types of bacteria, magnetic microspheres with higher loadings of Ag nanoparticles had lower MIC values. Bare magnetic microparticles as well as microparticles with hydrogen-bonded multilayers (no Ag) did not show any biocidal activity up to 2000 ppm. These results show that the layer-by-layer assembly of polymers in conjunction with nanoreactor chemistry is a versatile approach to render colloidal particles antibacterial. The values of the MIC indicate that only a small amount of coated material would be needed as an additive to keep various suspension-based coatings such latex paints and pigments antiseptic. As a comparison, the MIC for commercially available antibacterial particles is approximately 800 ppm.[83]

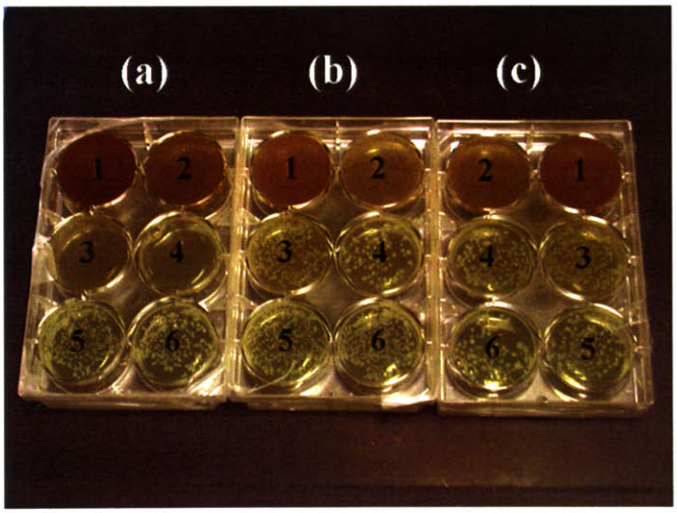

Figure 3.10. Image of plates used in the agar dilution technique performed after 20 hr of *E. Coli* incubation. (a), (b) and (c) agar mixtures are made from a mixture of PAH(PAA/PAAm)$_4$ Ag_3, PAH(PAA/PAAm)$_4$ Ag_+, and PAH(PAA/PAAm)$_4$ Ag_1 suspension and LB agar, respectively. In the each 6-well plate, the concentration of magnetic particles with Ag nanocomposite coatings decreases from 800 ppm (well #1) to 25 ppm (well #6) by half dilutions.

Table 3.2. The minimum inhibitory concentration (MIC) values of the antibacterial magnetic microspheres determined by the agar dilution technique.

Samples	*E. Coli*	*S. Epidermidis*
PAH(PAA/PAAm)$_4$ Ag$_+$	400 ppm	400 ppm
PAH(PAA/PAAm)$_4$ Ag$_1$	400 ppm	400 ppm
PAH(PAA/PAAm)$_4$ Ag$_3$	100 ppm	200 ppm

3.4 Conclusions

Antibacterial coatings based on hydrogen-bonded multilayers containing in-situ synthesized Ag nanoparticles were created on planar surfaces and on magnetic colloidal particles. Both Gram-positive strain (*S. Epidermidis*) and Gram-negative strain (*E. Coli*) bacteria were susceptible to the biocidal activity of Ag nanoparticle-loaded multilayer thin films. The zone of inhibition (ZoI) determined by the disc-diffusion test increased as the thickness of the multilayer film was increased. The observed trends could be successfully described by a simple diffusion model. (i.e., the square of the zone of inhibition (ZoI) depended linearly on the logarithm of the thickness of the silver-loaded films). My observation and the diffusion model indicated that incremental expansion of the ZoI requires exponentially increasing amounts of silver to be released from the films. In general, the effect of multiple silver loading and reduction cycles did not have a statistically significant effect on the zone of inhibition; the duration of silver release, however, is strongly dependent on the total amount of zerovalent Ag nanoparticles in the films and increases with the number of loading and reduction cycles at a given thickness. These results are consistent with: (1) a mechanism in which oxidation of zerovalent Ag to Ag ions at the nanoparticle surfaces is the rate limiting step, and Ag ion

transport is fast in the hydrated multilayer films, and (2) a mechanism in which repeated loading and reduction of silver leads preferentially to growth of the existing silver nanoparticles in the film as opposed to nucleation of new Ag nanoparticles. When these coatings were applied to the surfaces of magnetic microspheres, the bactericidal effect determined by the minimum inhibitory concentration in the agar dilution technique increased as the total amount of Ag nanoparticles was increased within the thin film coatings. It is possible to achieve localized antibacterial action by directing the nanocomposite coated magnetic microspheres to a specific location. In the future, bimetallic nanocomposite coatings containing both copper[105] and silver or platinum and silver[111] nanoparticles will be studied for their antimicrobial properties against fungi as well as bacteria.

Chapter 4

pH-induced Hysteretic Gating of Track-Etched Polycarbonate Membranes: Swelling/Deswelling Behavior of Polyelectrolyte Multilayers in Confined Geometry

4.1 Introduction

Porous membranes that change their permeation/separation properties in response to environmental stimuli have been focus of research for the last few decades.[31,112-134] Permeation properties of these membranes can be controlled by changing pH[31,112,113,116,118,121-123,127], temperature[124,125,128,129], electric field[130,133,134], concentration of chemical species[119,131] or ionic strength[113,132] of their environments. Potential applications for these stimuli-responsive membranes include controlled drug delivery, wastewater treatment, chemical sensors and the separation of macromolecules including biological molecules such as proteins.

One of the most widely utilized approaches to create stimuli-responsive membranes is to graft polymer chains such as weak polyelectrolytes onto the surfaces of porous membranes. Ito et al. have demonstrated that it is possible to create pH-responsive membranes by surface graft polymerization of a weak polyacid onto track-etched polycarbonate (TEPC) membranes.[115-117] Also polypeptides that exhibit conformation changes as a function of environmental pH have been grafted to the surface of TEPC membranes to create stimuli-responsive membranes.[117,118] Mayes et al. also have reported a one-step fabrication of pH-responsive membranes by immersion precipitation with no post-coagulation processing steps.[127] In these pH-responsive membranes, the degree of ionization of a

weak polyelectrolyte changes as a function of environmental pH; the chain conformation, hence, changes as a function of pH and controls the permeation and separation properties of porous membranes providing a "mechanochemical valve". Using the approach of surface graft polymerization, stimuli-responsive membranes that can respond to changes in environmental temperature, light, concentration of chemical species and redox properties also have been created. [112-119,122-125,129,132] Other approaches to create stimuli responsive membranes include the methods introduced by Martin and coworkers where gold nanotube membranes are utilized to modulate the transport properties of ions and organic molecules.[31,133,134]

While surface graft polymerization of polymers provides a useful means to create stimuli-responsive membranes, it is often difficult to precisely and reproducibly control the grafting density and degree of polymerization of grafted chains in the confined geometries of porous membranes.[113,120,127] In addition, most, if not all, of the stimuli responsive membranes generated to date via surface graft polymerization or other approaches show a non-hysteretic response to stimuli. This means that, while it is possible to achieve changes in the permeation properties by changing environmental conditions such as pH condition, ionic strength and temperature, it is not possible to achieve either an "open" or "closed" state at one specified condition. Having "open" or "closed" states at one specified condition will be preferred for various applications that involve filtration of materials that are stable only in a narrow range of pH conditions. For example, most proteins are only stable in narrow pH ranges (pH 6 – 8).[135] Also, many types of nanoparticles, which have stabilizing agents on their surfaces, can only retain their colloidal stability in certain pH conditions[136]; therefore, it would be advantageous to use membranes that can filter or allow the passage of these pH-sensitive proteins or nanoparticles within the narrow pH ranges where their stability is maintained.

Layer-by-layer (LbL) assembly of polymers based on electrostatic or hydrogen-bonding interactions provides a versatile means to engineer and modify the physical and chemical properties of various surfaces including planar supports, colloidal particles and porous membranes.[17,26,27,137-139] By choosing appropriate processing conditions and materials, it is possible to create polymer thin films that are responsive to various environmental stimuli such as ionic strength, pH and temperature.[140] In particular, polyelectrolyte multilayers comprising weak polyelectrolytes offer a great advantage in creating stimuli-responsive polymer thin films.[40,50,140-142] A number of studies have shown that the permeation properties of multilayer hollow microcapsules containing weak polyelectrolytes can be controlled by various stimuli including temperature, ionic strength and pH conditions.[143-147] It also has been shown that by creating thin films of weak polyelectrolyte multilayers atop nanoporous anodized aluminum oxide (AAO) membranes or on planar electrode surfaces, ion diffusion characteristics can be modulated.[28,148-151] Sukhishvili et al. recently showed that by depositing thermoresponsive hydrogen-bonded multilayers onto AAO membranes, the permeation of dyes could be controlled by changes in the temperature.[147] Hollman and Bhattacharyya also have assembled multilayers comprising polypeptides in the pores of track-etched polycarbonate membranes for enhanced ion separation.[152]

In this chapter, pH-responsive membranes that show discontinuous changes in the permeation properties will be described. The responsive membranes are produced by depositing polyelectrolyte multilayers on the inner pore walls as well as on the surfaces of track-etched polycarbonate membranes. Rubner et al. have recently demonstrated that polyelectrolyte multilayers comprising a strong polyanion, poly(sodium 4-polystrene sulfonate) (PSS) and a weak polycation, poly(allylamine hydrochloride) (PAH), assembled at a high pH condition (pH > 9.0) show discontinuous swelling/deswelling transitions as a function of pH conditions.[50,141] These reversible discontinuous transitions are induced by discontinuous changes in the degree of ionization of free

amine groups of PAH and a dramatic shift in the pK_a value of PAH due to its local environment (hydrophobic association of free amine groups) within the multilayers.[39,141] Such a mechanism leads to a history-dependent swelling behavior of these multilayers. The swelling/deswelling behavior of these multilayers in a confined geometry based on simple models that enable the calculation of the pore diameters from the experimental flux values will be investigated. I also demonstrate that it is possible to filter or allow the passage of high molecular weight polymers at the same pH condition utilizing the hysteretic gating properties of these membranes, demonstrating the proof-of-concept of achieving an "open" or "closed" state at a single pH condition depending on pretreatment conditions. The hysteretic gating of membranes overcomes one of the problems of conventional (non-hysteretic) stimuli responsive membranes in that, one membrane can be use to allow either retention or passage of pH-sensitive materials. This study is the first demonstration of hysteretic gating of porous membranes as well as the first study of swelling behavior of polyelectrolyte multilayers in a confined cylindrical geometry.

4.2 Experimental Methods

Materials. Poly(allylamine hydrochloride) (PAH) (M_w = 70 000), poly(sodium 4-styrenesulfonate) (PSS) (M_w = 70 000) and poly(ethylene oxide) (PEO) (M_v = 2 000 000) were purchased from Sigma-Aldrich and used as received. Viscosity-average molecular weight (M_v) of PEO was determined by measuring the intrinsic viscosity ($[\eta]$) of PEO in water at 20 °C and using the relation $[\eta] = 2.0 + 0.016\ M_v^{0.76}$.[153] The nominal molecular weight of PEO provided by the manufacturer was 5 000 000. Track-etched polycarbonate membranes (25 mm in diameter) whose pore diameters are 400 and 800 nm were purchased from Sterlitech.

Modification of track-etched polycarbonate membranes with polyelectrolyte multilayers. Polyelectrolyte solutions of 10 mM (based on the repeat unit molecular weight) were prepared from

deionized (DI) water (18 MΩ·cm Millipore), and the pH of both polyelectrolyte solutions and the rinse water were adjusted to pH 9.3 with 1 M NaOH. Unless otherwise noted, all the (PAH/PSS) multilayers were assembled at pH 9.3 in this study. The pH of both the assembly solutions and swelling solutions was monitored to ensure that a significant drift in pH did not occur during experiments. The drift in pH was typically less than 0.2 units. If the drift exceeded this amount, the solution was replaced with fresh solution. Polyelectrolyte multilayers were assembled onto track-etched polycarbonate (TEPC) membranes at room temperature (19 ~ 20 °C, relative humidity ~ 30 %) by using an automated HMS programmable slide stainer (Zeiss, Inc.). Polyelectrolyte multilayers were deposited by dipping into the polycation (PAH) solution and the polyanion (PSS) solution alternately (for 20 min each) with dips in pH-adjusted water rinsing in between (for 2, 2, and 1 min before the next dip into a polyelectrolyte solution). The role of the rinse steps is to remove loosely bound and unbound polyelectrolytes from the pores of the TEPC membranes. Dipping and rinsing steps were repeated until the predetermined number of bilayers was deposited. (corresponding to 18.5 and 6.5 bilayers on 800 and 400 nm pore TEPC membranes, respectively). A pair of (PAH/PSS) depositions will be referred to as one bilayer.

Flux measurement. Flux measurements were performed on 25 mm diameter TEPC membranes using an Amicon 8010 dead-end filtration cell (Millipore) having an effective filtration area of 4.1 cm^2. pH-adjusted deionized water was delivered from a stainless steel dispensing vessel (Millipore) pressurized with nitrogen gas as shown in Figure 4.1.

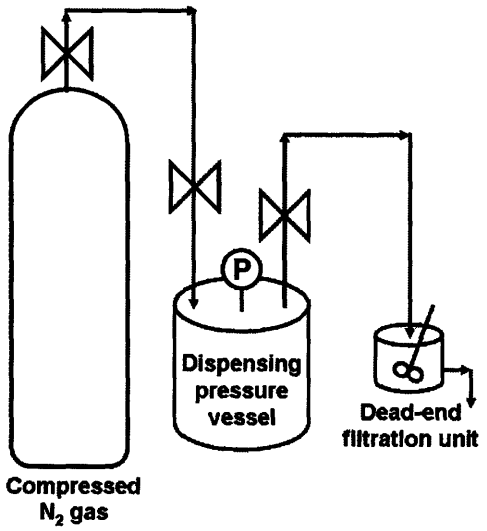

Figure 4.1. Experimental set-up of permeation cell for flux measurement.

Polyelectrolyte multilayer modified TEPC membranes were pretreated by soaking the membranes in either pH 2.5 or pH 10.5 adjusted water for 3 min. After the pretreatment, the membranes were dried in the air for 2 ~ 3 min and then loaded into the filtration cell. The cell and the pressure vessel were filled with pH adjusted water and pressurized to 20 and 10 psi for 800 and 400 nm pore membranes, respectively. Each measurement consisted of a 3-min equilibration period, followed by a gravimetric flux measurement over a 3 minute period. All of filtration steps and flux measurements were performed at room temperature with a stirring speed of ~ 500 rpm. For reversibility tests, the trans-membrane flux was measured during 5 cycles consisting of a pH 10.5 measurement followed by a pH 2.5 measurement. Each measurement consisted of a 3-min equilibration followed by a 3-min gravimetric flux measurement. Flux (J) was calculated from the following relation:

$$J = \frac{V}{A_m \cdot t}\left[\frac{ml}{cm^2 \cdot \min}\right] \qquad (4.1)$$

where, V is volume of pH-adjusted water collected during 3 min, A_m is the superficial area of the TEPC membrane (4.1 cm^2) and t is the time of collection which was 3 min. For filtration experiments, a dilute solution (0.01 g/dL) of PEO dissolved in deionized water (pH 5.5 ~ 6.0) was filtered with pH 2.5 or 10.5 pretreated membranes. During each filtration experiment, the pressure was adjusted so that the flux was maintained at ~ 0.01 ml/(cm^2·min). The concentration of filtrate solution was determined by measuring the relative viscosity by using a Cannon-Fenske viscometer (size 100). A calibration curve was obtained beforehand with polymer solutions of known concentrations.

Multilayer film characterization. The degree of swelling on planar Si (100) wafers was obtained using in situ ellipsometry as previously reported.[141] A spectroscopic ellipsometer (M-2000D, J. A. Woollam Co., Inc.) was used and the data were fitted to a Cauchy model.[154] A refractive index of 1.33 was used for water during in-situ ellipsometry. A self-built fluid cell based on a design described in the literature was used.[155] Measurements were made after a 3 min pretreatment either in pH 2.5 or 10.5 adjusted water followed by drying with blown air and then 3 min equilibration in pH-adjusted water.

To measure the multilayer growth in pores of track-etched polycarbonate membranes, scanning electron microscopy (SEM) was performed on a JEOL 6320 FEG-SEM operating at 2.0 kV. Cross-section transmission electron microscopy (TEM) images were generated on a JEOL 200CX operated at 200 kV. Multilayer-coated membranes were first stained with 1 mM sodium tetrachloropalladate (Na_2PdCl_4) solution and then embedded in epoxy (Electron Microscopy Sciences). Ultrathin sections (50 ~ 70 nm) for TEM observation were microtomed at room temperature with a diamond knife using a RMC MT-X ultramicrotome and collected on copper grids.

In-situ atomic force microscopy was performed under pH-adjusted water by a Molecular Imaging Pico Plus SPM. Contact mode with a Si_3N_4 cantilever was used to scan a 10 μm square area of the film in pH-adjusted deionized water.

4.3 Results and Discussion

4.3.1 Growth of (PAH/PSS) multilayers in cylindrical pores of TEPC membranes.

Growth of multilayers comprising PAH and PSS was studied by scanning electron microscopy (SEM) and transmission electron microscopy (TEM). (PAH/PSS) multilayers were deposited onto 800 nm pore TEPC membranes at pH 9.3. Figure 4.2 shows SEM images of the pores at various stages of multilayer deposition. The diameter of pores decreased as the number of deposited layers increased (Figure 4.3 (a)), and no clogging of the pores was observed up to 24.5 bilayers. As can be seen in Figure 4.3(b), the thickness of multilayers grown within the pores of TEPC membranes (estimated from SEM images in Figure 4.2) is larger than those grown on planar Si wafers for a given number of bilayers deposited (determined via ellipsometry). Also the difference in the thickness increases with the number of bilayers deposited onto each substrate. Previous studies by others also have observed thicker multilayer growth in cylindrical pores of anodized aluminum oxide (AAO) membranes and polycarbonate membranes.[29] In this case, since the SEM images only show the face of the multilayer coated membranes, the multilayer growth could be greater around the entrance regions of the cylindrical pores compared to the inner regions of the pores. Also, the nature of the substrate (Si wafer vs. TEPC membrane surface) could have an effect on the growth behavior of multilayers, a result that has been observed previously by others.[156] To address both of these issues, cross-sectional TEM studies of the multilayer-coated membranes were carried out.

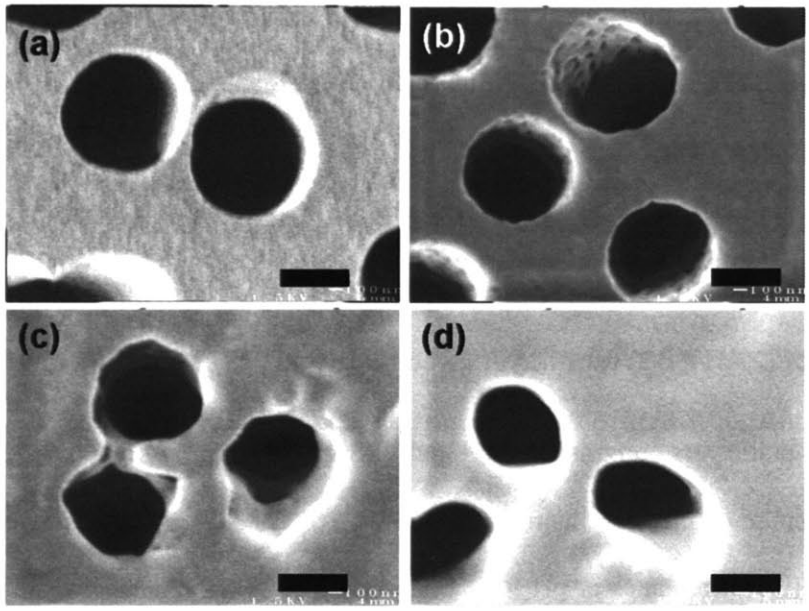

Figure 4.2. SEM images of (PAH/PSS) multilayer coated TEPC membranes. (a) 0, (b) 8.5, (c) 14.5 and (d) 20.5 bilayers of (PAH/PSS) multilayers deposited at pH 9.3 onto 800 nm pore TEPC membranes. (Scale bar = 500 nm)

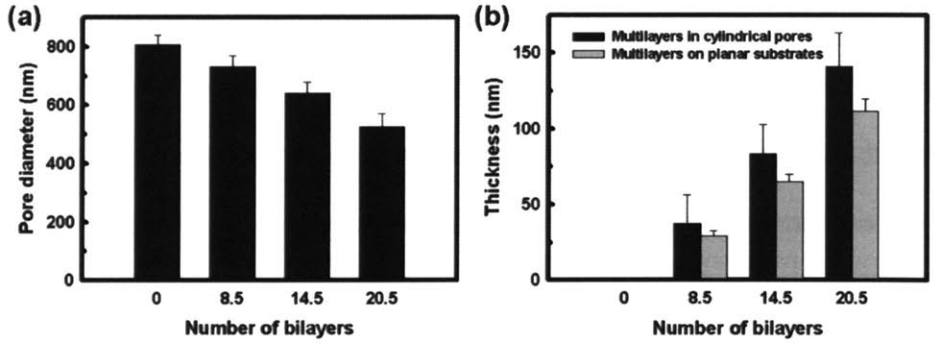

Figure 4.3. Changes in the (a) average pore diameters and (b) the thickness of multilayers in the pores of TEPC estimated from SEM images. Black bars represent the thickness of multilayers in the cylindrical pores of TEPC membranes and gray bars represent the thickness of multilayers on planar Si substrates. Diameters of at least 50 pores were measured for averaging.

Cross-sectional TEM images in Figure 4.4 clearly show that the thickness of a multilayer film assembled on the interior of the pores is larger than that on the face of the TEPC membranes; the

same multilayer comprised of 24.5 (PAH/PSS) bilayers on planar Si wafer has a thickness of 155 nm, in comparison to the approximate thickness of 250 nm seen in the membrane pores. This result shows that neither the nature of the surface nor an entrance effect is contributing to the enhanced growth behavior of multilayers in TEPC membrane pores. The small difference in the thickness of multilayers on planar Si wafers (155 nm) and on the face of the TEPC membrane (~ 175 nm) could be attributed to the difference in the thickness measurement techniques (i.e., cross-sectional TEM vs. ellipsometry)[44]. Others have suggested that the conformational changes induced by a curved surface may lead to enhanced growth of multilayers[29]. The conformation of polymer chains, however, was most likely not affected by the curvature of the pores since the size of pores in this study is much larger than the radius of gyration (~ 10 nm) [157,158] of the polyelectrolytes used.

The incomplete drainage of solutions during the layer-by-layer deposition process is believed to cause the larger growth behavior within the cylindrical pores. On planar substrates (e.g., Si or glass substrates) that are held vertically during the LbL process, it is often observed that due to the incomplete drainage of solutions on the bottom portion of the substrates during the deposition steps, the multilayers are thicker in this part of the substrate than in the uniform regions. Capillary forces that act on solutions within the cylindrical pores of TEPC membranes during the LbL process can lead to a similar effect, causing multilayers to grow thicker within the pores. Incomplete drainage, however, does not necessarily indicate that residual polyelectrolytes are left in the pores during the rinse cycles of the LbL process. The characteristic diffusion time for polyelectrolyte chains to travel through the cylindrical pores estimated from a simple scaling argument ($\tau_{diff} \approx L^2/D$, where $D \sim 10^{-7}$ cm^2/s for polymer chains whose radius of gyration is ~ 10 nm[157]) is on the order of 10 s. Therefore, during the rinse cycles, which lasted 2, 2 and 1 min, any residual polyelectrolyte chains should be removed. The mechanism underlying the observed enhanced growth due to incomplete drainage of solution during the LbL process is, however, still unclear.

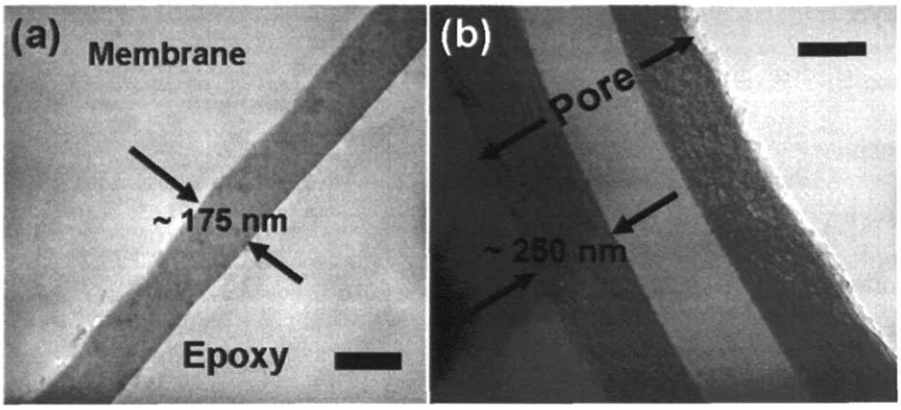

Figure 4.4. Cross-section TEM images of 24.5 (PAH/PSS) bilayers (a) on the planar surface of the TEPC membrane and (b) in the pore of the TEPC membrane. (Scale bar = 200 nm)

4.3.2 Hysteretic gating and swelling/deswelling behavior of the multilayers in confined geometry.

Hysteretic gating and discontinuous swelling/deswelling behavior of (PAH/PSS) multilayers in the pores of TEPC membranes were studied by measuring the flux of pH adjusted-water through these membranes. 18.5 bilayers of (PAH/PSS) multilayers were deposited onto the 800 nm pore TEPC membranes. A membrane was pretreated by soaking it in either pH 2.5 or 10.5 adjusted water for 3 min. After the pretreatment, a 3-min equilibration in pH-adjusted water was followed by a 3-min gravimetric flux measurement. Figure 4.5 shows the changes in flux as a function of pH treatment. A large discontinuous hysteresis loop in the flux is observed. After the pH 10.5 pretreatment, the multilayers within the pores of the TEPC membranes are only slightly hydrated down to a pH of about 5.0; therefore, the pores of the TEPC membranes remain "open". However, as the pH condition of water that is permeated through the membranes is further lowered, the multilayers undergo a swelling transition which, in turn, effectively "closes" the pores. For the case of the multilayer-modified membranes that are pretreated at pH 2.5, the multilayers within the pores of the TEPC membranes retain their swollen structure up to pH 9.0; hence, the pores are "closed" and the

flux is extremely low. It should be noted that the values of flux measured for the "closed" states are not equal to zero and are quantitatively in the range of about 0.2 ml/(cm^2·min), smaller than the flux in the "open' state by a factor of about 500. At a pH environment higher than 9.0, the multilayers begin to deswell and open up the pores. These results confirm that the discontinuous swelling/deswelling transitions that were observed on planar substrates[47,141] can also be realized in the sub-micron pores of TEPC membranes. Taking advantage of the LbL process, the difference in the trans-membrane flux between the open and closed states (the vertical gap of the hysteresis loop) can be easily varied by changing the number of bilayers deposited and the original diameter of the pores in the TEPC membranes as shown in Figure 4.6. It should be noted that in all cases multilayers were characterized within 24 h after their preparation. Previous studies have shown that these multilayers slowly, over a period of days and weeks, undergo molecular rearrangements, especially in a moist environment, that prevent multilayers from achieving its high level of swellability.[50,141] Multilayers' ability to gate the pores of TEPC membranes has been correspondingly observed to diminish as a result of this molecular reorganization. The stability of the multilayers can be maintained, however, by storing the multilayer-modified membranes in dry conditions (e.g., vacuum) as mentioned by Itano et al.[141]

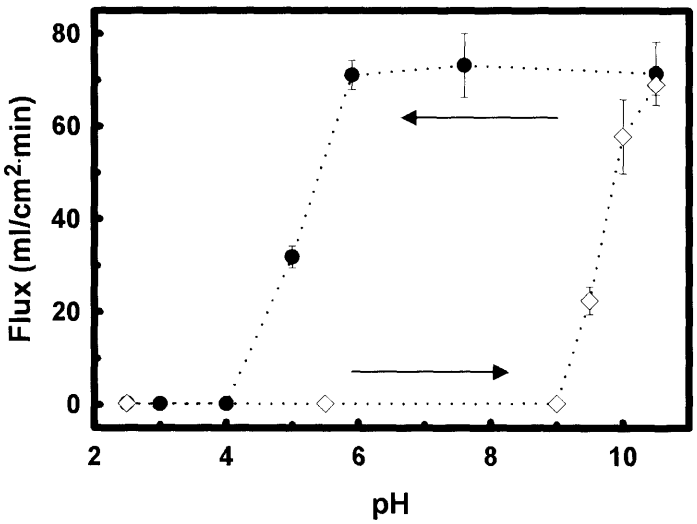

Figure 4.5. Changes in flux as a function of pH. The filled circles and open diamonds represent data generated after a pH 10.5 pretreatment and after a pH 2.5 pretreatment, respectively. Error bars represent standard deviations.

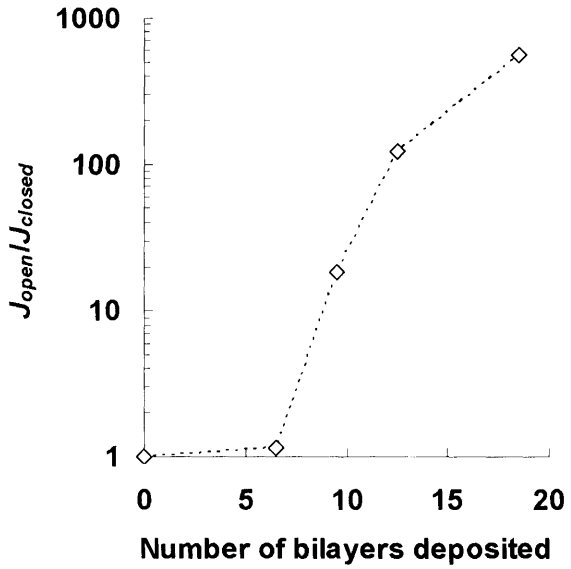

Figure 4.6. The ratio of flux of open state (J_{open}) to flux of closed state (J_{closed}) as a function of number of deposited bilayers in the pores of 800 nm pore TEPC membranes. J_{open} and J_{closed} were measured with de-ionized water (pH 5.5 – 6.0) flowing through the membranes after multilayer-modified 800 nm pore TEPC membranes were pretreated at pH 2.5 and pH 10.5, respectively.

A more quantitative analysis of the phenomena described above would provide valuable information about the swelling/deswelling behavior of (PAH/PSS) multilayers in a confined geometry. To estimate the size of pores in the open and closed states, the well-established Hagen-Poiseuille (HP) equation was first used[159]:

$$\frac{Q}{A_m} = J = \frac{n\pi(D/2)^4 \Delta P}{8\eta L} \tag{4.2}$$

where Q is the volumetric flow rate, A_m is the external membrane area, J is the flux, n is the number of pores per unit area of membrane, D is the average pore diameter, η is the fluid viscosity, ΔP is the pressure difference across the membranes and L is the average length of the pores. Therefore, at constant ΔP, the trans-membrane flux should depend on the pore diameter according to the following relation:

$$\frac{D}{D_{ref}} = \left(\frac{J_{\exp}}{J_{ref}}\right)^{1/4} \tag{4.3}$$

By measuring the trans-membrane flux of bare 800 nm pore TEPC membranes (reference state), the pore diameters (D) of multilayer-modified membranes under different pH conditions can be estimated from the experimentally measured flux (J_{exp}).

Figure 4.7 shows the discontinuous transitions in the pore diameter of multilayer-modified TEPC membranes as a function of pH conditions as estimated from the HP equation. As expected, the pore diameters decrease significantly in the "closed" states reducing the flux of water through the membranes. However, the estimated pore diameter in the open state is about 700 nm, whereas the pore diameter measured from SEM is approximately 600 $\pm$ 26 nm. Previous studies that utilized the HP equation to estimate the size of cylindrical capillaries of TEPC membranes have shown that this equation over-estimates the size of pores of these membranes.[160-162] Also the HP equation

assumes that the multilayers are impenetrable to water; however, ample evidence in the literature supports the fact that polyelectrolyte multilayers are highly permeable to water.[163] Therefore, by making the assumption of impermeable multilayers, especially in the swollen state, the pore diameters would be overestimated.

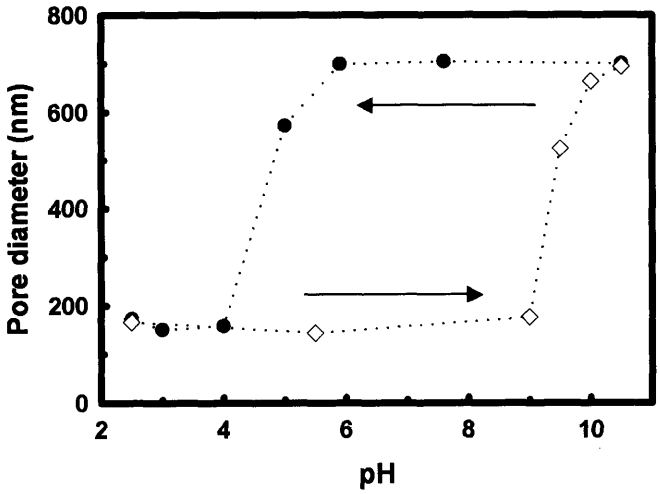

Figure 4.7. Changes in the pore diameter as a function of pH estimated from Hagen-Poiseuille equation. The filled circles and open diamonds represent data generated after a pH 10.5 pretreatment and after a pH 2.5 pretreatment, respectively.

To account for permeation of water through the hydrated multilayers, a two-region flow (TRF) model (see Appendix A for details) is employed. This model has been used to model the flow of water through polymer brush grafted TEPC membranes.[164,165] Figure 4.8 shows the estimated pore diameter from the TRF model. The pore diameter (~ 120 nm) in the "closed" state obtained from the TRF model is smaller than that predicted by the HP equation (~160 nm). Figure 4.9 shows that, in the "closed" state (calculated for a solution of pH 5.5 after a pH 2.5 pretreatment), the velocity of water permeating through the hydrated multilayers is extremely small (ca 1.9×10^{-3} cm/sec) compared to that of water in the physically open region (i.e., multilayer-free region where the typical

maximum value is ca. 1.2 cm/sec). However, the fraction of the total flux that passes through the hydrated region is nearly 0.13 since the hydrated multilayer region covers about 98 % of the cross-sectional area of the pores. While it is not expected that the values of the pore diameters estimated by the TRF model or HP equation to be quantitatively exact as both models were employed on a number of assumptions, the values from the TRF model and HP equation qualitatively provide plausible ranges for the dimensions of the constricted pores from the flux experiments.

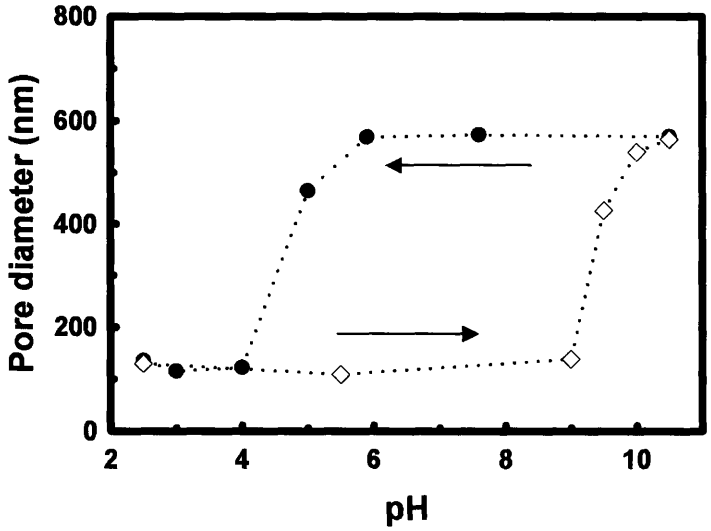

Figure 4.8. Changes in the pore diameter as a function of pH estimated from two-region flow (TRF) model. The filled circles and open diamonds represent data generated after a pH 10.5 pretreatment and after a pH 2.5 pretreatment, respectively.

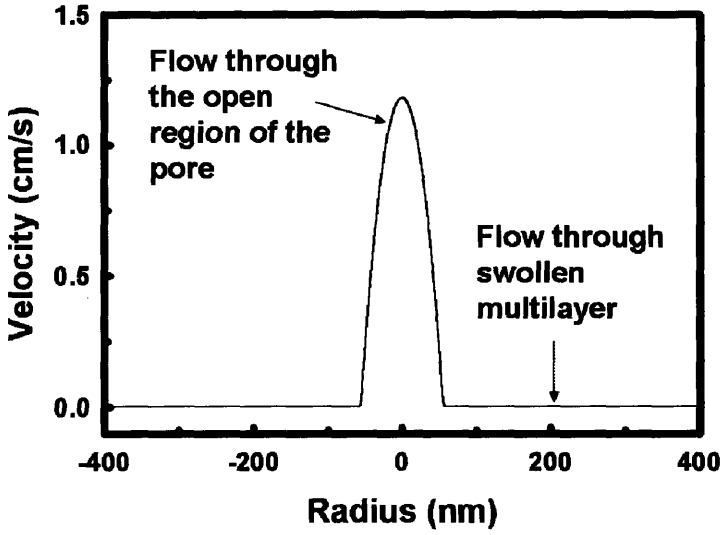

Figure 4.9. Velocity profile of water flowing through a cylindrical pore in closed state. The velocity profile was calculated based on the TRF model from experimental flux values taken from a pH 5.5 solution after a pH 2.5 pretreatment. The radius of the unmodified pore is 400 nm.

The swelling behavior of the (PAH/PSS) multilayers on planar Si wafers and within the cylindrical pores of TEPC membranes was compared. Figure 4.10 shows the percent (%) swelling of the multilayers as a function of solution pH (18.5 bilayers) on a planar surface (determined by in-situ ellipsometry; see Section 4.2) and within the pores of TEPC membranes. (For a definition of percent swelling in each geometry, see Appendix A) While the hysteresis is present in both cases, swelling in the confined geometry is clearly suppressed. This suppression of swelling in the confined geometry is believed to be caused by a decrease in the volume available to the multilayers during swelling. In the case of multilayers swelling on a planar substrate, the multilayer-liquid interface is essentially stress free as it undergoes swelling; however, in the case of multilayers in the confined geometry, as the multilayers swell, the volume available to the swelling multilayer decreases leading to stress at the multilayer-liquid interface. Also, another possibility is the contribution of electrostatic repulsive forces that may act across the physical opening hindering the close approach of multilayers as the

pores become smaller. It is expected that the effect of confinement would be more pronounced as the ratio of multilayer thickness to radius of the pores becomes larger.

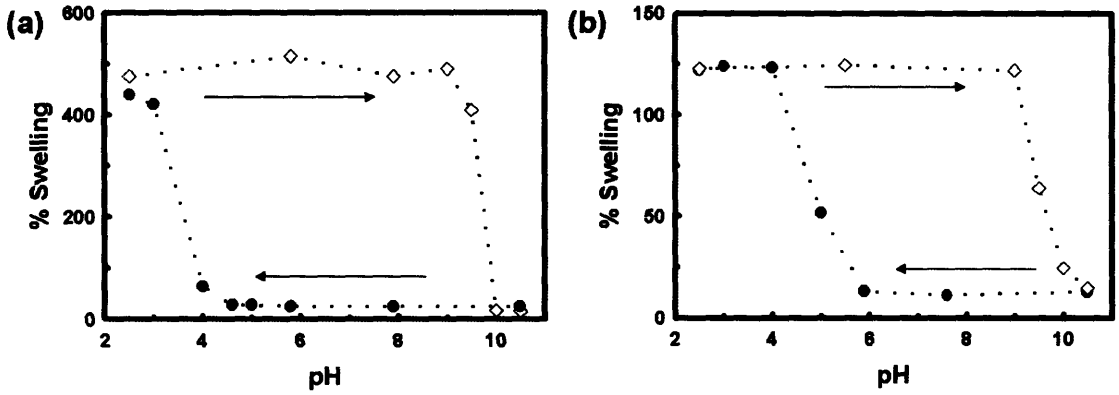

Figure 4.10. Comparison of % swelling (a) on a planar Si substrate (determined by in-situ ellipsometry) and (b) in the cylindrical pores of the 800 nm pore TEPC membranes (from flux measurements and the TRF model). The filled circles, and open diamonds represent data generated after a pH 10.5 pretreatment and after a pH 2.5 pretreatment, respectively.

4.3.3 Reversible gating of membrane pores.

Reversibility of the multilayer gates was verified by changing solution pH between pH 2.5 and pH 10.5 five times (see Section 4.2 for details). Figure 4.11 shows the reversible gating properties of the 400 nm pore TEPC membranes coated with 6.5 bilayers of (PAH/PSS) multilayers. Although a small decrease is seen in the flux of the "open" states as the number of acid/base treatment cycles increased, the multilayer-modified TEPC membranes retains reversibility as the conditions are cycled between the "open" and "closed" states with changes in solution pH. The small decrease in the flux may be attributed to slower deswelling kinetics as the number of cycles increased, possibly due to a reorganization of the polyelectrolyte chains in the multilayer structures. As can be seen in Figure 4.11(b), the degree of swelling of a 6.5 bilayer (PAH/PSS) multilayer in cylindrical pores (determined from flux experiments based on the TRF model and HP equation) was smaller compared to the same

multilayers on planar Si wafers (determined by in-situ ellipsometry). As described above, it is believed that stress in the multilayer due to the decrease in available volume during multilayer expansion is responsible for the suppression of swelling in the confined geometry. Although it cannot be clearly seen in Figure 4.11(b) (due to the large scale in the ordinate), the % swelling of multilayers in the cylindrical pores indeed shows a small increase in the open, or deswollen, (pH 10.5) state with the number of acid/base cycles.

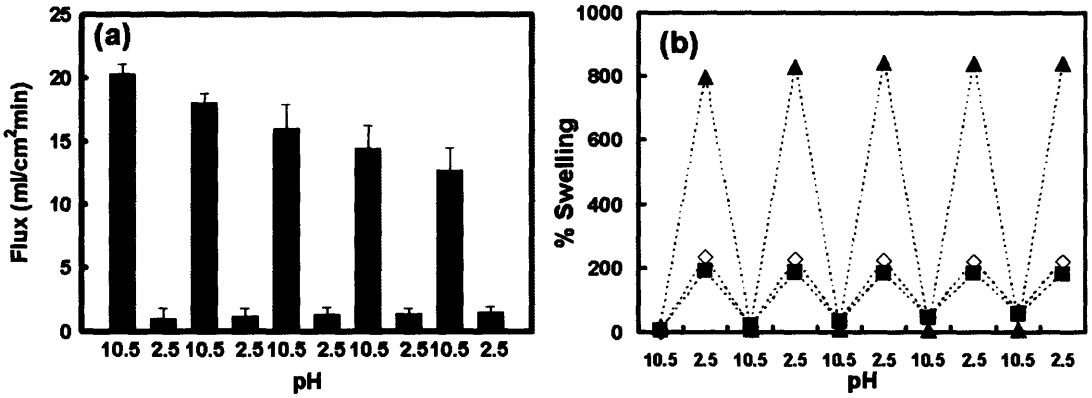

Figure 4.11. Reversible gating of 400 nm pore TEPC membranes with 6.5 bilayers of (PAH/PSS) multilayers. (a) Changes in the trans-membrane flux as a function of pH and (b) % swelling of 6.5 bilayers of (PAH/PSS) multilayers on planar Si substrate (▲) (determined by in-situ ellipsometry), and in the pores of 400 nm pores TEPC membranes based on the HP equation (◇) and the TRF model (■).

4.3.4 In-situ atomic force microscopy (AFM).

In-situ AFM was performed to visualize the gating of the cylindrical pores by the swollen (PAH/PSS) multilayers at acidic conditions (pH 2.5). Figure 4.12 shows the time evolution of pores being closed by the swelling multilayers. Multilayer-modified TEPC membranes show relatively smooth surfaces in a dry state. In the initial stages of the swelling (< 15 min), the pores of the TEPC membranes become smaller and, at the same time, the raised ridges are formed around the pores

(Figure 4.12(b)). These ridges around the pores indicate that the multilayers within the pores are also swelling in the axial direction of the pores and the axial expansion could be accommodating some of the stress that is formed during the swelling in the radial direction. The pores are clearly visible up to 50 min, which indicates that swelling within the pores is suppressed. Swelling studies on planar substrates showed that the multilayers swell ~ 500 % after only 3 min (Figure 4.10 (a))[141]; therefore, the pores should have been closed completely in less than 3 min if the multilayers exhibited the same swelling behavior within the confined geometry. In-situ AFM again supports the idea that the swelling of (PAH/PSS) multilayers is suppressed by the confinement. A direct comparison between the swelling behavior of the multilayers in the pores observed from in-situ AFM and the flux measurements is not made since the experimental conditions such as applied pressure under which each experiment was performed are different.

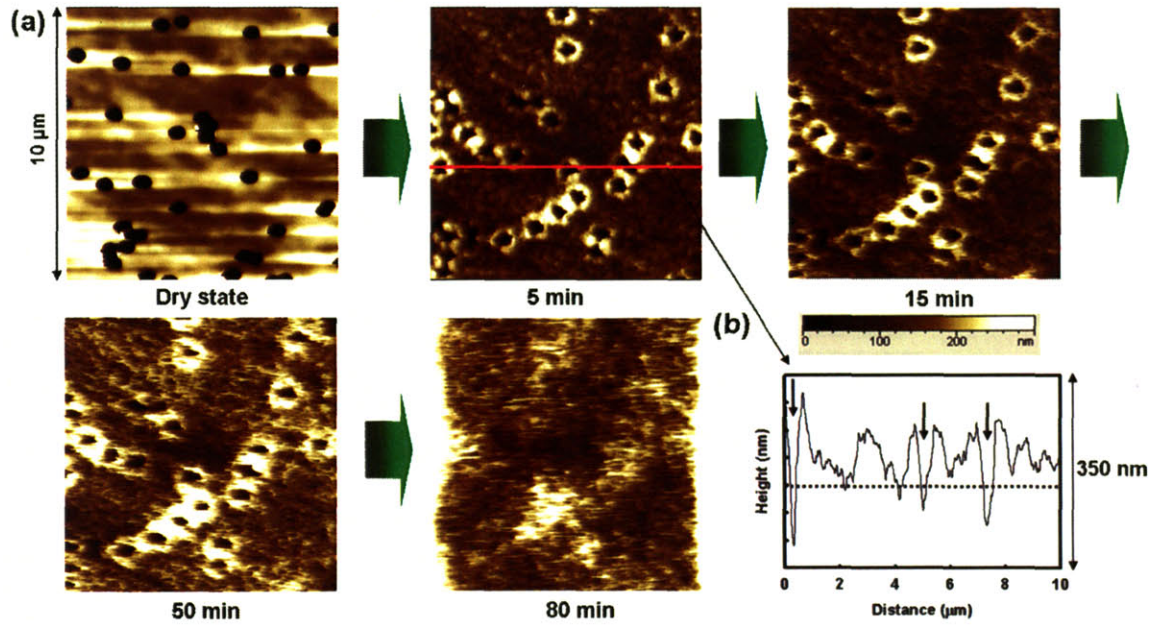

Figure 4.12. (a) Time evolution of the pore structures observed by in-situ AFM of (PAH/PSS) multilayer-modified 800 nm pore TEPC membrane under acidic condition (pH 2.5). (b) Height profile from the "5 min" AFM image along the red line (arrows indicate the locations of pores).

4.3.5 Filtration of macromolecules

To demonstrate that it is possible to have either "open" or "closed" states at one pH condition depending on the pretreatment conditions, a high-molecular weight water soluble polymer, poly(ethylene oxide) (PEO), was filtered using multilayer-modified TEPC membranes. PEO was a suitable candidate for the filtration test since it is water soluble and, at the same time, does not carry any charges; therefore, it is possible to exclude any charge effect during the filtration process. The PEO solution was made with deionized water (pH range between 5.5 and 6.0). Figure 4.13 shows that when the multilayer-modified TEPC membranes were pretreated at pH 10.5, PEO chains could not be retained by the filter, and essentially all of the original concentration (0.01 g/dL) was recovered in the filtrate. After pH 2.5 treatment of the multilayer modified membranes, however, approximately 80 % of the PEO was retained due to size exclusion. It is likely that only relatively short PEO chains passed through the constricted pores of the TEPC membrane resulting in the observed decrease in the total concentration of PEO in the filtrate.

Filtration was also performed by dissolving PEO in pH 2.5 adjusted-water. As shown inFigure 4.13, the PEO solution made with pH 2.5 adjusted-water shows a higher PEO retention. It is believed that the lower filtration efficiency in DI water (pH 5.5 – 6.0) solutions may be due to the relaxation (or deswelling) of the swollen multilayers that occurs when the filtration is performed. A previous report showed that when the (PAH/PSS) multilayer pretreated in acidic condition (pH 2.5) was immersed in DI water for a prolonged period (> 60 min), the multilayer deswells to its original thickness.[141] Multilayers in the cylindrical pores of TEPC membranes deswell much more slowly that planar thin films. A negligible change in the flux was observed (for a membrane pretreated at pH 2.5) with DI water for at least 1 h. The observed slow deswelling kinetics is believed to be a consequence of the geometrical confinement of the multilayers. While the planar thin films are exposed to a semi-infinite reservoir of DI water, the swollen multilayer within the confined geometry

comes in contact with only a small amount of DI water that permeates through the constricted pores. A more extensive study on the swelling/deswelling dynamics of multilayers in confined geometry should be performed in the future. In the case of the acidic PEO solution, the multilayers maintain a high level of swelling during filtration leading to higher filtration efficiency. These results clearly show the feasibility of retaining or passing high molecular weight polymer using the (PAH/PSS) multilayer-modified TEPC membranes at a specific pH condition by varying the pretreatment conditions. In other words, the pretreatment history of the multilayer-modified membranes determines whether high molecular weight polymers can be retained or passed through at a single pH condition.

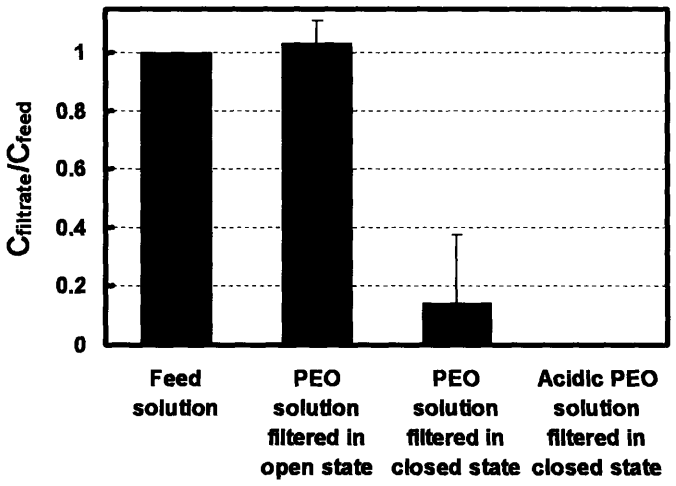

Figure 4.13. Filtration of high molecular weight PEO (0.01 g/dL) using 18.5 bilayer (PAH/PSS) modified 800 nm TEPC membranes in different conditions. Flux during each filtration experiment was ~ 0.01 ml/(cm^2·min). Open and closed states were attained by the pretreatment of multilayer-modified membranes at pH 10.5 and pH 2.5, respectively. PEO was dissolved in DI water to make PEO solution (pH 5.5 – 6.0). Acidic PEO solution was made by adjusting the solution pH of PEO solution to pH 2.5. Error bars represent standard deviation. $C_{filtrate}$ and C_{feed} denote the concentration of PEO in filtrate and feed solutions, respectively.

4.4 Conclusions

This study has demonstrated that stimuli responsive membranes can be fabricated by modifying track-etched polycarbonate membranes with polyelectrolyte multilayers comprising poly(allylamine hydrochloride) and poly(sodium 4-styrenesulfonate). (PAH/PSS) multilayers were deposited on TEPC membranes at a high pH condition (pH > 9.0) which has been shown to produce multilayers that undergo discontinuous swelling/deswelling transitions. Multilayer-modified TEPC membranes showed discontinuous changes in the trans-membrane flux as a function of solution pH. Using two qualitative models, the diameters of the pores were predicted from experimental values of the flux. Compared to the swelling of these multilayers on planar Si substrates, the geometrically confined multilayers swelled to a smaller extent. It is believed that stresses in the multilayers that arise from limitations on the available volume during multilayer swelling suppress the expansion of the multilayers within the confined geometry. Although a small decrease in the trans-membrane flux was observed in the "open" state as the number of open/close cycles was increased, multilayer-modified TEPC membranes showed reversible gating properties during multiple alternate acid and base treatments. As demonstrated in a simple filtration experiment of water soluble PEO, these membranes can either retain or allow the passage of high molecular weight PEO chains at a specified pH condition, depending on the membrane pretreatment condition. By utilizing the overlap of an electrical double layer in the constricted pores, it may be also possible to use these membranes for pH-triggered separation of small molecular weight charged molecules such as charged dye molecules as well as small ionic species.[166-168]} In addition, this new class of stimuli responsive mechanochemical valves can be used to gate the flow of water in microfluidic channels allowing either an open or closed state to exist at a single pH condition.[169]

Chapter 5
Heterostructured Magnetic Nanotubes

5.1 Introduction

Magnetic colloidal particles that have a linear dimension between 1 nm to 1 μm[170] have attracted much attention recently due to their potential applications in various branches of science and engineering.[85] The versatility of magnetic colloidal particles lies in the fact that magnetic forces can be used to direct these particles to separate (or move) molecules and cells *in vitro*. In addition, these particles can be magnetically targeted to specific anatomical sites *in vivo*. Other biomedical applications of colloidal magnetic particles include their use as contrast enhancing agents in magnetic resonance imaging (MRI)[171,172] and also as biosensors[173]. These particles have been also utilized to form permanently or temporarily linked chains of beads[174,175] and ordered patterns on surfaces.[176-179]

A number of different preparation methods have been developed in preparing magnetic colloidal particles that can be dispersed in water. Magnetic nanoparticles have been in situ synthesized in porous polymeric particles to create magnetically responsive polymer microspheres (these particles are commercially available as Dynabeads®).[180] Preformed magnetic nanoparticles have been also embedded in different organic and inorganic matrices such as amphiphilic block copolymers[181,182] and mesoporous silica shells.[183,184] Preformed magnetic nanoparticles have been deposited onto the surfaces of colloidal particles via different approaches to create magnetically responsive core-shell spherical particles or hollow microcapsules.[55,185-189]

While most efforts in the field have been focused on creating spherical magnetic particles, a few studies also have shown promise in creating tubular magnetic structures as alternatives to spherical particles.[190-193] Son *et al.* have shown that silica based magnetic nanotubes can be synthesized by utilizing anodized aluminum oxide (AAO) templates and subsequently used for bioseparation and drug delivery.[191] Martin and co-workers have shown over the past few decades that various types of functional nanotubes can be created based on template synthesis where tubular structures are formed inside the pores of membranes (e.g., AAO and track-etched polycarbonate) and then "freed" by sacrificing the membranes.[194-196] One major advantage of these tubular structures over spherical particles is the possibility of obtaining multifunctional particles by utilizing the presence of inner and outer surfaces.[191,195] As will be described in this chapter, the outer bilayers of nanotubes can be designed to function as compartments for loading and releasing small molecular weight drug molecules and the inner bilayers can be tailored to create magnetic manipulability of the tubes.

As described in Chapter 1, layer-by-layer (LbL) deposition of charged species including synthetic polyelectrolytes, biomacromolecules (e.g., proteins, polysaccharides, DNA etc.), and nanoparticles offers a versatile means to prepare nanocomposite coatings on various types of supports including planar surfaces[17], spherical microparticles[27,197], and porous membranes[28,30,137,198,199]. In addition, as shown in previous chapters, multilayers with various functionalities can be created by incorporating weak polyelectrolytes into these films[44,50,140-142,200]. In addition, heterostructures whose composition or physical properties vary through the thickness of the films can be easily fabricated by using different combinations of polyelectrolytes and nanoparticles during the LbL process.[9,44,201]

Several studies have recently shown that the LbL technique along with the template method can be used to create hollow nanotubes with sub-micron dimensions. It has been shown that by using

track-etched polycarbonate membranes and anodized aluminum oxide membranes, hollow tubes whose aspect ratio is between 25 to 200 can be prepared.[29,32,138,139,202-204] Unlike their inorganic counterparts, these layer-by-layer assembled tubes are often highly flexible and can be further functionalized readily via a number of different surface modification methods. Also, various types of functional multilayer systems that have been developed on planar or spherical supports can be easily assembled into these tubular structures via the template method.

In this Chapter, the formation of magnetic nanotubes[205] via layer-by-layer assembly of polymers and magnetic iron oxide nanoparticles will be investigated. Polyelectrolyte multilayers consisting of poly(styrene sulfonate) and poly(allylamine hydrochloride) are deposited onto track-etched polycarbonate membranes. Subsequently inner surface of the multilayer modified pores of TEPC membranes are further modified with magnetic nanoparticle-containing multilayers. The outer bilayers of the LbL assembled tubes, as demonstrated in Chapter 4, can undergo discontinuous swelling/deswelling transitions as a function of solution pH and can also be activated to absorb a large amount of small molecular weight molecules (e.g., anionic drug and dye molecules) for subsequent release.[50,141] The inner bilayers of the nanotubes contain magnetite nanoparticles to allow magnetic manipulation of these tubes in solution. It will be demonstrated that the template method enables the formation of colloidal multilayer structures with slightly charged weak polyelectrolytes without the problem of irreversible aggregation during the LbL process. As reported in Chapter 1, the LbL assembly of partially ionized weak polyelectrolytes onto spherical colloidal particles often can lead to the undesirable aggregation of the particles[61] or the formation of non-uniform coatings[206] limiting the formation of a stable suspension of functionalized particles. The separation (or removal) and release of small molecular weight anionic molecules by the magnetic nanotubes is also studied. As will be shown, magnetic fields can be used to effectively remove a high

concentration of anionic dyes from a solution. These tubes also can potentially be used as drug delivery vehicles that can be directed to specific locations using magnetic fields.

5.2 Experimental Methods

Materials. Poly(allylamine hydrochloride) (PAH) (M_w = 70 000), poly(sodium 4-styrenesulfonate) (PSS) (M_w = 70 000), $FeCl_2 \cdot 4H_2O$, $FeCl_3$, citric acid monohydrate, ibuprofen (sodium salt), acid red 8, and rose bengal were purchased from Sigma-Aldrich and used as received. Poly(ethylene oxide)-*b*-poly(methacrylic acid) (PEO-PMAA; $Mw \sim 7\,800$-$2\,000$) was purchased from Polymer Sources, Inc. Track-etched polycarbonate membranes (25 mm in diameter) whose pore diameters are 800 nm were purchased from Whatman and Sterlitech.

Preparation of citrate-stabilized magnetic nanoparticles. Citrate-stabilized Fe_3O_4 nanoparticles were synthesized using the method reported by Sahoo et al.[207] Briefly, the mixture of 0.86 g $FeCl_2$ and 1.40 g $FeCl_3$ were mixed in 40 ml water (degassed by bubbling $N_{2(g)}$ prior to mixing) and heated to 80 °C under nitrogen. While vigorously stirring the mixture, 5 ml of NH_4OH was added by syringe and heated for additional 30 min. The supernatant was decanted while the nanoparticles were retained in the reaction flask using a magnet and then fresh water was added. 2 ml citric acid solution (0.5 g/ml) was added and the reaction mixture was heated to 95 °C for 90 min. The reaction mixture was allowed to cool down to room temperature under nitrogen. The nanoparticle suspension was rinsed with deionized (DI) water three times and dialyzed against DI water for 72 h. The magnetic nanoparticles have a zeta-potential of -47.9 ± 3.3 mV at pH 8.5.

Preparation of magnetic hollow tubes. Polyelectrolyte solutions of 10 mM (based on the repeat unit molecular weight) were prepared from DI water (> 18 MΩ·cm Millipore), and the pH of both polyelectrolyte solutions and the rinse water were adjusted to pH 9.3 (unless otherwise noted, all the

(PAH/PSS) multilayers were assembled at pH 9.3 in this study) with 1 M NaOH. Each solution was filtered using 0.45 μm filters. The pH of the assembly solutions was monitored to ensure that a significant drift in pH did not occur during experiments. The drift in pH was typically less than 0.2 units. If the drift exceeded this amount, the solution was replaced with fresh solution. Polyelectrolyte multilayers were assembled onto track-etched polycarbonate (TEPC) membranes at room temperature by using an automated HMS programmable slide stainer (Zeiss, Inc.). Polyelectrolyte multilayers were deposited by dipping into the polycation (PAH) solution and the polyanion (PSS) solution alternately (for 20 min each) with pH-adjusted water rinsing in between (for 2, 2, and 1 min before the next dip into a polyelectrolyte solution). Typically 20.5 bilayers of (PAH9.3/PSS9.3) multilayers were assembled onto the 800 nm pore TEPC membranes. After the assembly of multilayers, multilayers coating the top and bottom surface of the membranes were removed by plasma etching at pressure of 100 mTorr for 4 min. Three to four bilayers of Fe_3O_4 and PAH were deposited onto the membranes after the plasma etching. The TEPC membranes were slowly dissolved in the mixture of dichloromethane and ethanol (9:1) and sonicated for 10 min.[208] After the sonication, the tubes were rinsed in fresh dichloromethane five times followed by two ethanol rinses.

For PEO-PMAA modification, magnetic tubes were first redispersed in DI water after the last ethanol rinse. After 10 min in pH 2.5 water, tubes were redispersed in PEO-PMAA (5 mM based on the PMAA repeat unit) solution for 15 min. After the deposition of the block copolymer, the tubes were rinsed with DI water three times.

Magnetic nanotube characterization. Scanning electron microscopy was performed on a JEOL 6320 scanning electron microscope at an acceleration voltage of 2 kV. Samples were coated with 10 nm of gold/palladium. Transmission electron microscopy was performed on a JEOL 200CX operated at 200 kV. Samples were prepared on either carbon or silica oxide coated copper grids. Zeta

potentials of the samples were measured in DI water using a Brookhaven ZetaPals zeta potential meter. A superconducting quantum interference device (SQUID) magnetometer (Quantum Design Model MPMS) was used for magnetic property characterization of magnetic tubes. The samples (approximately 0.5 to 1 mg) were dried in vacuum overnight and then sealed in a poly(ethylene) straw tube for the measurements. Error in the weight measurement of the samples is approximately 0.1 mg. Magnetization scans were performed between -20,000 and 20,000 Oe (increments of 500 Oe) at 5 and 300 K.

Separation and release of anionic molecules. For separation of rose bengal, 25 μM solutions were made. Magnetic nanotubes either as prepared or acid activated were suspended into the solution which was shaken for 15 min. Lab magnets were used to separate the nanotubes from the solution.

Rose bengal, acid red 8 and ibuprofen were used as model anionic molecules for release studies. Each chemical was dissolved in de-ionized water to make a 1 mM solution and then loaded into acid-activated magnetic nanotubes. Magnetic nanotubes loaded with each molecule were suspended in pH 7.4 phosphate buffered saline (PBS) solution at room temperature. The fraction of molecules released was monitored using UV-Vis spectroscopy. The total amount of each anionic molecule loaded into magnetic nanotubes was determined by releasing the bound molecules in a high pH solution (> pH 11.0).

5.3 Results and Discussion

5.3.1 Formation and characterization of layer-by-layer assembled magnetic nanotubes.

Magnetic nanotubes were assembled using track-etched polycarbonate (TEPC) membranes as templates as illustrated in Figure 5.1. Multilayers comprised of poly(allylamine hydrochloride) (PAH) and poly(styrene sulfonate) (PSS) were assembled onto the TEPC membranes at a high pH

condition (pH 9.3). As described in Chapter 4, these multilayers can undergo a discontinuous swelling/deswelling transition as a function of solution pH and have been shown to have a high capacity for loading low molecular weight anionic molecules after they have been pretreated, or "activated", with acidic solution (pH < 2.5).[50,141] As will be described later, the resultant multilayer nanotubes can potentially be used for separation and delivery of anionic molecules. After the desired number of bilayers (usually 20.5 bilayers; a bilayer consists of a polyanion and polycation) have been deposited ("(PAH *a*/PSS *b*)$_x$" will denote *x* bilayers of (PAH/PSS) multilayers. *a* and *b* will represent the pH condition of PAH and PSS solution, respectively.), the multilayer coatings on the top and bottom surfaces of the membranes were removed by plasma treatment (step (b) in Figure 5.1). Figure 5.2 shows the SEM images of a typical surface of a multilayer-modified TEPC membrane before and after the plasma treatment. It can be clearly seen that the plasma treatment efficiently removes the surface polymer layers, exposing the multilayers that conformally coat the pores of the TEPC membranes. Complete removal of multilayers on each surface of the TEPC membranes was crucial as incomplete removal of the multilayers often led to the formation of bundles of aggregated nanotubes rather than separately suspended tubes after the removal of the TEPC membranes. While others have used different methods[29,32] (e.g., mechanical removal using sand paper), the plasma etching technique was found to be extremely reliable as the thickness of removed films can be precisely controlled by changing processing conditions (time, pressure, and feed gas). A detailed study on the removal of polyelectrolyte multilayers using plasma etching is currently underway. It should be noted that although the complete removal of the multilayers on each surface of the TEPC membranes was essential in obtaining well dispersed tube suspensions after template removal, some bundles of tubes were still obtained due to the existence of some interconnected pores in the TEPC membranes.[209,210] Roughly 10 ~ 20 % of the tubes were in bundles of more than five nanotubes as determined by optical microscopy.

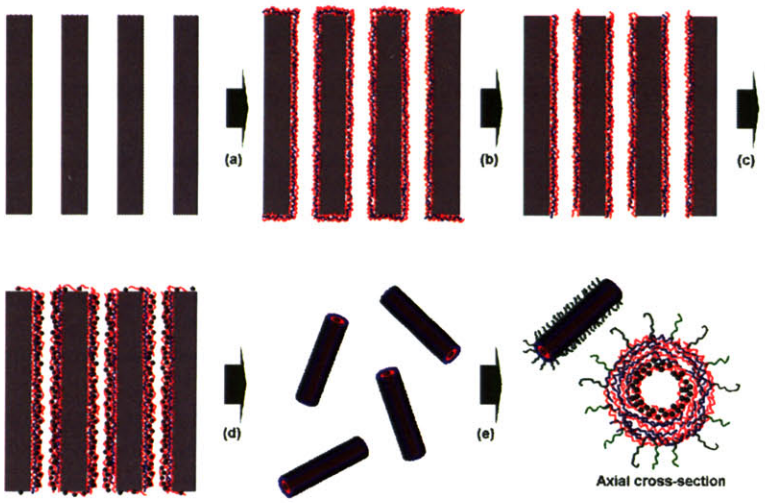

Figure 5.1. Formation of layer-by-layer assembled magnetic hollow tubes via the template method. (a) Assembly of multilayers on track-etched polycarbonate (TEPC) membranes. (b) Plasma etching of each surface of the multilayer-modified TEPC membranes. (c) Adsorption of Fe_3O_4 (magnetite) nanoparticle/PAH multilayers. (d) Dissolution of TEPC membranes. (e) Surface modification of magnetic hollow tubes with a PEO-PMAA block copolymer. An axial cross-section of a typical nanotube is shown in the right lower corner.

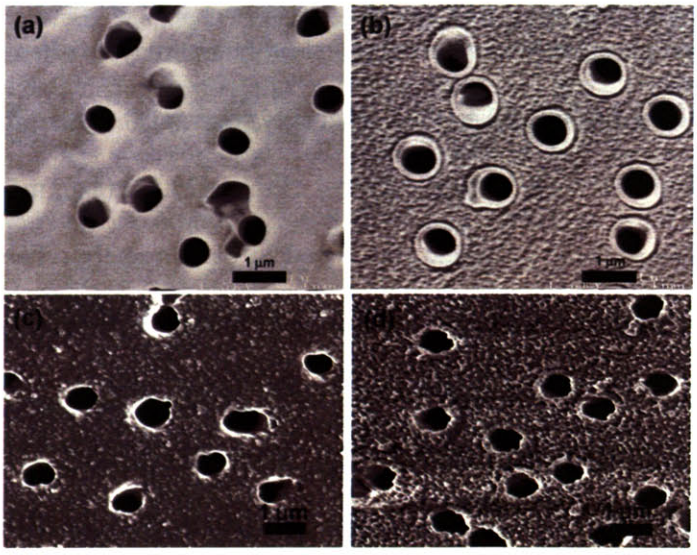

Figure 5.2. SEM images of $(PAH9.3/PSS9.3)_{20.5}$ multilayer-modified membranes (a) before and (b) after plasma etching. SEM images of (c) and (d) were taken after the deposition of $(Fe_3O_49.3/PAH9.3)_4$ multilayers onto untreated and plasma treated $(PAH9.3/PSS9.3)_{20.5}$ modified TEPC membranes, respectively.

The tubes within the pores of the TEPC membranes were further modified by depositing additional layers of citrate-coated Fe_3O_4 nanoparticles (7 ~ 10 nm in diameter) and PAH (step (c) in Figure 5.1). After deposition of three or four bilayers of magnetite nanoparticles and PAH, the resultant magnetic tubes were freed from the templates by dissolving the TEPC membranes. It should be pointed out that the $(PAH9.3/PSS9.3)_{20.5}$ multilayers on both surfaces of the TEPC membranes were more easily removed before rather than after the deposition of magnetite nanoparticles and PAH. A prolonged plasma etching (longer than a few min) to remove the $(PAH9.3/PSS9.3)_{20.5}$ multilayers (if this multilayer was not removed prior to the deposition of the magnetite nanoparticles and PAH) beneath the magnetite nanoparticle/PAH bilayers often led to the damaging (burning) of the TEPC membranes. The difficulty in the removal of the multilayers is likely due to the formation of densely packed magnetite nanoparticles atop $(PAH9.3/PSS9.3)_{20.5}$ multilayers (Figure 5.2(c)). The removal of the multilayers on each surface of the membrane prior to the deposition of magnetic nanoparticles exposed hydrophobic polycarbonate surface[d] which led to the sparse (or incomplete) deposition of magnetite and PAH on each surface of the membrane as seen in Figure 5.2(d). Figure 5.2(d) shows that the tips of the nanotubes are still observed after the deposition of the (Fe_3O_4/PAH) multilayers onto the plasma treated TEPC membranes. Magnetic nanotubes could be easily freed into a stable suspension of tubes with sonication (~ 10 min) during the dissolution of the TEPC membranes. PAH in poorly formed (Fe_3O_4/PAH) multilayers on the top and bottom surfaces (Figure 5.2(d)) of the TEPC membranes could be removed with a short plasma treatment (30 s) but this step was not absolutely necessary to obtain well dispersed nanotubes. Figure 5.3 shows electron microscopy images of nanotubes with or without the magnetic inner shell after they have been freed from the templates. While no clear difference can be seen from the scanning electron microscope (SEM)

---

[d] The surfaces of received TEPC membranes had been modified with poly(vinylpyrrolidone) to increase the hydrophilicity by the supplier.

images (Figure 5.3 (a, c)) before and after the magnetic nanoparticle deposition, transmission electron microscope (TEM) images (Figure 5.3 (b. d)) clearly show the formation of densely packed magnetic bilayers on the inner surface of the nanotubes. By calcinating the magnetic nanotubes, inorganic iron oxide nanotubes could be obtained as shown in Figure 5.4. The obtainment of inorganic nanotubes supports the idea that a densely packed inner shell of magnetic nanoparticles is formed. The above results demonstrate that heterostructured nanotubes can be easily assembled using a combination of the template approach and the LbL technique and that inner and outer bilayers can be designed to have their own functions. In this case, while the inner bilayers will confer magnetic properties to the tubes, the outer bilayers will function as compartments for loading and releasing different anionic molecules. The template method provides a means to create colloidal materials with multilayers incorporating weak polyelectrolytes. As has been reported by others[61], assembly of partially ionized polyelectrolytes (PAH at pH 9.3 in this case) onto spherical colloidal particles will often lead to undesirable aggregation of the particles during the LbL assembly. Non uniform coating of the particles was also seen when PAH and PSS were assembled onto spherical particles at a high pH condition (pH 10).[206] It is expected that a number of interesting multilayer systems that only have been realized on macroscopically planar surfaces can be easily and successfully transferred to a sub-micron scale by the combination of the template method and the LbL assembly of functional multilayers.

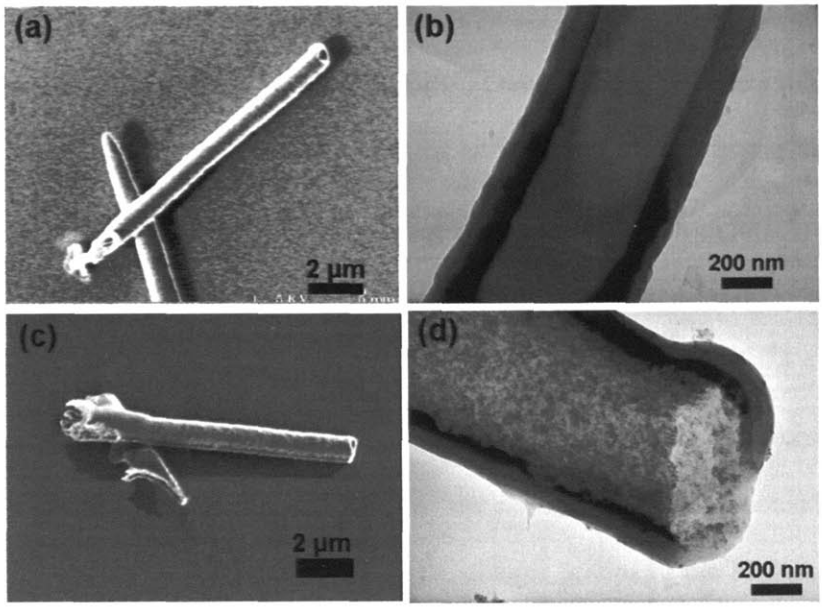

Figure 5.3. SEM and TEM images of hollow tubes (a, b) without and (c, d) with magnetic nanoparticle/PAH multilayers.

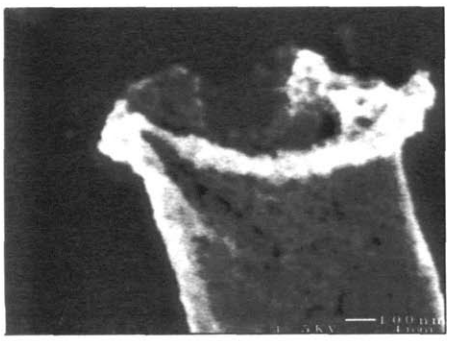

Figure 5.4. SEM image of iron oxide nanotubes after the calcination of layer-by-layer assembled magnetic nanotubes.

The magnetic properties of the nanotubes $((PAH9.3/PSS9.3)_{20.5}(Fe_3O_4 9.3/PAH9.3)_3)$ were characterized by a SQUID magnetometer. Hysteresis loops of samples were measured at 5 and 300 K (Figure 5.5). While the nanotubes exhibited ferromagnetism with a coercivity of ~ 240 Oe at 5K, they showed superparamagnetic characteristics at 300K with a saturation moment of ~ 4 emu/g. Based on the saturation magnetization of the magnetic nanoparticles (~ 19 emu/g) measured using

only the nanoparticles and the data of Figure 5.5, the nanoparticles constitute approximately 20 wt.-% of nanotubes. [e] For various applications in industry and the biomedical arena, the observed superparamagnetic properties are desirable as magnetic forces can be utilized to manipulate these nanotubes. Also the tubes can readily be redispersed in a medium in the absence of a magnetic force.

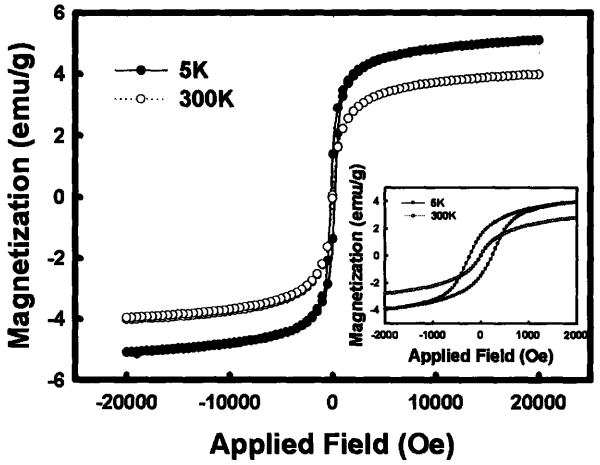

Figure 5.5. Magnetization curves of magnetic nanotubes $((PAH9.3/PSS9.3)_{20.5}(Fe_3O_4/PAH9.3)_3)$. Magnetization vs. Applied field at 5 and 300 K (inset shows high resolution magnetization curve for each temperature).

Tailoring surface properties of colloidal materials is often important as these properties play a crucial role in determining colloidal stability as well as the suitability of use in biomedical applications. In this respect, the addition of poly(ethylene oxide) (PEO) chains onto surfaces of colloidal particles has many advantages. PEO, or poly(ethylene glycol) (PEG), has been utilized in various biomedical applications as it has been shown to increase the circulation half life *in vivo* by

---

[e] Thermal gravimetric analysis (TGA) of the magnetic nanotubes with four bilayers of PAH and magnetite nanoparticles (i.e., $(PAH9.3/PSS9.3)_{20.5}(Fe_3O_49.3/PAH9.3)_4$) showed that magnetite nanoparticles consititute ca. 30 wt. % of the nanotubes. Note that the magnetization characterization in Figure 5.5 was performed with magnetic nanotubes composed of three bilayers of PAH and magnetite nanoparticles (i.e., $(PAH9.3/PSS9.3)_{20.5}(Fe_3O_49.3/PAH9.3)_3$).

making colloidal objects less recognizable to phagocytes.[172,211,212] Also it has been used to increase the stability of colloidal particles in high salt concentration buffer solutions due to a steric stabilization mechanism.[213]

The surfaces of the freed nanotubes were further modified (or "PEGylated") by adsorbing a block copolymer (poly(ethylene oxide)-b-poly(methacrylic acid) (PEO-PMAA)) (step (e) in Figure 5.1). The zeta potential of the tubes changed from + 50.3 ± 1.2 mV to – 25.4 ± 1.5 mV (measured in DI water) confirming the adsorption of the block copolymer onto the surfaces of the magnetic nanotubes. The charge reversal (as indicated by the change in the zeta potential) is due to the overcompensation of positive surface charges by the anionic groups of the PMAA block. A similar change in the zeta potential was observed by others when a block copolymer containing PEO and an anionic block was adsorbed onto poly(ethyleneimine) (PEI) modified maghemite nanoparticles.[172] The magnetic nanotubes showed markedly improved colloidal stability in salt solution (0.1 M NaCl) after PEO-PMAA surface modification. The improved colloidal stability can potentially enable the utilization of these nanotubes in physiologically relevant environments as will be demonstrated later.

5.3.2 Separation of anionic molecules using the magnetic nanotubes.

As briefly mentioned above, when PAH/PSS multilayers assembled at a high pH condition (pH > 9.0) are treated with acid (< pH 2.5), the multilayers' capacity to bind anionic dye molecules (i.e., rose bengal) dramatically increases approximately by an order of a magnitude.[50] The increased capacity arises from the ionization of free amine groups within the multilayers. Rapid diffusion of the dye molecules through the swollen network of polyelectrolytes also plays a role in the observed large uptake over experimentally accessible timescales. Taking advantage of the increased capacity for the uptake of anionic molecules after acid treatment, the magnetic nanotubes (unless otherwise noted, magnetic nanotubes from this point will refer to nanotubes with the following structure:

$(PAH9.3/PSS9.3)_{20.5}(Fe_3O_4 9.3/PAH9.3)_4$ modified with PEO-PMAA block copolymer) could successfully be used to separate or remove a high concentration (25 μM) of anionic molecules from solution. As seen in Figure 5.6, when the as-assembled nanotubes without the acid activation (right) are used to separate the anionic dye molecules, there is no noticeable change in the color of the solution compared to the original solution (25 μM rose bengal solution: middle) after the nanotubes have been collected using a magnetic field. However, after the nanotubes have been acid activated, they can effectively absorb a large amount of rose bengal molecules and remove essentially all of the rose bengal molecules from the solution upon application of a magnetic field. The efficient removal of rose bengal from the solution using the nanotubes clearly indicates that the functionality observed in planar films is retained in tubular structures even after several additional preparation steps (nanoparticle deposition, plasma etching, TEPC membrane dissolution). The large and rapid anionic molecule uptake of the magnetic nanotubes after acid activation also provides indirect evidence that the nanotubes undergo the same swelling transition observed in planar films. These results show that the LbL assembled magnetic nanotubes can be utilized as separation tools in various fields. The removal of dyes and toxins from solution is especially important in industrial practice, since incomplete removal of these molecules in effluent streams can lead to unwanted circumstances such as pollution of the environment.[214]

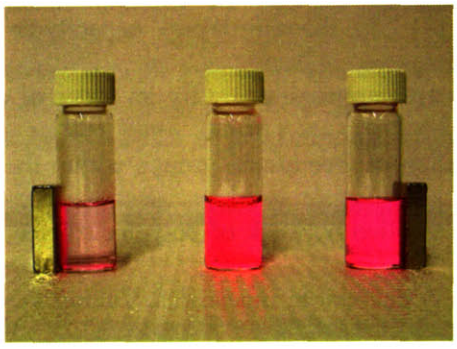

Figure 5.6. Photo image showing the separation (removal) of rose bengal molecules from aqueous solution (25 μM) by using magnetic hollow tubes. From left to right: solution after the removal with

tubes activated with acid, original solution and solution after the treatment with as-prepared (without the acid activation) tubes.

5.3.3 Release of anionic molecules in physiological buffer solution.

As these magnetic nanotubes can be easily manipulated using magnetic fields, they can be used as drug carriers targeted to specific anatomical sites *in vivo* and also can be used in applications where sustained release of chemical agents at specific locations is necessary.[215] Three anionic molecules (i.e., ibuprofen, acid red 8, and rose bengal) that are used as pharmaceuticals or bear resemblance to many drug molecules, were used in the release study. For example, ibuprofen is a well known anti-inflammatory drug[216], and rose bengal has been studied as an anti-viral agent.[217,218] Each anionic molecule was loaded into the magnetic tubes from 1 mM solutions after acid activation. Figure 5.7 shows the release profile of each molecule from the multilayer tubes in pH 7.4 phosphate buffered saline (PBS) solution. The molecular structure of the anionic molecules has a strong effect on the release behavior. While the bulky rose bengal is released extremely slowly, virtually all of the loaded ibuprofen is instantaneously released. Slow release of rose bengal from planar multilayers was also observed in a previous study.[50] Acid red 8, which is smaller than rose bengal and larger than ibuprofen in volume by ~ 100 $Å^3$ (molecular volume of each molecule was estimated using Chem3D Pro (CambridgeSoft)), shows an intermediate release behavior. The rapid release of ibuprofen molecules from the multilayers can be attributed to the charge screening between the carboxylate groups of ibuprofen and amine groups of PAH in the high ionic strength buffer solution and also to the fast diffusion of small ibuprofen molecules in the swollen multilayers. A similar result has previously been observed for the release of charged dye molecules (methylene blue) from planar polyelectrolyte multilayers comprised of PAH and poly(acrylic acid) (PAA) in PBS buffer solution.[200] The sustained release of rose bengal and acid red 8 compared to the rapid release of ibuprofen, on the other hand, is likely due to the slow diffusion of these molecules in the multilayer

matrix caused by steric hindrance. The release profile of each molecule from $(PAH9.3/PSS9.3)_{20.5}$ multilayers assembled on planar substrates was also studied and exhibited the same trend; that is, while rose bengal released extremely slowly, ibuprofen molecules released rapidly.

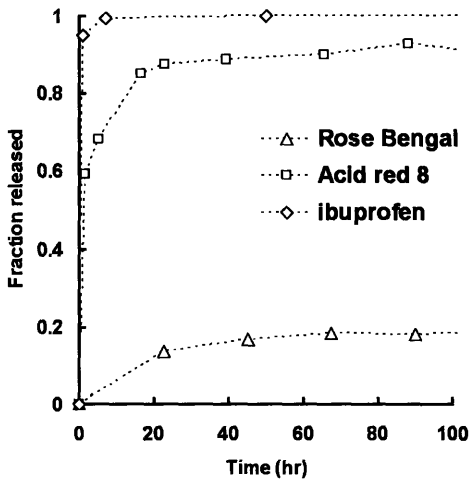

Figure 5.7. Release profiles of anionic molecules from magnetic nanotubes in pH 7.4 phosphate buffered saline (PBS) solution.

5.4 Conclusions

Layer-by-layer assembly of polymers and nanoparticles was utilized with the template method to create magnetic nanotubes with sub-micron dimension. After the deposition of polyelectrolyte multilayers comprised of poly(allylamine hydrochloride) (PAH) and poly(styrene sulfonate) (PSS), multilayers on the flat surfaces of the membranes were removed with plasma treatment. Subsequently thin layers of magnetite nanoparticles and PAH were adsorbed onto the inner surface of the tubes followed by template (TEPC membrane) dissolution. Electron microscopy confirmed that magnetic nanoparticles were successfully adsorbed onto the inner surfaces of the tubes. These tubes exhibited superparamagnetic properties at room temperature. The magnetic nanotubes could be utilized to remove a large amount of an anionic dye (i.e., rose bengal) from solution after acid

activation. A release study of the anionic molecules indicates that the diffusion of the molecules in the multilayers is greatly influenced by their size. Larger molecules were released slowly while the smallest molecule (ibuprofen) released rapidly from the multilayers. As these tubes can be easily manipulated and directed to specific locations using magnetic forces, they can be used as separators and also as carriers of drugs or agents to targeted sites *in vivo* as well as *in vitro*.

In this report, the formation of magnetic nanotubes and their separation and release properties of low molecular weight anionic molecules were studied. However, the multilayer investigated in this report is known to undergo a large discontinuous swelling/deswelling transition (as much as ~ 600% of their original volume) as a function of solution pH. The fast uptake of anionic molecules upon acid activation as demonstrated above provides an indirect evidence of such swelling transition occurring in these nanotubes. In addition, preliminary results based on dynamic light scattering indicate that the multilayer tubes also swell in the acidic condition. Also results in Chapter 4 showed that the (PAH9.3/PSS9.3) multilayers assembled within the pores of TEPC membranes undergo a discontinuous swelling/deswelling transition.[30] However, the mode of swelling of freely suspended multilayer nanotubes, that is how much swelling takes place in the radial and axial direction, still remains unclear. To date, all of the swelling studies of multilayers, whether assembled on planar or spherical supports, have observed swelling only in the direction of the assembly (i.e., perpendicular to the substrate for planar and radial direction for spherical supports). I recommend investigating the swelling behavior of these tubes using various techniques such as *in situ* atomic force microscopy, confocal laser scanning microscopy, light scattering, and rheometry.

Chapter 6
All-Nanoparticle Thin Film Coatings

6.1 Introduction

The assembly of nanoparticles into conformal and uniform thin films with precise control over chemical and physical properties poses a significant challenge. A number of techniques has been developed and studied over the years to create robust thin films of nanoparticles that can lead to novel applications in the areas of photonics, catalysis, sensors and biomaterials.[219] Some examples of these approaches include the electrodeposition of semiconductor and metal nanoparticles[220,221], the deposition of nanoparticle monolayers via the Langmuir-Blodgett technique[222,223], sol-gel chemistry based deposition of nanoparticles[224] and in situ synthesis of nanoparticles using polymeric thin films as templates[225,226]. While these methods provide a means to create thin films of nanoparticles on surfaces, incorporating two or more nanoparticles into conformal thin films that can be readily coated onto different types of surfaces and geometries is still an unsolved problem.

In 1966, a seminal paper by Iler disclosed a novel method to create multilayers of inorganic "colloidal particles" without the use of any organic molecules by a method now known as layer-by-layer (LbL) deposition.[18] He reported that multilayers of oppositely charged nanoparticles can be assembled by the sequential adsorption of oppositely charged nanoparticles onto substrates from aqueous suspensions. Although Iler's work did not attract attention at the time, it was one of the first studies to successfully demonstrate that thin films of nanoparticles can be readily assembled. Twenty five years after Iler's discovery, Decher and co-workers utilized LbL processing to fabricate multilayer thin films from oppositely charged polyelectrolytes.[17,60] Decher's pioneering work has

led to a very large number of studies that have shown potential applications of LbL assembled films in various fields.[17] The LbL technique has been extended to the preparation of conformal thin films containing nanoparticles paired with polyelectrolytes[22,52-54,227-232] with precise control over film properties. Despite Iler's disclosure 40 years ago and the enormous attention the LbL technique has received over the past 15 years, multilayer thin films containing oppositely charged nanoparticles without any polyelectrolytes have not been heavily explored.[233,234]

In this chapter, the possibility of creating all-nanoparticle thin film coatings by the method described by Iler is re-examined. It is demonstrated that all-nanoparticle-based coatings comprising oppositely charged nanoparticles can be created using the aqueous based LbL technique.[18] As a model system, positively charged TiO_2 nanoparticles and negatively charged SiO_2 nanoparticles were used to create the all-nanoparticle multilayer coatings. To characterize the multilayers consisting of TiO_2 and SiO_2 nanoparticles, a characterization technique based on ellipsometry was developed, which allows the determination of the porosity and chemical composition of these all-nanoparticle multilayer thin films without the need for any assumption about the refractive indices of the constituent nanoparticles. As Iler noted in his work, multilayers comprising oppositely charged nanoparticles are porous in nature due to the presence of interstitial void volume.[18] The presence of nanopores in the TiO_2/SiO_2 nanoparticle-based multilayer coatings leads to useful functionalities including antireflection and antifogging properties. In addition, the presence of TiO_2 nanoparticles leads to self-cleaning properties, making them extremely attractive for applications in photovoltaic cells, automobile windshields and windows of high rise buildings. The aqueous-based LbL assembly of oppositely charged nanoparticles provides a versatile and general approach in creating all-nanoparticle based conformal thin film coatings on various substrates. It also represents a general means to create multifunctional coatings by incorporating different types of nanoparticles that exhibit catalytic, magnetic, optical and metallic properties.

6.2 Experimental Methods

Materials. Anatase titanium oxide nanoparticles STS-100 (18 wt. % TiO_2 suspension in water, average particle size of 7 nm, and specific surface area of 320 m^2/g) were generously provided by Ishihara Sangyo Kaisha, Ltd (Japan). Silica nanoparticles, Ludox SM-30 (30 wt. % SiO_2 suspension in water, average particle size of 7 nm, and specific surface area of 345 m^2/g), and Ludox TM-40 (40 wt. % SiO_2 suspension in water, average particle size of 22 nm, and specific surface area of 140 m^2/g) were purchased from Sigma-Aldrich (St. Louis, MO). The average size of nanoparticles was provided by the suppliers. Glass slides were purchased from VWR International. The zeta-potential of each nanoparticle at pH 3.0 was measured using a ZetaPals (Brookhaven Instrument Corp.).

Fabrication of TiO_2/SiO_2 nanoparticle-based multilayer coatings. Sequential adsorption of TiO_2 and SiO_2 nanoparticles onto glass substrates was performed by using an automated dipping machine. The concentration and solution pH of each nanoparticle suspension were adjusted to 0.03 wt. % and pH 3.0 (using 1.0 M HCl), respectively. Glass substrates were degreased with detergent and then cleaned with 1.0 M NaOH solutions under sonication for 15 min. Deionized water (> 18 MΩ·m, Millipore Milli-Q (MQ)) was used to make the nanoparticle suspensions. The dipping time in each nanoparticle solution was 10 min followed by three rinse steps (2, 1, and 1 min) in deionized water. A Barnstead Thermolyne 47900 furnace was used to calcinate the films at 550 °C for 3 h.

Characterization. Thicknesses of the TiO_2/SiO_2 nanoparticle-based multilayers assembled on glass substrates were determined by using a Woolham Co. VASE spectroscopic ellipsometer; the data analysis was done using the WVASE32 software package. An uncoated glass slide was first scanned in the ellipsometer. Measurements were performed from 300 to 900 nm at an angle of incidence of 70°. The data obtained were fitted to a Cauchy model which assumes that the real part of the refractive index (n_f) can be described by:

$$n_f(\lambda) = A_n + \frac{B_n}{\lambda^2} + \frac{C_n}{\lambda^4} \qquad (6.1)$$

where, A_n, B_n and C_n are constants, and λ is the wavelength of the light. The values of refractive index reported in this study were determined at 633 nm. As the difference in the refractive indices of the porous films and the glass substrates was significant (typically larger than 0.2), the measurements of thickness and refractive index of the films were possible using the ellipsometer. Nolte et al. have previously reported the successful use of ellipsometry to measure the thickness of polymeric multilayers on transparent rubbery substrates made of poly(dimethylsiloxane).[154] In that case, the mismatch in the refractive index between the substrates and the films was less than 0.2. Film thickness of the multilayers was also measured using a Tencor P10 surface profilometer. Differences in the thicknesses measured using the two methods (ellipsometry and profilometry) were less than 10 %.

Root-mean-squared (RMS) surface roughness of the multilayers was determined by using a Nanoscope IIIa in a Dimension 3000 AFM microscope (Digital Instruments, Santa Barbara, CA) in the tapping mode in the air. RMS roughness was obtained from AFM images with a scan size of 10 × 10 μm^2. Transmission measurements were performed using a Varian Cary 6000 spectrophotometer. Sessile drop contact angle measurements utilizing deionized water were performed with a VCA-2000 contact angle system (AST Products, Inc., MA). A water drop of approximately 0.5 μL was placed on the multilayer coated surfaces using a syringe. Advancing contact angle values were determined from dynamic video files that captured at 15.6 frames/s using the software provided (VCA Optima XE Version 1.90) by the manufacturer.

Determination of chemical composition of TiO_2/SiO_2 nanoparticle multilayer thin films via quartz crystal microbalance (QCM) and X-ray photoelectron spectroscopy (XPS). To monitor the mass uptake during the layer-by-layer assembly, quartz crystal microbalance (QCM) crystals with

gold electrodes were used. The gold electrodes were cleaned with hot water and ethanol and dried with N_2 gas. The gold electrode was then treated with 16-mercaptodecanoic acid before the LbL assembly was performed. A mass control QCM system20 comprised of a HP 53131A/ 225 MHz universal counter and computer was connected to an automated dipper. The frequency shift caused by material adsorption onto the QCM crystal was monitored every second by a computer. The weight fraction (w_{TiO_2}) of TiO_2 nanoparticles was estimated from the following relation on the assumption that the frequency shift (|Δf|) is proportional to the mass increase at each adsorption step:

$$w_{TiO_2} = \left| \frac{\Delta f_{TiO_2}}{\Delta f_{TiO_2} + \Delta f_{SiO_2}} \right| \qquad (6.2)$$

The weight fractions of TiO_2 nanoparticles were measured and averaged over at least 6 bilayers of deposition for each TiO_2 and SiO_2 nanoparticle multilayer system. Due to the presence of nanopores which would be filled with water during the QCM measurements, the interpretation of QCM data (i.e., the assumption on the relation between the mass uptake and the frequency shift), however, is not straightforward.

The mass fraction of the TiO_2/SiO_2 nanoparticle based multilayers was also measured using X-ray photoelectron spectroscopy (XPS). A Kratos AXIS Ultra Imaging XPS with an Al Kα source was used at normal angle of detection relative to the surface plane. As this characterization technique probes the chemical composition of surface (to depths of less than 10 nm) rather than the bulk film, multilayers with TiO_2 or SiO_2 nanoparticles as outermost layer were fabricated for XPS measurements. For multilayers comprising 7 nm TiO_2 and 22 nm SiO_2 nanoparticles, 6 and 6.5 bilayer samples were analyzed. For multilayers comprising 7 nm TiO_2 and 7 nm SiO_2 nanoparticles, 12 and 12.5 bilayer samples were analyzed. Half a bilayer represents a multilayer with a TiO_2 nanoparticle layer as the outermost layer. While it is difficult to estimate the chemical composition of

the bulk films from these data, the two values obtained with TiO_2 and SiO_2 nanoparticles as outermost layers for each system provides a plausible range (as presented in Table 6.2) for the chemical composition of the entire films.

Photocatalytic Activities of TiO_2/SiO_2 nanoparticle-based Multilayers. Methylene blue (MB) was used as the model contaminant. Multilayer coated glass substrates were contaminated by immersing them into a 30 μM MB solution for 5 min. Contaminated samples were irradiated with ultraviolet light (UVM-57, UVP) centered at 302 nm with an intensity of 1.5 mW/cm^2. The amount of MB remaining in the multilayer coatings was monitored by measuring the UV-Vis spectra and comparing the absorbance measured at 660 nm. The contact angles after UV irradiation of MB contaminated samples were measured without rinsing the samples.

6.3 Results and Discussion

6.3.1 Fabrication and Characterization of All-Nanoparticle Thin Film Coatings.

Layer-by-layer assembly of positively charged TiO_2 nanoparticles (average size ~ 7 nm) and negatively charged SiO_2 nanoparticles (average size ~ 7 and ~ 22 nm) was performed using glass or silicon as substrates. The concentration and pH of each nanoparticle suspension was adjusted to 0.03 wt. % and 3.0, respectively. The growth behavior of multilayers comprising TiO_2 and SiO_2 nanoparticles was monitored using spectroscopic ellipsometry and atomic force microscopy (AFM). Figure 6.1 (a) shows the variation of film thickness with increasing number of deposited bilayers (one bilayer consists of a sequential pair of TiO_2 and SiO_2 nanoparticle depositions). In both cases, the multilayers show linear growth behavior (average bilayer thickness for 7 nm TiO_2/22 nm SiO_2 and 7 nm TiO_2/7 nm SiO_2 multilayers is 19.6 and 10.5 nm, respectively). The RMS surface roughness, determined via AFM, increases to an asymptotic value for each system. Other studies, in which

nanoparticle thin films were assembled using polyelectrolytes, DNA or di-thiol compounds as linkers between nanoparticles also showed linear growth behavior.[52,53,59,235,236] However, in a recent molecular dynamics (MD) simulation study of layer-by-layer assembled multilayers comprising two oppositely charged nanoparticles, the thickness of the multilayers exhibited non-linear growth behavior due to the increase in the surface roughness of the multilayers.[237] The increased surface roughness was a result of substrates not being uniformly coated with the nanoparticles as the number of deposited layers increased. Therefore, the observed saturation of surface roughness in this study indirectly indicates that the surface is uniformly and completely coated with the nanoparticle multilayers. AFM results confirmed the existence of a uniform coating of multilayers on glass substrates.

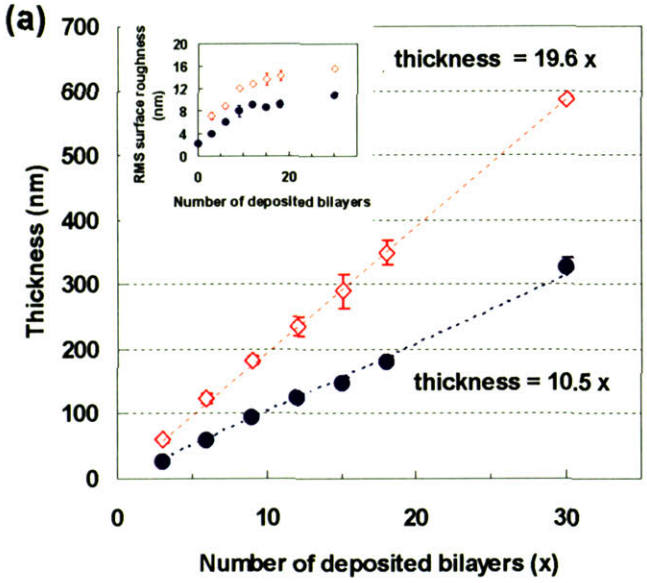

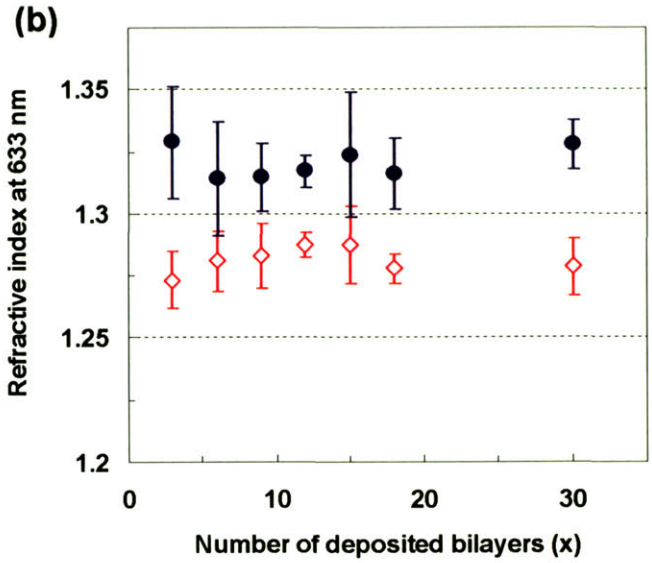

Figure 6.1. (a) Thickness and (b) refractive index of (7 nm TiO_2/7 or 22 nm SiO_2) multilayers assembled on glass substrates as determined by ellipsometry. Inset in Figure (a) represents the root-mean-squared (RMS) surface roughness of the multilayers as determined with AFM. Open diamonds and closed circles represent multilayers comprising 7 nm TiO_2/22 nm SiO_2 and 7 nm TiO_2/7nm SiO2 nanoparticles, respectively.

While the refractive index of each system does not change as a function of the number of deposited bilayers, the refractive indices of the two systems differ. Figure 6.1 (b) shows that multilayers comprising 7 nm TiO_2 and 22 nm SiO_2 nanoparticles have an average refractive index of 1.28 ± 0.01, whereas multilayers made from 7 nm TiO_2 and 7 nm SiO_2 nanoparticles have an average refractive index of 1.32 ± 0.01. In both cases, the refractive index of the TiO_2/SiO_2 nanoparticle multilayer is lower than the reported values of bulk anatase TiO_2 (2.0 ~ 2.7)[238-240] and SiO_2 (1.4 ~ 1.5)[241]. As described by Iler, the assembly of nanoparticles results in the presence of nanopores which will effectively lower the refractive index of the multilayers.[18] The invariance of the refractive index with thickness and the linear growth behavior indicate that the composition of the multilayers for each system does not vary with increasing number of deposited bilayers. The

difference in the observed refractive index of the two multilayer systems suggests that either the porosity, the relative amount of TiO_2 to SiO_2 nanoparticles, or both differ. To clearly address this issue, the porosity and chemical composition of the nanoparticle multilayer coatings were determined via ellipsometry.

6.3.2 Determination of porosity and refractive index of the nanoparticle framework of thin films using ellipsometry.

Ellipsometry has been widely used to estimate the porosity of thin films based on the assumption that the refractive index of the constituent materials is known.[59,242] When the constituent materials are nanoparticles, however, it is not always possible to have reliable information on the refractive index of the nanoparticles utilized to fabricate the film. The physical properties of nanoparticles differ from the bulk properties of their corresponding materials due to quantum confinement effects and their large specific surface areas.[243,244] A method based on ellipsometry was developed to determine the porosity of nanoporous thin films without any assumption about the material properties (i.e., refractive index). For porous thin films, if the refractive index of the material's framework (i.e., solid materials) and the overall porosity are unknown, the solving of two independent equations containing the two parameters would be necessary to determine these values. These two independent equations can be obtained by measuring the values of the effective refractive index of the porous thin films in two different media of known refractive index (e.g., air and water), assuming that the thickness of the porous thin films remain constant in these two different media (constant volume). Another prerequisite for this method to work is that the pores should be interconnected so that the chosen media can infiltrate and fill the pores completely. Based on the arguments above, the porosity and the refractive index of the film's solid framework can be derived according to the procedure described below.

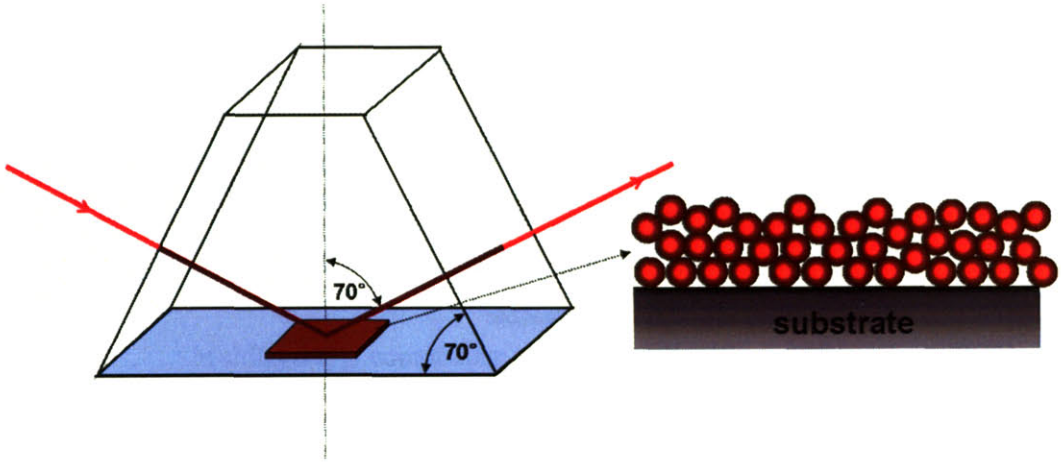

Figure 6.2. Measurement of thickness and refractive index of all-nanoparticle thin films in medium 1 (i.e., air).

Step 1. The effective refractive index ($n_{f,1}$) of the nanoporous thin film is measured in air ($n_{f,air}$ = 1.00) inside an ellipsometric cell made of quartz (Hellma) as shown in Figure 6.2. $n_{f,1}$ can be represented using a first principle mixing rule for the effective refractive index as: $n_{f,1} = p \cdot n_{f,air} + (1-p) \cdot n_{f,framework}$. Thickness of multilayer thin films in the dry state was measured inside as well as outside the quartz cell. The difference between the two measurements was negligible (typically less than 0.5 nm) indicating that the use of the quartz cell does not alter the measurements. Previous studies have shown that these types of cells can be used reliably to measure the thicknesses of thin films in various solvents.[30,141,155]

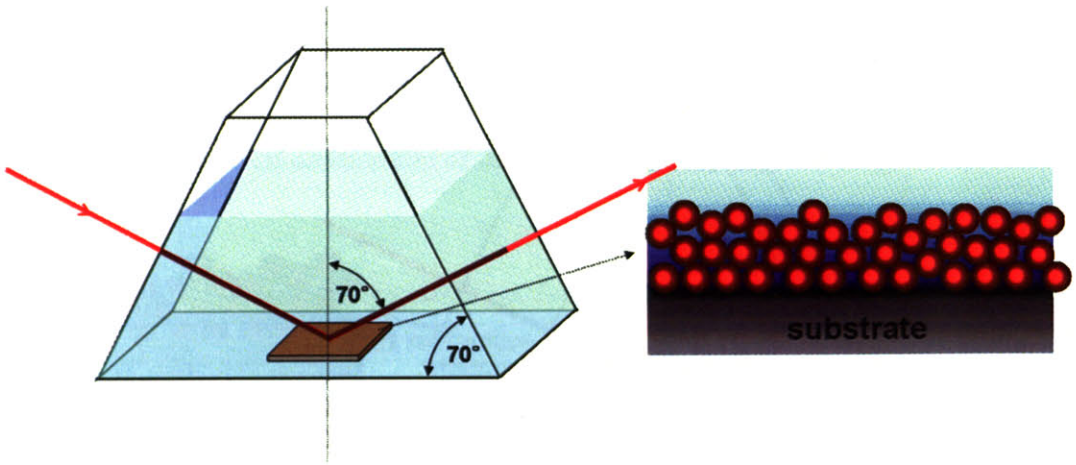

Figure 6.3. Measurement of thickness and refractive index of an all-nanoparticle thin film in medium 2 (i.e., water).

Step 2. The effective refractive index ($n_{f,2}$) of the nanoporous thin films is measured in water (n_{water} = 1.33) on the same spot where the previous measurement in air was made as shown in Figure 6.3. $n_{f,2}$ can be represented using the first principle mixing rule for the effective refractive index as: $n_{f,2} = p \cdot n_{f,water} + (1-p) \cdot n_{f,framework}$.

Step 3. After confirming that the values of thickness from steps 1 and 2 do not differ (difference was typically less than 2 nm), the porosity (p) and the refractive index of the nanoparticle framework ($n_{f,framework}$) was calculated using the two equations above. These values can be expressed as:

$$p = \frac{n_{f,2} - n_{f,1}}{n_{f,water} - n_{f,air}} = \frac{n_{f,2} - n_{f,1}}{0.33} \tag{6.3}$$

$$n_{f,framework} = \frac{n_{f,1} - n_{f,air} \cdot p}{1 - p} \tag{6.4}$$

Step 4. In the case of the all-nanoparticle thin films made from TiO_2 and SiO_2, four independent variables need to be determined for quantitative characterization of the films. These variables are

porosity (p), the volume fraction of either of the nanoparticles (e.g., v_{TiO_2}), and the refractive indices of TiO_2 (n_{f,TiO_2}) and SiO_2 (n_{f,SiO_2}) nanoparticles. The refractive index of each nanoparticle (n_{f,TiO_2} and n_{f,SiO_2}) was first obtained by the method described above; that is, effective refractive indices of nanoporous thin films comprising either TiO_2 or SiO_2 nanoparticles were measured in air and in water, and then equations (6.3) and (6.4) were used to calculate the refractive index of each constituent nanoparticle. Multilayers comprising TiO_2/poly(vinyl sulfonate) (PVS) and poly(diallyldimethylammonium chloride) (PDAC)/SiO_2 were assembled on Si substrates and then calcinated at 550 °C for 3 h to create nanoporous films of TiO_2 and SiO_2 nanoparticles, respectively. The calcination process removes the organic polymers and also fuses the nanoparticles together; therefore, the nanoparticle thin films do not undergo swelling in water. The solution pH of the TiO2 nanoparticles, PVS, SiO_2 nanoparticles, and PDAC solutions for LbL assembly was adjusted to 2.0, 4.0, 9.0, and 4.0, respectively, using 1.0 M HCl or 1.0 M NaOH solution. The concentration of polymer solutions and nanoparticle suspensions was adjusted to 10 mM (based on repeat unit) and 0.03 wt. %, respectively. Figure 6.4, for example, shows the changes in the thickness and refractive index of calcinated (PDAC/7 nm SiO_2 nanoparticle) multilayers as a function of the number of deposited bilayers. The thickness of calcinated (PDAC/7 nm SiO_2) multilayers in air and water does not differ significantly. On the other hand, the refractive index of the films increases in water as the air in the pores of the films is replaced by water which has the higher refractive index. By plugging in the values of refractive index of the calcinated films into Equations (6.3) and (6.4), the porosity of the calcinated films and the refractive index of 7 nm SiO_2 nanoparticles (n_{f,SiO_2}) could be calculated. Following this procedure, the refractive index of each nanoparticle was determined. The refractive index of 7 nm TiO_2, 22 nm SiO_2 and 7 nm SiO_2 nanoparticles was determined to be 2.21 ± 0.05, 1.47

± 0.01 and 1.47 ± 0.004, respectively. These values are in good agreement with the values of refractive index reported for bulk materials, i.e., anatase TiO_2 = 2.0 ~ 2.7 and SiO_2 = 1.4 ~ 1.5.

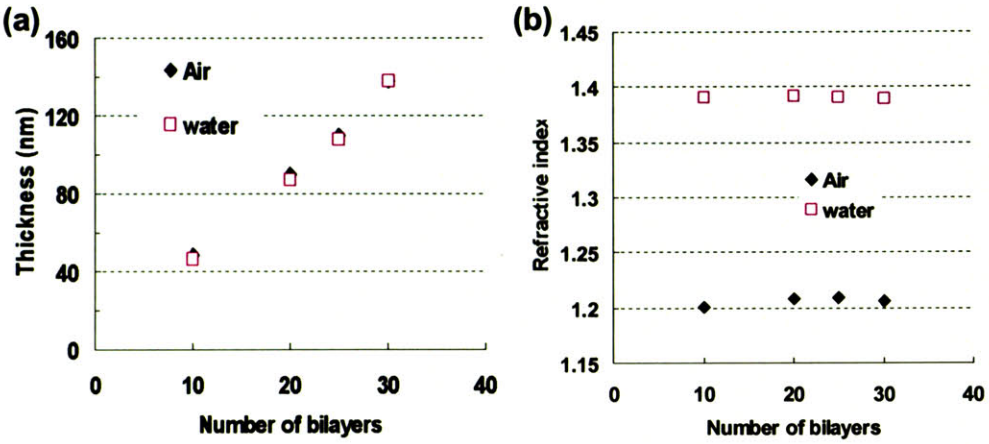

Figure 6.4. (a) Thickness and (b) refractive index of calcinated (PDAC/7 nm SiO_2) multilayers as a function of deposited bilayers measured in air and in water via ellipsometry.

The porosity (p) and the composite refractive index ($n_{f,framework}$; the term "composite" is used as the material's framework in this case since it consists of TiO_2 and SiO_2 nanoparticles) of the nanoparticle framework ($n_{f,framework}$) of the TiO_2/SiO_2 nanoparticle-based thin films were then determined by measuring the effective refractive index of these films in air and in water and using equations 6.3 and 6.4. Using the values obtained for n_{f,TiO_2}, n_{f,SiO_2}, $n_{f,framework}$ and p, the volume fraction of TiO_2 and SiO_2 nanoparticles can be calculated using the linear relation for composite refractive indices and is expressed as follows (The first principle mixing rule for a composite refractive index was used to calculate the volume fraction of TiO_2 (v_{TiO_2}) and SiO_2 nanoparticles (v_{SiO_2}) in the TiO_2/SiO_2 nanoparticle-based multilayers):

$$v_{TiO_2} = \frac{n_{f,framework} - n_{f,SiO_2}}{n_{f,TiO_2} - n_{f,SiO_2}} \cdot (1 - p) \qquad (6.5)$$

$$v_{SiO_2} = 1 - (p + v_{TiO_2}) \qquad (6.6)$$

The simplest form of effective medium formulas was used to calculate the effective refractive index of porous thin films as the goal in this study was to demonstrate the validity of this method based on ellipsometry. The method described above, however, can readily be extended to other effective medium theories including Looyenga, Maxwell-Garnett, and Bruggemann equations.[245]

Table 6.1. Porosity and chemical composition of calcinated TiO_2/SiO_2 multilayers as determined by in-situ ellipsometric method.

Multilayers	Number of bilayers	Composition vol. % (wt. %)		
		Air	TiO_2[a]	SiO_2[b]
(7 nm TiO_2/22 nm SiO_2)	6	44.7 (0)	1.2 (6.3)	54.1 (93.7)
	6.5	45.3 (0)	1.6 (8.0)	53.1 (92.0)
(7 nm TiO_2/ 7 nm SiO_2)	12	35.4 (0)	1.6 (7.3)	63.0 (92.7)
	12.5	35.8 (0)	1.7 (8.0)	62.5 (92.0)

[a] Density of TiO_2 = 3.9 g/cm^3,[246] [b] Density of 22 nm and 7 nm SiO_2 = 1.3 and 1.22 g/cm^3 (provided by the supplier), respectively.

The values obtained are summarized in Table 6.1. The major difference between the 7 nm TiO_2/22 nm SiO_2 and 7 nm TiO_2/7 nm SiO_2 nanoparticle-based multilayer coatings is the porosity, consistent with a denser packing of nanoparticles in films with 7 nm TiO_2 and 7 nm SiO_2 nanoparticles compared to films with the 22 nm SiO_2 nanoparticles. The weight fraction of TiO_2 nanoparticles in the two systems does not differ significantly, although the 7 nm TiO_2/7 nm SiO_2 system has a slightly larger value. Table 6.1 also shows that the ellipsometry method is sensitive

enough to distinguish the slight difference in chemical composition of multilayers with a half bilayer difference (e.g., between 6 and 6.5 bilayers of 7 nm TiO_2 and 22 nm SiO_2 multilayers).

To confirm the reliability of the chemical composition determined via ellipsometry, the weight fractions of TiO_2 and SiO_2 nanoparticles were determined independently using a quartz crystal microbalance (QCM) and X-ray photoelectron spectroscopy (XPS). Table 6.2 summarizes the chemical composition (wt. % of TiO_2 nanoparticles) determined via QCM and XPS (see Section 6.2 for the detailed experimental procedure/scheme used for the determination of the weight fraction of TiO_2 nanoparticles via each technique). The weight fractions of TiO_2 obtained from QCM and XPS consistently indicates that the amount of TiO_2 nanoparticles in the multilayers is relatively small (< 12 wt. %) and that the 7 nm TiO_2/7 nm SiO_2 multilayers have a slightly larger amount of TiO_2 nanoparticles present in the films. These results are consistent with the results obtained from ellipsometry which showed that the weight fraction of TiO_2 nanoparticles in both systems is relatively small compared to that of the SiO_2 nanoparticles and that the 7 nm TiO_2/7 nm SiO_2 system has a higher content of TiO_2 nanoparticles. The fact that the values obtained from three different techniques show good agreement validates the capability of the ellipsometry method.

Table 6.2. Weight percentage (wt. %) of TiO_2 nanoparticles in TiO_2/SiO_2 nanoparticle thin films as determined by QCM and XPS.

Multilayers	QCM	XPS[a]
(7 nm TiO_2/22 nm SiO_2)	8.1 ± 2.3	2.9 ~ 6.6
(7 nm TiO_2/7 nm SiO_2)	11.6 ± 1.7	5.8 ~ 10.9

[a] The lower and upper limit of the values for TiO_2 wt. % were obtained by analyzing the multilayers with SiO_2 and TiO_2 nanoparticles as the outermost layer, respectively.

The observation that the volume fraction of TiO_2 nanoparticles in the two multilayer systems studied is below 2 vol. % (less than 8 wt. %) is remarkable and surprising. I believe the surface charge density of each nanoparticle during the LbL assembly plays an important role in determining the chemical composition of the TiO_2/SiO_2 nanoparticle-based multilayer thin films. At the assembly condition, which is pH 3.0 for both nanoparticle suspensions, the zeta-potential of the 7 nm TiO_2 nanoparticles is + 40.9 ± 0.9 mV, compared to values of - 3.3 ± 2.6 and -13.4 ± 1.4 mV, for the 7 nm and 22 nm SiO_2 nanoparticles respectively. These values suggest that the TiO_2 nanoparticles are much more highly charged than the SiO_2 nanoparticles during the LbL assembly. Therefore, only a small number of TiO_2 nanoparticles would be required to achieve the charge reversal required for multilayer growth. Also the interparticle distance between adsorbed TiO_2 nanoparticles would be large due to strong electrostatic repulsion between the particles. On the other hand, a large number of SiO_2 nanoparticles would be needed to reverse the surface charge and, at the same time, SiO_2 nanoparticles can pack more densely compared to TiO_2 nanoparticles as the electrostatic repulsion between the SiO_2 nanoparticles is not as significant as that between highly charged TiO_2 nanoparticles. On a similar note, Lvov et al. have also shown that the partial neutralization of functional groups on SiO_2 nanoparticles by addition of salt to a nanoparticle suspension leads to an increased fraction of SiO_2 nanoparticles in multilayers assembled with a polycation.[53] The next Chapter will focus on studying the effect of assembly conditions (pH and ionic strength of the nanoparticle suspensions) on the growth behavior as well as the porosity and the chemical composition of the TiO_2/SiO_2 nanoparticle-based multilayers.

6.3.3 Multifunctionality of TiO_2/SiO_2 nanoparticle-based coatings.

The all-nanoparticle thin film coatings based on TiO_2 and SiO_2 exhibited potentially useful functionalities including antireflection, antifogging and self-cleaning properties. Depositing the

nanoporous TiO_2/SiO_2 nanoparticle-based coatings on glass causes the reflective losses in the visible region to be significantly reduced, and transmission levels above 99 % can be readily achieved. The wavelength of maximum suppression of reflections in the visible region is determined by the quarter-wave optical thickness of the coatings, which can be varied by changing the number of layers deposited as seen in Figure 6.5 (a). Figure 6.5 (b) reveals the visual impact of these all-nanoparticle antireflection coatings. Due to its higher effective refractive index, the antireflection properties of a multilayer coating made from 7 nm TiO_2 and 7 nm SiO_2 nanoparticles are not as pronounced (ca. 98 and 97 % maximum transmission in the visible region before and after calcination, respectively) as the 7 nm TiO_2 and 22 nm SiO_2 nanoparticle-based multilayer coatings. The wavelength of maximum suppression of the 7 nm TiO_2/7 nm SiO_2 nanoparticle system, however, can be tuned more precisely compared to the 7 nm TiO_2/22 nm SiO_2 multilayers as the average bilayer thickness is only 10 nm.

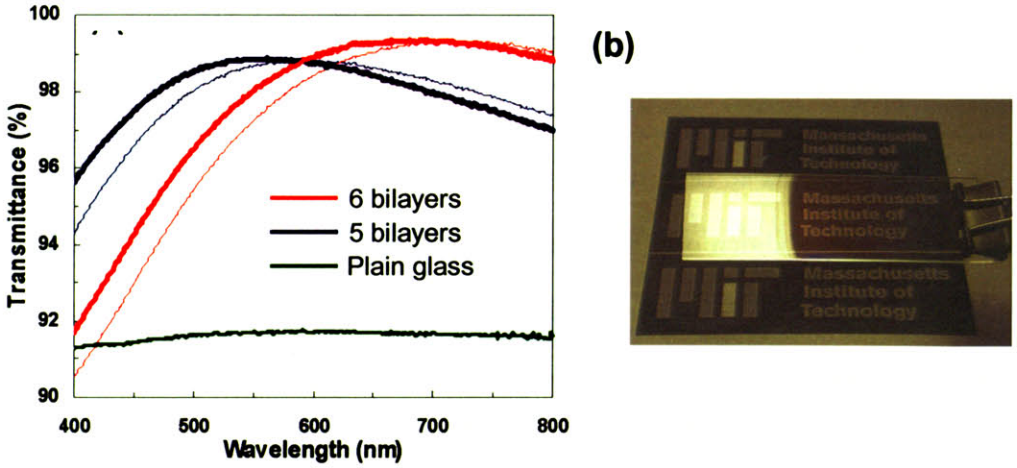

Figure 6.5. (a) Transmittance spectra of 7 nm TiO_2/22 nm SiO_2 multilayer coatings before (thin solid line) and after calcination (thick solid line) on glass substrates. Green, Red and Blue curves represent transmittance through untreated glass and glass coated with 5- and 6 bilayers, respectively. (b) A photograph image of a glass slide showing the suppression of reflection by a 5 bilayer 7 nm TiO_2/22 nm SiO_2 nanoparticle multilayer (calcinated). Left portion has not been coated with the multilayers. Multilayer coatings are on both sides of the glass substrates.

For practical application of any coating, the mechanical integrity (durability and adhesion) is extremely important. Due to the absence of any interpenetrating components (i.e., charged macromolecules) that bridge or glue the deposited particles together within the multilayers, as-assembled TiO_2/SiO_2 nanoparticle-based multilayers show rather poor mechanical properties. The mechanical properties of the all-nanoparticle multilayers can be improved significantly by calcinating the as-assembled multilayers at a high temperature (550 °C) for 3 h, which leads to the partial fusing of the nanoparticles and better adhesion of the coatings to glass substrates.[59] While the film thickness decreases by ca. 5 %, the refractive index increases slightly (ca. 2 %) after the calcination process, resulting in the observed blue shift in the maximum transmission wavelength as seen in Figure 6.5. From this point on, the multifunctional properties of calcinated (7 nm TiO_2/22 nm SiO_2) multilayers will be reported.

In addition to antireflection properties, the nanoporosity of TiO_2/SiO_2 nanoparticle multilayers leads to superhydrophilicity. Cebeci et al. demonstrated that nanoporous coatings comprising SiO_2 nanoparticles exhibit superhydrophilicity (water droplet contact angle < 5° in less than 0.5 sec) due to the nanowicking of water into the network of capillaries present in the coatings.[59] The mechanism of such behavior can be understood from the simple relation derived by Wenzel and co-workers. It is well established that the apparent contact angle of a liquid on a surface depends on the roughness of the surface according to the following relation[247]:

$$\cos\theta_a = r\cos\theta \qquad (6.7)$$

where θ_a is the apparent water contact angle on a rough surface and θ is the intrinsic contact angle as measured on a smooth surface. r is the surface roughness defined as the ratio of the actual surface area over the project surface area. r becomes infinite for porous materials meaning that the surface will be completely wetted (i.e., $\theta_a \sim 0$) with any liquid that has a contact angle (as measured on a

smooth surface) of less than 90°. The contact angle of water on a planar SiO_2 and TiO_2 surface is reported to be approximately 20°[59] and 50 ~ 70°[248,249], respectively; therefore, multilayers comprising SiO_2 nanoparticles (majority component) and TiO_2 nanoparticles (minority component) with nanoporous structures should exhibit superhydrophilicity. Figure 6.6 (a) and (b) verify this expectation; the data show that the contact angle of a water droplet (~ 0.5 μl) on TiO_2/SiO_2 nanoparticle-based multilayer coatings becomes less than 5° in less than 0.5 sec.

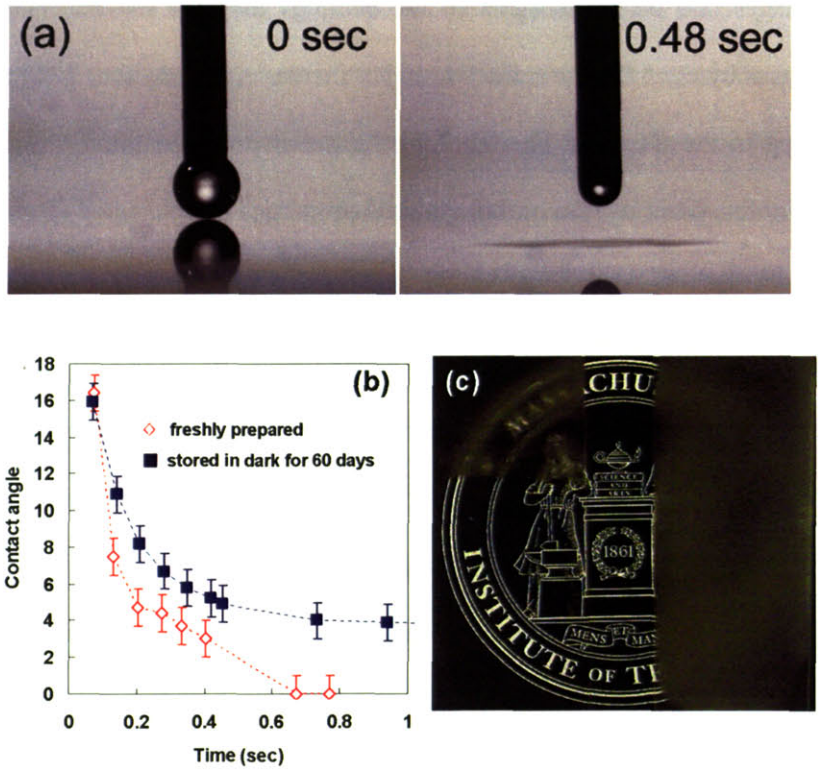

Figure 6.6. Results demonstrating the superhydrophilicity of (7 nm TiO_2/22 nm SiO_2)$_6$ coated glass (after calcination). (a) Images of a water droplet instantaneously (< 0.5 sec) wetting the multilayer-coated glass, (b) changes in the contact angle of a water droplet on the freshly prepared (◊) and 60 day-stored (■) multilayer-coated glass as a function of time and (c) image demonstrating the antifogging properties of multilayer coated glass (left) compared to that of an untreated glass substrate (right). Each sample was exposed to air (relative humidity ~ 50 %) after being cooled in a

refrigerator (below - 4 °C) for 12 h. Top portion of the slide on the left has not been coated with the multilayer, thus it fogs and scatters light.

Unlike TiO_2 based coatings which lose their superhydrophilic properties in the dark, SiO_2/TiO_2 nanoparticle-based coatings retained their superhydrophilicity even after being stored in the dark for at least 60 days (Figure 6.6(b)). Superhydrophilicity leads to antifogging properties which is extremely useful for various applications. The scattering of light caused by condensed water droplets is eliminated due to instant sheet-like wetting of water on the multilayer-modified surface. The antifogging properties of these coatings were demonstrated by exposing untreated and multilayer-modified glass substrates to humid environments (relative humidity ~ 50 %) after cooling them at a low temperature (below - 4 °C) as shown in Figure 6.6(c). As described above, the presence of nanopores in these films leads to nanowicking of water into the network of capillaries in the coatings; therefore, the superhydrophilicity of these coatings can be retained even in the absence of UV irradiation.

While the antifogging properties of superhydrophilic coatings can be extremely useful for a number of applications, contamination of the coating by organic compounds can lead to the loss of this useful property. In this respect, self-cleaning properties of antifogging coatings are very desirable for applications where long-term stability of superhydrophilicity is important. The self-cleaning properties of TiO_2/SiO_2 nanoparticle-based multilayers were tested to confirm that the removal of organic contaminants can be effected by the presence of TiO_2 nanoparticles under UV irradiation[250-252]. Glass substrates coated with TiO_2/SiO_2 nanoparticle-based multilayers were contaminated using a model contaminant, i.e., methylene blue (MB). Nanoparticle-based superhydrophilic coatings[59] containing only SiO_2 nanoparticles were also generated and subjected to the same experiments for comparison. The decomposition of methylene blue by the coatings was monitored by measuring the amount of remaining MB in the coatings after UV irradiation as a

function of time. Figure 6.7 clearly shows that nearly 90 % of the MB in the TiO_2/SiO_2 nanoparticle-based coatings is decomposed after 2 h of UV irradiation whereas less than 50 % of the MB is eliminated from the SiO_2 nanoparticle based coating even after 4 h of UV irradiation.

The contact angle of water on the MB contaminated TiO_2/SiO_2 surface was 18.5 ± 1.0°; thus, the antifogging properties were lost. The contact angle changed to ~ 0° after 2 h of UV irradiation indicating that the superhydrophilicity was recovered. These results demonstrate that the amount of TiO_2 nanoparticles in the multilayer coatings (slightly more than 6 wt. %) is sufficient to confer self-cleaning properties to these coatings. Nakajima et al. also have shown that transparent superhydrophobic coatings containing only 2 wt. % TiO_2 can self-clean under the action of UV irradiation.[251] The recovered antifogging property was retained for more than 30 days even after storing the MB-contaminated/UV illuminated samples in the dark. The contact angle measured on the UV irradiated samples after 30 days of storage in the dark was less than 4°, which is below the limit at which antifogging properties are observed (~ 7°).[59] Some previous studies have shown that the incorporation of SiO_2 into TiO_2 based thin films improves the stability of light-induced superhydrophilicity; however, the mechanism behind the improved stability was different from the current mechanism, which is driven by the nanoporosity.[250,253] While the current system contains TiO_2 nanoparticles that require UV irradiation (wavelengths shorter than 400 nm) for activation, TiO_2 nanoparticles that are sensitive to visible light have been developed.[254,255] Incorporation of these visible light active TiO_2 nanoparticles into the multilayer coatings should be straightforward using the LbL technique and enable self-cleaning properties of the coatings in the visible region.

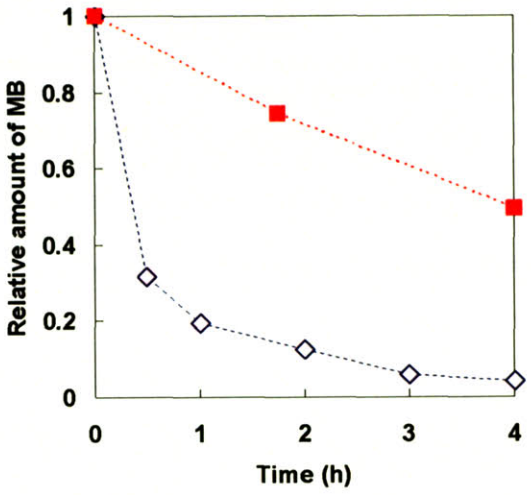

Figure 6.7. Comparison of the photocatalytic properties of SiO_2/TiO_2 (◊) and SiO_2 nanoparticle-based superhydrophilic coatings (■). (a) Self-cleaning properties of multilayers as determined by the relative amount of methylene blue remaining after UV-irradiation. The error in each data point was less than 5 %.

6.4 Conclusions

In summary, it was demonstrated that all-nanoparticle conformal thin film coatings can be generated via aqueous-based layer-by-layer processing. The LbL assembly of oppositely charged nanoparticles, which was first disclosed in 1966[18], has been more or less neglected for the last four decades. The methodology, in principle, provides a versatile means to create all-nanoparticle coatings from different combinations of functional nanoparticles (e.g., catalytic, magnetic and semiconductor nanoparticles). In the present work, I have shown that TiO_2/SiO_2 nanoparticle coatings exhibit attractive and potentially useful antifogging, antireflection, and self-cleaning functionalities.

A technique based on ellipsometry introduced in this work enabled the quantitative characterization of the chemical composition and the porosity of the all-nanoparticle multilayer

coatings without the need for assuming the refractive indices of the constituent nanoparticles. This technique will, in turn, enable the reverse engineering of the all-nanoparticle multilayer coatings by allowing the determination of the effects of porosity and chemical composition on the functionality of interest. The influence of assembly conditions on the growth behavior, chemical composition, and porosity of the nanoparticle/nanoparticle multilayers will be described in the next two Chapters.

Chapter 7
pH-Dependent Structure and Properties of TiO_2/SiO_2 Nanoparticle Multilayer Thin Films

7.1 Introduction

The formation of thin films containing nanoparticles can lead to novel applications in the areas of photonics, catalysis, electronics, magnetism and biomedical engineering.[219] Despite the recent advances in creating various types of functional nanoparticles[244,256,257], it still remains a challenge to create conformal thin films of nanoparticles with precise control over the physicochemical properties. One approach that has been widely used is the layer-by-layer (LbL) deposition[17] of charged nanoparticles in conjunction with an oppositely charged polyelectrolyte.[52-54,57,59,188,227,228,232,258] Properties of nanoparticle-containing multilayers can be precisely tuned by controlling the assembly conditions (e.g., salt concentration and pH conditions), and the types of nanoparticles and polyelectrolytes assembled. Nanoparticle-containing multilayers have been studied extensively for their potential use in the various fields of science[17] and, recently, have shown promise in creating thin films with extreme wetting behaviors.[58,59,201] Also these nanoparticle-containing multilayers can be readily coated onto non-planar geometries such as spherical colloidal particles and porous membranes.[27,30,55,152,188]

While researchers in this field have generally shown that multilayer thin films consisting of nanoparticles and oppositely charged polyelectrolytes can be readily prepared, only a few studies have shown that multilayers of oppositely charged nanoparticles can be created via layer-by-layer assembly.[233,234] It is interesting to note, however, that the very first report of the preparation of multilayers involved the layer-by-layer (LbL) deposition of oppositely charged nanoparticles without

any organic processing agents.[18] This pioneering work did not receive substantial follow-up attention owing to the fact that robust assembly conditions were not easily achieved for the commonly available nanoparticle systems. Thus, researchers turned their attention to the more readily processed polyelectrolyte containing multilayer systems.[17]

In Chapter 6, the possibility of using the LbL technique in the absence of any polymer components was re-examined, and it was demonstrated that all-nanoparticle thin film coatings comprising positively charged TiO_2 nanoparticles and negatively charged SiO_2 nanoparticles can be readily assembled.[259] These all-nanoparticle multilayer coatings exhibited potentially useful antifogging, antireflection and self-cleaning properties. The ability to tune various film characteristics, such as chemical composition, would enable the fabrication of functional coatings for specific applications. For example, others have shown that the amount of TiO_2 nanoparticles in various nanocomposite thin films is crucial in determining the their photocatalytic or superhydrophilic properties.[251,253] In this respect, a comprehensive understanding of the effect of assembly conditions on the chemical composition would provide an important blueprint for the fabrication of functional thin films with desirable properties.

Iler in his seminal report describing multilayers of oppositely charged colloidal particles noted that "adsorption of colloidal silica onto positively charged alumina-coated glass substrates was most rapid and complete in the low pH range of 2 to 4".[18] Although a quantitative study on the effect of assembly conditions (i.e., pH of each nanoparticle suspension) was not performed at the time, he clearly noticed that the pH of colloidal particle suspensions had an enormous influence on the deposition characteristics of multilayers. In this chapter, the dependence of average incremental bilayer thickness, refractive index, chemical composition and porosity of all-nanoparticle multilayer thin films comprising TiO_2 and SiO_2 nanoparticles on the pH of the nanoparticle suspensions will be investigated. By independently changing the pH of each nanoparticle suspension, the average bilayer

thickness[f] of all-nanoparticle thin films could be varied between a few nanometers to tens of nanometers. It will be also demonstrated that the chemical composition as well as the porosity of the all-nanoparticle thin films are dependent on the assembly conditions. Zeta-potential measurements of polystyrene microspheres coated with TiO_2 and SiO_2 nanoparticles show that conditions that enable complete charge reversal after the deposition of each nanoparticle layer are essential to create thick all-nanoparticle multilayers. Incomplete charge reversal leads to sparse nanoparticle adsorption at each deposition step resulting in a relatively small incremental thickness per bilayer.

7.2 Experimental Methods

Materials. Anatase titanium oxide nanoparticles STS-100 (18 wt. % TiO_2 suspension in water, average particle size 7 nm, and specific surface area 320 m^2/g) were generously provided by Ishihara Sangyo Kaisha, Ltd (Japan). Silica nanoparticles, Ludox TM-40 (40 wt. % SiO_2 suspension in water, average particle size 22 nm, and specific surface area 140 m^2/g) were purchased from Sigma-Aldrich (St. Louis, MO). The average size of nanoparticles was provided by the suppliers. Glass slides were purchased from VWR International. 1.5 μm poly(styrene) (PS) microspheres were purchased from Polysciences, Inc.

Assembly of TiO_2/SiO_2 nanoparticle multilayers. Sequential adsorption of TiO_2 and SiO_2 nanoparticles onto glass substrates was performed by using an automated dipping machine. The concentration of each nanoparticle suspension was adjusted to 0.03 wt. %. The pH of each nanoparticle suspension was adjusted using 1.0 M HCl or NaOH. Glass substrates were degreased with 2 vol. % detergent solution and then cleaned with 1.0 M NaOH solutions under sonication for 15

---

[f] The term "average bilayer thickness" is used to represent the incremental thickness measured via ellipsometry after an alternate exposure of substrates to positively charged SiO_2 and negatively charged SiO_2 nanoparticle suspensions. The term "bilayer" in this sense does not necessarily indicate that one dense layer of SiO_2 nanoparticles is formed on top of previsouly adsorbed layer of SiO_2 nanoparticles.

min. Deionized water (> 18 MΩ·m, Millipore Milli-Q (MQ)) was used to make the nanoparticle suspensions. The dipping time in each nanoparticle solution was 10 min followed by three rinse steps (2, 1, and 1 min) in deionized water. The pH of the nanoparticle suspensions was readjusted after deposition of every three bilayers corresponding to approximately 1.5 h. A Barnstead Thermolyne 47900 furnace was used to calcinate the films at 550 °C for 2 h.

Characterization. Thicknesses of the TiO_2/SiO_2 nanoparticle-based multilayers assembled on glass substrates were determined by using a Woolham Co. VASE spectroscopic ellipsometer; the data analysis was done using the WVASE32 software package. An uncoated glass slide was first scanned in the ellipsometer. Measurements were performed from 300 to 900 nm at an angle of incidence of 70 °. The data obtained were fitted to a Cauchy model which assumes that the real part of the refractive index (n_f) can be described by:

$$n_f(\lambda) = A_n + \frac{B_n}{\lambda^2} + \frac{C_n}{\lambda^4} \qquad (7.1)$$

where, A_n, B_n and C_n are constants, and λ is the wavelength of the light. The values of refractive index reported in this study were determined at 633 nm.

The zeta-potential and hydrodynamic diameter of the each nanoparticle (or aggregates of nanoparticles) as a function of pH were determined using a ZetaPals (Brookhaven Instrument Corp.) and a 90Plus Particle Size Analyzer (Brookhaven Instrument Corp.), respectively. Measurements were made within one hour of pH adjustments.

For measurement of zeta-potential after each deposition step, TiO_2/SiO_2 multilayers were assembled onto polystyrene (PS) microspheres whose diameter was 1.5 μm. To facilitate the adsorption of nanoparticles, PS microspheres were primed with five bilayers of poly(allylamine hydrochloride) (PAH) and poly(styrene sulfonate) (PSS) (pH of each polyelectrolyte solution was ~ 4,

and 0.1 M NaCl was added to each solution) prior to the deposition of TiO_2/SiO_2 nanoparticle multilayers. The zeta-potential of the coated microspheres after each adsorption step was measured in pH adjusted de-ionized water. To create hollow microcapsules of TiO_2 and SiO_2 nanoparticles, PS microspheres coated with 5 bilayers of TiO_2 and SiO_2 nanoparticles were calcinated at 550 °C for 2 h. These calcinated hollow microcapsules were observed with a JEOL 6320FV Field-Emission High-Resolution Scanning Electron Microscope (SEM) at an acceleration voltage of 2 kV. The samples were coated with 10 nm of Au/Pd prior to SEM observation.

The porosity and chemical composition of the multilayers were determined using the ellipsometric method summarized in Chapter 6. In brief, all-nanoparticle multilayers (12 bilayers) assembled on Si substrates at different assembly conditions were first calcinated at 550 °C for 2 h. The calcination prevents the swelling of films in water. The refractive indices of the films were then measured in air ($n_{f,1}$) and in water ($n_{f,2}$) by using the ellipsometer. The porosity and the chemical composition of the multilayers are then calculated by the following equations:

$$p = \frac{n_{f,2} - n_{f,1}}{n_{f,water} - n_{f,air}} = \frac{n_{f,2} - n_{f,1}}{0.33} \tag{7.2}$$

$$v_{TiO_2} = \frac{n_{f,framework} - n_{f,SiO_2}}{n_{f,TiO_2} - n_{f,SiO_2}} \cdot (1 - p) \tag{7.3}$$

$$v_{SiO_2} = 1 - (p + v_{TiO_2}) \tag{7.4}$$

where, v, p, and n_f represent the volume fraction of each nanoparticle, porosity and refractive index of nanoparticles. Framework denotes the solid materials in the multilayer thin films which consist of TiO_2 and SiO_2 nanoparticles. For detailed derivation of the equations 7.2 – 7.4, see Section 6.3.2. Refractive indices of the TiO_2 and SiO_2 nanoparticles were determined to be 2.29 and 1.45, respectively. These values are within experimental errors of the values for each nanoparticle obtained

in Chapter 6. The chemical composition of the multilayers is reported in weight fraction of TiO_2 nanoparticles using the density of each nanoparticle (TiO_2 = 3.9 g/cm^3 and SiO_2 = 1.3 g/cm^3)[259].

7.3 Results and Discussion

7.3.1 pH-dependent growth behavior of TiO_2/SiO_2 multilayers

All-nanoparticle multilayer thin films comprising 7 nm TiO_2 and 22 nm SiO_2 nanoparticles were assembled onto glass or Si substrates to determine average bilayer thicknesses. Figure 7.1 is an example of the variation of average bilayer thickness with assembly conditions. In this case, the pH of the TiO_2 nanoparticle suspension was held constant at pH 3.0 while that of the SiO_2 nanoparticle suspension was varied from 2.0 to 5.0 by a single pH unit. Thicknesses were measured every three bilayers up to 12 bilayers for each condition and then the average bilayer thickness was determined using linear regression. To eliminate the effect of substrates, the regression lines were drawn without forcing the fit through the origin. In all cases, the R-squared values were greater than 0.95 indicating that the multilayers assembled at all conditions showed linear growth behavior up to 12 bilayers. The fact that some of the regression lines do not go through the origin, however, indicates the existence of substrate effects in the first few bilayers of the multilayer films.

Following the procedure described above, twelve different combinations of pH conditions were used to create a matrix of average bilayer thickness as shown in Figure 7.2. Depending on the assembly conditions, multilayers can show either very little growth (~ 2 nm/bilayer) or a large growth (~ 30 nm/bilayer) after a sequential exposure of substrates to TiO_2 and SiO_2 nanoparticle suspensions. Clear trends are observed as the assembly conditions were changed. For a constant pH of the SiO_2 suspension, the average bilayer thickness increases as the pH of the TiO_2 suspension is increased. For a constant pH of the TiO_2 nanoparticle suspension, on the other hand, the average bilayer thickness

goes through a maximum at pH 3.0 for the SiO_2 nanoparticle suspensions. Iler also observed that the multilayer assembly of SiO_2 nanoparticles and positively charged colloidal particles such as alumina showed the maximum growth at pH 3.0 when the pH of the positively charged particle suspension was held constant at 4.0.[18] All multilayers shown in Figure 7.2 yielded completely transparent films with high uniformity. When the pH of the TiO_2 nanoparticles was increased to pH 5.0, the films became cloudy, independent of the pH of the SiO_2 suspensions. As will be described below, the opaqueness of the films assembled at pH 5.0 is likely due to the formation (and adsorption) of large TiO_2 nanoparticle aggregates in the suspension.

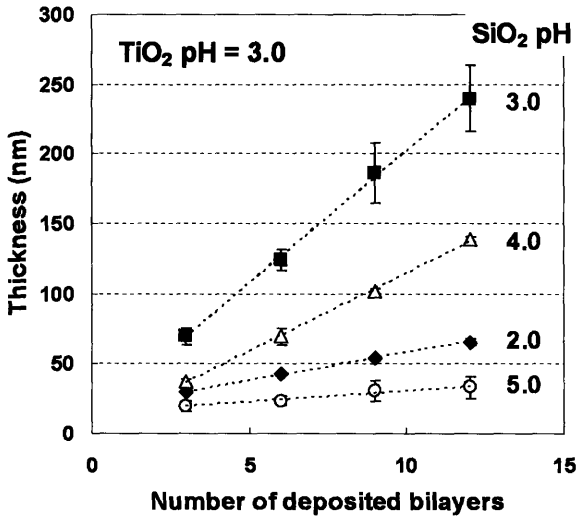

Figure 7.1. Increase in thickness of TiO_2 3.0/SiO_2 *y* multilayers as a function of number of deposited bilayers, where *y* is the pH of the SiO_2 nanoparticle suspension. The values of *y* are shown in the legend of the graph. The nanoparticle multilayer thin films were assembled on glass substrates.

The results obtained in Figure 7.2 indicate that there exists a narrow regime of pH conditions in which assembly proceeds in a "successful" layer-by-layer manner. Specifically, the average bilayer thickness observed for all conditions except the pH range between 3.0 and 4.0 for both nanoparticle suspensions is significantly less than the diameter of the SiO_2 nanoparticles themselves. Therefore,

successful LbL assembly leading to significant adsorption of nanoparticles at each deposition step occurs only within this narrow assembly window. As will be shown below, the complete charge reversal of multilayers after each nanoparticle deposition step is essential for successful LbL assembly.

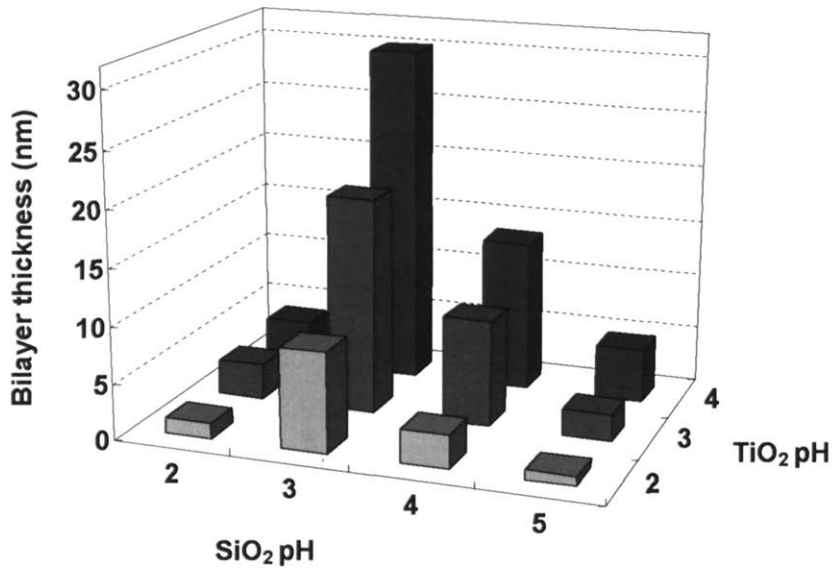

Figure 7.2. pH matrix showing the average bilayer thickness of 7 nm TiO_2/22 nm SiO_2 nanoparticle multilayers as a function of nanoparticle suspension pH. At least two measurements were made and averaged for each multilayer. Error in average bilayer thickness for each multilayer is less than 2.5 nm.

To better understand the effect of pH on the growth behavior of the TiO_2/SiO_2 nanoparticle multilayers, the zeta-potential and the size of nanoparticles (or that of nanoparticle aggregates) as a function of suspension pH were determined as shown in Figure 7.3. For SiO_2 nanoparticles, the surface charge density decreases as the pH of the suspension decreases; the isoelectric point is reached around pH 2.0. The size of the SiO_2 entities in suspension, determined by dynamic light scattering (DLS), does not vary significantly over the pH range that was used for multilayer assembly,

indicating that even though the surface charge density of the SiO_2 particles changes significantly from pH 5.0 to 2.0, the particles are quite stable against flocculation. Excellent colloidal stability of SiO_2 nanoparticles near their isoelectric point has been well documented and reported by others.[260-262] In the case of TiO_2 nanoparticles, the charge density of the nanoparticles continually decreases above pH 3.0. The TiO_2 nanoparticles used in this study exhibited an isoelectric point near pH 7.0 which is consistent with reported values for TiO_2 nanoparticles.[263-265] The observed decrease of the zeta-potential at pH 2.0 is likely due to compression of the electric double layer as the ionic strength increases at such a low pH.[266] The size of suspended TiO_2 entities, determined via DLS, increases with increasing pH, indicating that these nanoparticles flocculate into large clusters at pH values higher than 3.0. At pH 5.0, the size of the aggregates is larger than the TiO_2 nanoparticles at pH 3.0 by a factor of 5, and some precipitation of nanoparticle aggregates was observed. The observation of a relatively low colloidal stability of TiO_2 nanoparticles compared to SiO_2 nanoparticles near the isoelectric point also has been observed by others.[264,267,268] As briefly mentioned above, the formation and adsorption of large aggregates of TiO_2 nanoparticles at pH 5.0 leads to the formation of the multilayers that scatter light.[g]

Figure 7.3(a) explains the reason behind the observed negligible multilayer growth when the pH of SiO_2 nanoparticle suspension is 2.0 regardless of TiO_2 pH (Figure 7.2). Because the SiO_2 nanoparticles are barely charged near their isoelectric point at pH 2.0, their electrostatic interaction with positively charged TiO_2 nanoparticles is extremely weak, leading to the negligible bilayer growth observed. It is reasonable to postulate that negligible multilayer growth would also be observed if the pH of TiO_2 nanoparticle suspension was adjusted to 7.0; however, due to the

---

[g] Average bilayer thickness of (TiO_2 5.0/SiO_2 3.0) and (TiO_2 5.0/SiO_2 5.0) were determined to be ~ 30 and 3 nm as determined via ellipsometry. These films are opaque and scatter light.

aggregation and precipitation of TiO_2 nanoparticles above pH 5.0 (Figure 3(b)), this regime cannot be accessed experimentally.

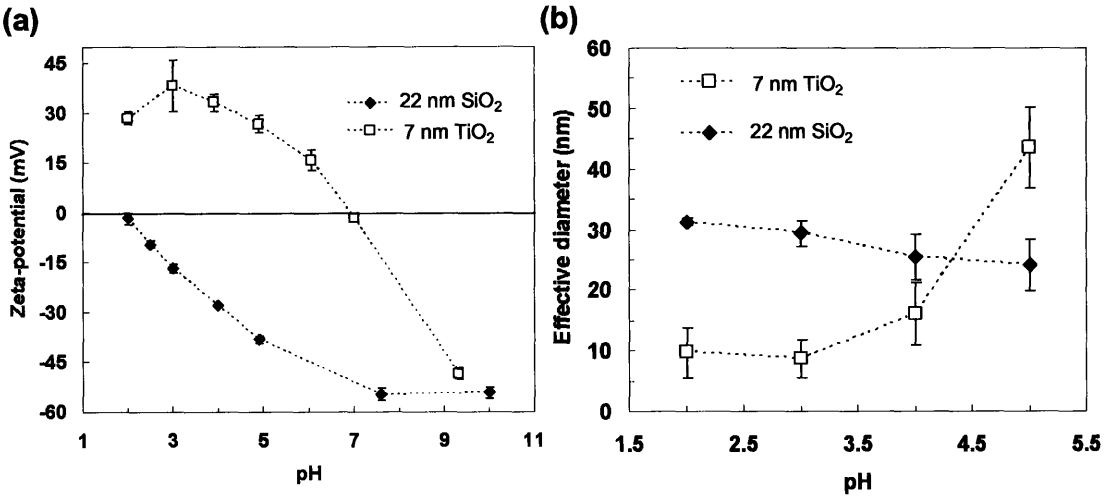

Figure 7.3. (a) Zeta-potential and (b) effective diameter of suspended nanoparticles determined by dynamic light scattering as a function of nanoparticle suspension pH.

The zeta-potential of TiO_2/SiO_2 nanoparticle multilayer coated polystyrene microspheres was monitored after each deposition step to provide important insight on the effect of assembly conditions on the surface charge density of multilayers during the adsorption of nanoparticles. For this purpose, two conditions were chosen: TiO_2 3.0/SiO_2 3.0 and TiO_2 3.0/SiO_2 5.0. While the former condition exhibited a bilayer growth of ca. 20 nm, the latter showed very limited growth of ca. 2 nm per bilayer. The comparison of these two extreme cases revealed important information regarding the dependence of layer thickness on assembly conditions. After the adsorption of each nanoparticle layer, coated PS microspheres were dispersed in deionized water whose pH was adjusted to the same value as that of the next nanoparticle suspension. For example, in the case of TiO_2 3.0/SiO_2 5.0 multilayers, after the adsorption of TiO_2 nanoparticles at pH 3.0 and three rinse steps, the coated PS microspheres were then dispersed in pH 5.0 adjusted-DI water for the measurement of zeta-potential. This scheme

allowed us to probe the surface charge density at each nanoparticle deposition step and its subsequent effect on the adsorption of nanoparticles.

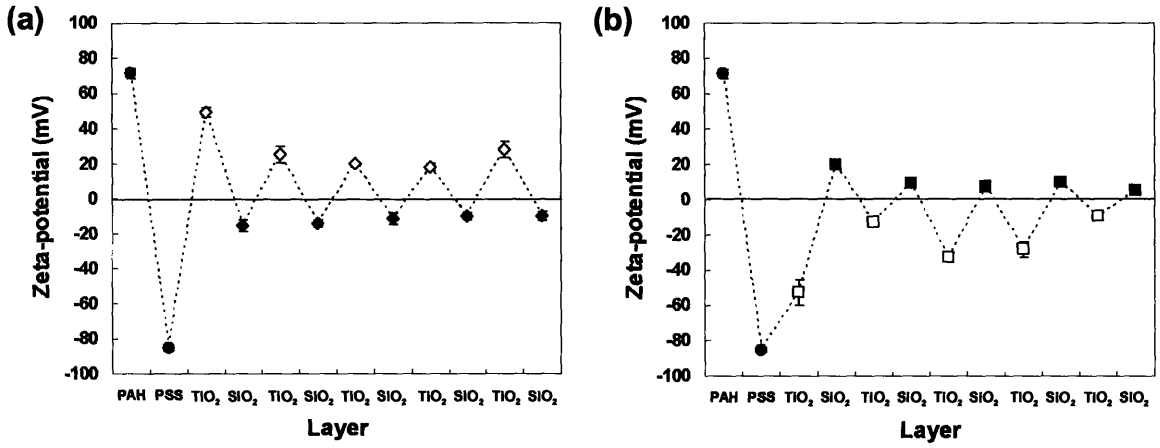

Figure 7.4. Zeta-potential variation of (TiO_2 3.0/SiO_2 3.0) and (TiO_2 3.0/SiO_2 5.0) multilayers deposited on 1.5 μm polystyrene (PS) microparticles. The PS particles were coated with 5 bilayers of (PAH/PSS) multilayers prior to the deposition of TiO_2/SiO_2 multilayers. Filled and open symbols in each figure represent zeta-potentials of coated PS microspheres after adsorption of SiO_2 and TiO_2 nanoparticles, respectively.

Figure 7.4(a) clearly shows that for TiO_2 3.0/SiO_2 3.0 multilayers, after deposition of each nanoparticle layer, the surface charge of the multilayer is completely reversed. This charge reversal leads to a complete adsorption from the next nanoparticle suspension in the processing scheme. It is a well-understood fact that charge reversal after deposition of each layer of polyelectrolyte or charged nanoparticles is essential for a successful build-up of multilayer thin films.[19-21]

In the case of the TiO_2 3.0/SiO_2 5.0 multilayers, however, each nanoparticle adsorption step does not necessarily induce charge reversal (Figure 7.4(b)). Specifically, after deposition step of positively charged TiO_2 nanoparticles at pH 3.0, the coated-PS microspheres still exhibit a negative surface charge at pH 5.0, whereas the coated PS microspheres have positive surface charge in pH 3.0 water

after the deposition step of silica nanoparticles at pH 5.0. These results preclude any significant electrostatically driven nanoparticle adsorption in this set of processing conditions, consistent with the very low value of bilayer thickness observed at TiO_2 3.0/SiO_2 5.0 (Figure 7.2). The major reason for the observed negligible growth of multilayers at numerous other conditions (i.e., conditions except for pH ranges between 3.0 and 4.0) observed in Figure 7.2 is believed to be due to the incomplete charge reversal after the deposition of each nanoparticle layer.

The observed incomplete charge reversal is likely due to the changes in the surface charge density of nanoparticles near the surface of the multilayer thin films. For example, when SiO_2 nanoparticles are adsorbed at pH 5.0, their surface charge density is relatively high as evidenced by the zeta-potential value in Figure 7.3. SiO_2 nanoparticles will adsorb on top of previously adsorbed TiO_2 nanoparticles but because of the high charge density of the SiO_2 nanoparticles and low surface charge of the previously adsorbed TiO_2 nanoparticle layers, SiO_2 nanoparticles cannot adsorb into dense layers on top of the TiO_2 nanoparticle layers. When the SiO_2 nanoparticle-coated surface is exposed to a TiO_2 nanoparticle suspension at pH 3.0, the surface charge density of the outermost SiO_2 nanoparticle layer decreases and that of the underlying TiO_2 nanoparticles increases. Due to the changes in the surface charge density of nanoparticles near the surface, the multilayer exhibits positive surface charge overall leading to little adsorption of positively charged TiO_2 nanoparticles from the suspension. Therefore, continuous exposure of the substrates to nanoparticle suspensions at this condition (i.e., TiO_2 3.0/SiO_2 5.0) only leads to the negligible growth observed in Figure 7.2.

The effect of assembly conditions on the growth of multilayers could be directly observed by creating hollow microcapsules of all-nanoparticle multilayers assembled at the two conditions mentioned above. Hollow microcapsules comprising TiO_2 and SiO_2 nanoparticles were obtained by calcinating the PS microspheres after the deposition of five bilayers of TiO_2 and SiO_2 nanoparticles at the two conditions. Figure 7.5 shows that depending on the assembly conditions two completely

different microcapsules can be prepared. The calcinated hollow microcapsules (as evidenced by a broken capsule in inset of Figure 7.5(a)) assembled at (TiO_2 3.0/SiO_2 3.0) show that due to the thick capsule walls, the microcapsules do not undergo the collapse that occurs during calcination of microcapsules assembled at (TiO_2 3.0/SiO_2 5.0). The collapsed microcapsules (Figure 7.5(b)) indicate that due to the incomplete charge reversal, these capsule walls are extremely thin even after the five cycles of the deposition process.

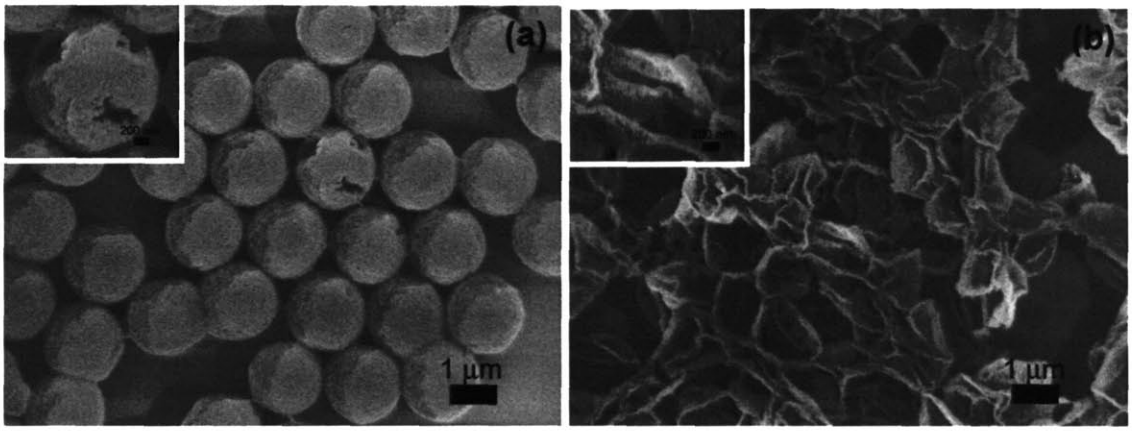

Figure 7.5. SEM images of (a) (TiO_2 3.0/SiO_2 3.0)$_5$ and (b) (TiO_2 3.0/SiO_2 5.0)$_5$ hollow microcapsules. Samples prepared by depositing five bilayers of TiO_2 and SiO_2 nanoparticles on top of (PAH/PSS)$_5$ coated PS microspheres were calcinated at 550 °C for 2 h. Due to the uneven evaporation of Au/Pd coatings for SEM imaging, the image on the top shows incomplete coatings of Au/Pd on TiO_2/SiO_2 hollow microcapsules. Insets show high magnification images of hollow microcapsules.

7.3.2 Effect of assembly conditions on chemical composition, porosity and refractive index of TiO_2/SiO_2 multilayers

As shown in Chapter 6, all-nanoparticle thin films comprising TiO_2 and SiO_2 nanoparticles have self-cleaning properties due to the presence of TiO_2 nanoparticles. Also these films are porous in nature because of the presence of interstitial void volume between randomly packed nanoparticles.[259] The control of the porosity of these films will enable, for example, the

investigation of effect of porosity on wetting behavior or on mechanical properties[13] of these all-nanoparticle thin films. Also the ability to control chemical composition by controlling the assembly conditions of these all-nanoparticle multilayers would offer great advantages in creating functional thin films for specific applications. For example, Nakajima et al. have shown that a precise control over the amount of TiO_2 is crucial in maintaining the long-term stability of the superhydrophobicity in self-cleaning transparent superhydrophobic thin films.[251] The effect of assembly conditions on chemical composition, porosity and refractive index of the TiO_2/SiO_2 nanoparticle multilayers was investigated using a method based on ellipsometry described briefly in the Experimental section and in detail in Section 6.3.2. This method allows the determination of porosity and chemical composition without making any assumption about the refractive index of each nanoparticle.

Figure 7.6(a) shows that the TiO_2 content in these all-nanoparticle multilayers can be varied from 5 to 25 wt. %. Within pH ranges where the average bilayer thickness is comparable to the size of the nanoparticles (i.e., pH range between 3.0 and 4.0 for both nanoparticle suspensions), the TiO_2 content could be varied from ca. 5 to 20 wt. %. In general, increasing the pH of each nanoparticle suspension increased the amount of TiO_2 nanoparticles in the multilayers. An understanding of effect of assembly conditions on chemical composition of the multilayers enables the fabrication of all-nanoparticle thin films with desirable amount of TiO_2 nanoparticles. It should be possible, for example, to create self-cleaning thin films with varying degree of photocatalytic activities.

The porosity of these films can also be varied as much as 10 % depending on the assembly conditions as seen in Figure 7.6(b). It is noteworthy that the assembly pH that leads to thick bilayer growth results in lower porosity. This result indicates that the conditions that favor thick bilayer growth also favor adsorption of densely packed nanoparticle layers. In addition to the control of assembly conditions, the results in Chapter 6 have shown that the use of nanoparticles of different sizes provides another approach to control the porosity of these all-nanoparticle thin films.[259]

Figure 7.6(c) shows that although changes in the refractive index of the films are observed, the difference in the refractive index between different conditions is very small (less than 0.05), even though the average bilayer thickness varies considerably (Figure 7.2). The lack of significant changes in the refractive index of the films can be explained by the fact that multilayer assembly conditions that lead to higher porosity, in general, result in greater volume fraction of TiO_2 nanoparticles in the multilayer thin films. As TiO_2 nanoparticles have a high refractive index of ~ 2.3, a greater volume fraction of TiO_2 nanoparticles will offset the effect of a higher porosity; this self-compensatory behavior causes the refractive indices of the all-nanoparticle films studied here to remain essentially constant.

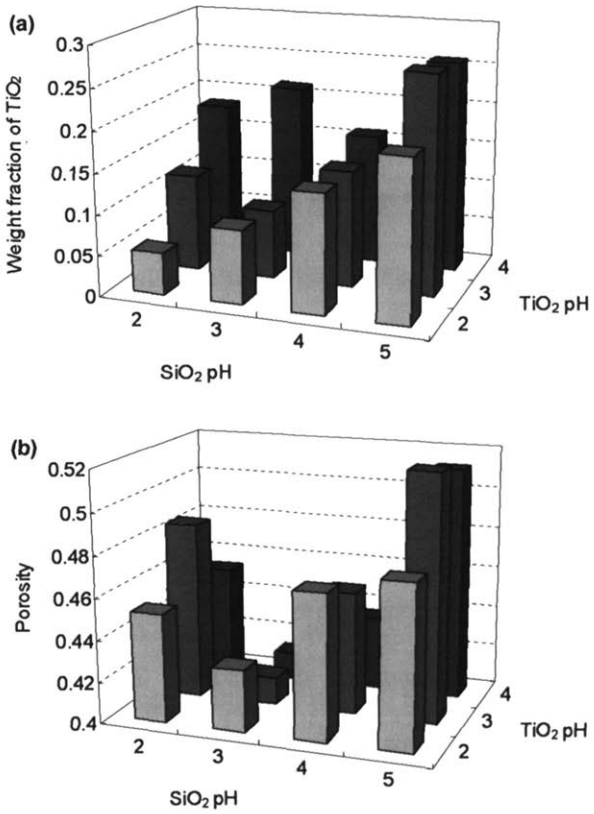

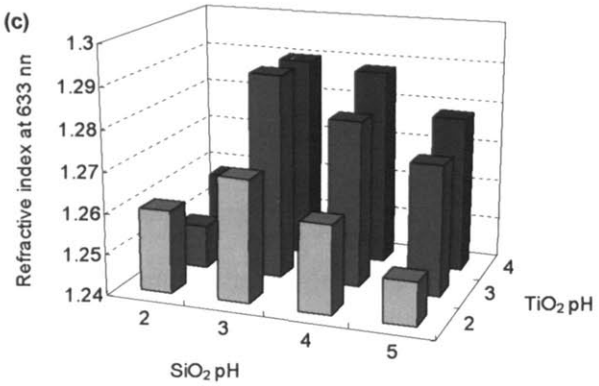

Figure 7.6. (a) Weight fraction of TiO_2 nanoparticles, (b) porosity and (c) effective refractive index of the multilayers as a function of assembly pH as determined via ellipsometry. TiO_2/SiO_2 nanoparticle multilayer thin films with 12 bilayers were assembled on Si substrates for the determination of porosity and chemical composition.

7.4 Conclusions

In this chapter, it was demonstrated that by controlling the assembly conditions (i.e., pH of each nanoparticle suspension) of multilayers comprising oppositely charged TiO_2 and SiO_2 nanoparticles, it is possible to vary the average bilayer thickness of multilayers as well as the porosity and chemical composition. Changes in the zeta-potential of TiO_2/SiO_2 multilayers assembled on polystyrene microspheres at different conditions indicated that while complete charge reversal after each nanoparticle adsorption step leads to the growth of thick layers, incomplete charge reversal results in very little incremental growth. The chemical composition and porosity of these all-nanoparticles also could be varied by controlling the assembly conditions. These observations will facilitate the fabrication of all-nanoparticle thin films with characteristics to suit specific applications. The refractive index of the TiO_2/SiO_2 nanoparticles multilayers showed negligible changes within the assembly conditions employed.

Chapter 8

All-Silica Nanoparticle Multilayer Thin Films: Effect of Surface Charge Density of Nanoparticles on Multilayer Assembly

8.1 Introduction

Two previous chapters have demonstrated that all-nanoparticle thin films based on electrostatically driven layer-by-layer (LbL) deposition of oppositely charged nanoparticle can be created.[259] These all-nanoparticle thin films made from TiO_2 and SiO_2 nanoparticles exhibited potentially useful antifogging, antireflection and self-cleaning properties. Originally, this method was developed and pioneered by Iler in 1966.[18] The LbL technique is extremely versatile in the fact that uniform thin films with a wide range of properties can be prepared onto various substrates including colloidal particles[26,27] and porous membranes[29,30,32,204,269]. However, it has been most widely used for the preparation of multilayer thin films from two oppositely charged polymers or from a charged nanoparticle and an oppositely charged polymer.[16,17] While enormous amount of fundamental knowledge on the formation of multilayers containing polyelectrolytes has been accumulated over the years[16,17], very little is known about the formation of multilayers consisting of oppositely charged nanoparticles.

To exploit the full potential of all-nanoparticle multilayers, it is essential to understand the effects of various assembly parameters (e.g., assembly pH, ionic strength, concentration of nanoparticle suspension and size of nanoparticles) on the formation of all-nanoparticle multilayers. In this chapter, the effect of assembly conditions on the growth behavior of all-silica (SiO_2) nanoparticle multilayers using nanoparticles of different sizes is investigated. The size and surface charge character of the nanoparticles used in the study are analyzed using transmission electron microscopy and zeta-potential analyzer. The effect of nanoparticle size on the average bilayer

thickness (thickness after a sequential adsorption of positively charged and negatively charged silica nanoparticles) and porosity of the multilayers is also studied.

8.2 Experimental Methods

Materials. 3-Aminopropyl-functionalized silica nanoparticles (AP-SiO_2) (3 % (w/v) in ethanol), Ludox SM-30 (30 wt. % SiO_2 suspension in water), Ludox HS-40 (40 wt. % SiO_2 suspension in water), and Ludox TM-40 (40 wt. % SiO_2 suspension in water) were obtained from Sigma-Aldrich (St. Louis, MO).

Assembly of all-SiO_2 nanoparticle multilayers. Sequential adsorption of oppositely charged silica nanoparticles was performed on either glass slides or silicon wafers by using an automatic dipping machine; the dipping time for nanoparticles was 10 min followed by three rinses in milli-Q (MQ) water: one 2 min and two 1 min rinses. In some cases, the substrates were primed with 5 bilayers of sequentially adsorbed poly(allylamine hydrochloride) (PAH) and poly(styrene sulfonate) (PSS) multilayers. The use of the adhesion layers, however, did not alter the results significantly. The concentration was 0.03 % (w/v) and the pH of nanoparticle suspensions were adjusted using 1.0 M HCl or NaOH. AP-SiO_2 nanoparticles were suspended into acidified deionized water (pH < 3.0) to facilitate ionization of the amine groups on the surface of AP-SiO_2 nanoparticles. Negatively charged silica nanoparticles were added into deionized water without any pretreatment. The pH of each nanoparticle suspension was checked after every three bilayers of deposition (i.e., every ~ 1.5 h). Thicknesses were measured every three bilayers at least up to 12 bilayers for each condition and then the average bilayer thickness was determined via linear regression. The regression lines were drawn without forcing the fit through the origin.

Characterization. Variable-angle spectroscopic ellipsometry (VASE) measurements were made on multilayer films assembled on silicon wafers by using a Woolham Co. VASE spectroscopic

ellipsometer; the data analysis was done using the WVASE32 software package. Measurements were performed from 250 to 900 nm at an angle of incidence of 70°. Film thicknesses were determined over this range, and refractive index values were determined at 633 nm. After a sample was placed in a trapezoid quartz cell (Hellma), film thickness and effective refractive index of the films were first measured in air. Thickness and effective refractive index of the films in ethanol was then made on the same location by adding ethanol to the quartz cell. The difference in the thickness in the two media was typically less than 2 % indicating that the multilayers did not undergo any swelling in ethanol.

8.3 Results and Discussion

8.3.1 Effect of Assembly Conditions on Growth Behavior of All-Silica Nanoparticle Multliayers

Multilayer thin films consisting of three different combinations of silica nanoparticles were assembled. Negatively charged silica nanoparticles of three different sizes were assembled into multilayers paired with one type of positively charged silica nanoparticle. Figure 8.1 shows the representation of silica nanoparticles used in this study, drawn to scale to illustrate their relative sizes. The average size and standard deviation of each nanoparticle were determined via transmission electron microscopy (TEM) and are summarized in Figure 8.1. The size distribution of each nanoparticle is narrow enough that a negligible portion of each nanoparticle suspension contains nanoparticles of the other sizes.

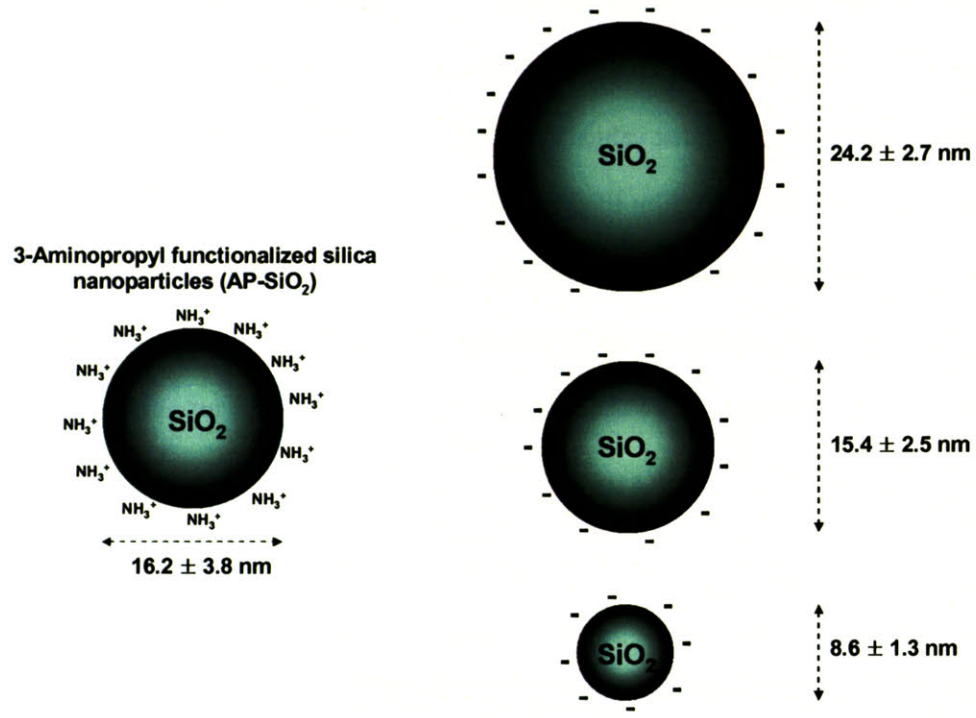

Figure 8.1. Representation of SiO_2 nanoparticles used in this study. The nanoparticles are drawn to scale to show their relative sizes. The average size and standard deviation of each nanoparticle were determined by measuring at least 50 nanoparticles.

The effect of assembly conditions on the growth behavior of each system was studied. Figure 8.2 shows the variations in the average bilayer thickness of AP-SiO_2/SiO_2 nanoparticle multilayer thin films as a function of suspension pH for the particular case in which both suspensions were kept at the same pH. In all three cases, the average bilayer thickness exhibited a maximum; however, the pH value at which the maximum occurred was different for each system. Results obtained in Chapter 7 using 24.2 nm SiO_2 and positively charged TiO_2 nanoparticles showed that the multilayers exhibited the maximum thickness growth when the pH of 24.2 nm SiO_2 nanoparticle suspension was adjusted to 3.0. Iler also observed that when negatively charged silica nanoparticles were assembled with positively charged alumina[18], the growth was maximized at pH 3.0, which is consistent with the

results for multilayers made from AP-SiO_2 and 24.2 nm silica nanoparticles. However, the multilayers comprising AP-SiO_2/15.4 nm SiO_2 and AP-SiO_2/8.6 nm SiO_2 exhibited maximum growth at pH 4.5 and 5.0, respectively. Considering that pH is a logarithmic unit of concentration, these differences are quite large. It is noteworthy that pH-dependent growth behavior has been also observed by others with polyelectrolyte/nanoparticle multilayers and that these systems also exhibited maximum growth at an optimized pH condition.[270,271]

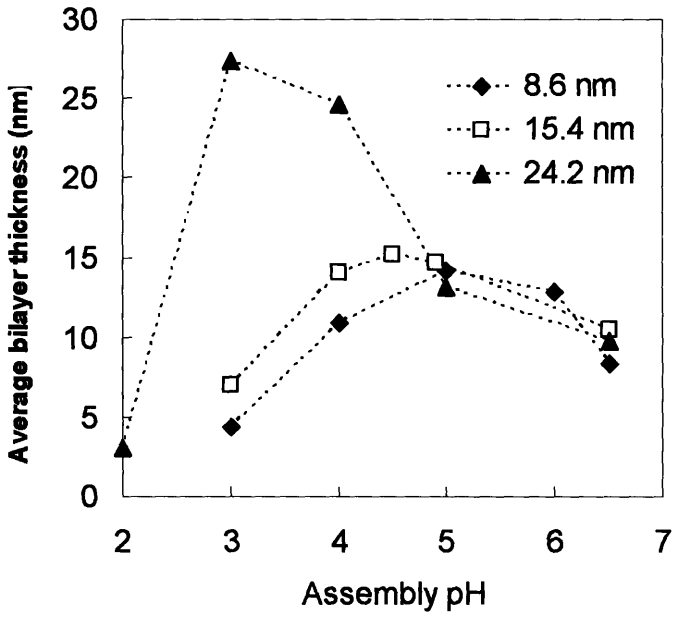

Figure 8.2. Average bilayer thickness of multilayers comprising positively charged AP-SiO_2 and negatively charged silica nanoparticles of different sizes. Multilayers were assembled on silicon substrates and the thicknesses were measured using a spectroscopic ellipsometer. At least 12 bilayers were assembled to determine the average bilayer thickness for each multilayer.

Figure 8.2 shows that at many pH values other than the "optimized condition" for the maximum growth, the average bilayer thickness of multilayers is smaller than the size of nanoparticles assembled. A similar trend in the growth behavior of multilayers consisting of polyelectrolytes and

yttrium iron garnet (YIG) nanoparticles was observed by Kotov et al.[52] They reported that the average bilayer thickness of multilayers measured via ellipsometry (3.5 nm) was significantly smaller than the size of the YIG nanoparticles (32 nm). They observed that these multilayers formed isolated domains of nanoparticles in the initial stages of growth and that these domains grew in size and in number as the number of deposition cycles was increased. They concluded that the small growth observed was due to the incomplete coverage of nanoparticles at each deposition step leading to what they termed as a lateral expansion mode.[52]

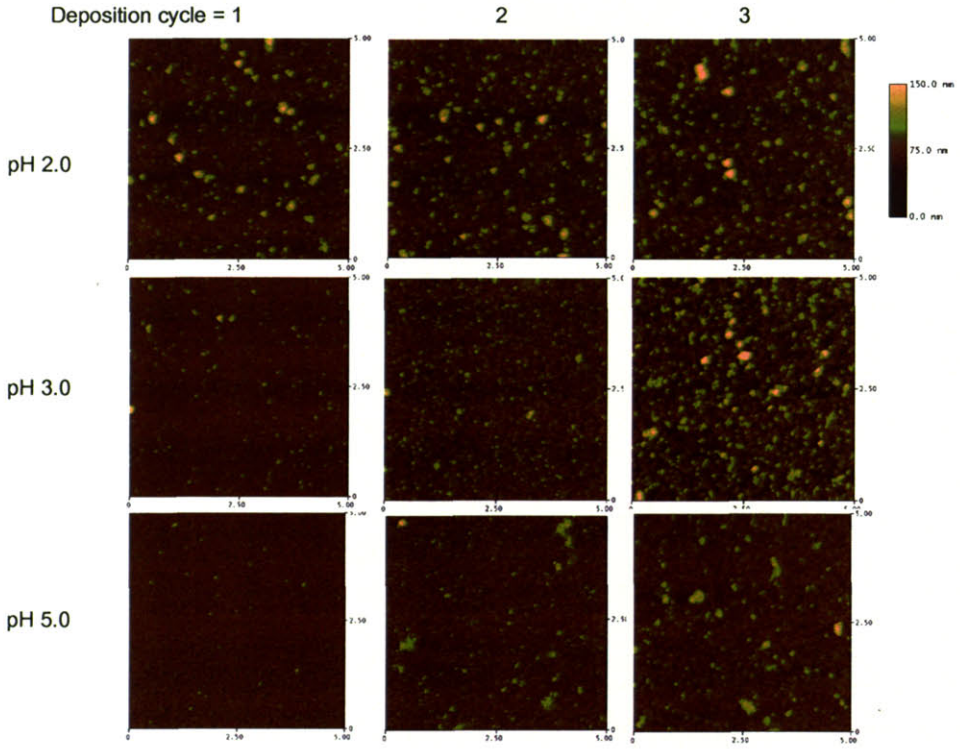

Figure 8.3. Atomic force microscopy (AFM) images of all-silica nanoparticle (AP-SiO_2/24.2 nm SiO_2) multilayers deposited at different assembly conditions (i.e., pH). Row 1, 2, and 3 corresponds to multilayers assembled at pH 2, 3, and 5, respectively. Column 1, 2, and 3 corresponds to multilayers after 1, 2, and 3 deposition cycles, respectively. Each side of the AFM images is 5 μm.

The growth of all-silica nanoparticle multilayers in the early stages at different assembly conditions was studied by atomic force microscopy (AFM). Multilayers consisting of AP-SiO_2 and

24.2 nm SiO_2 nanoparticles were assembled at three different assembly conditions (i.e., pH 2.0, 3.0 and 5.0[h]). Figure 8.3 shows that in all three cases the first deposition cycle (a sequential exposure of the substrate into two nanoparticle suspensions) results in the formation of a continuous layer of densely packed nanoparticles on the surface. Multilayers assembled at a lower pH tend to show a larger number of aggregated clusters of nanoparticles likely due to the loss of surface charge of silica nanoparticles near the isoelectric point (pH 2.0). After the second deposition cycle, multilayers assembled at pH 2.0 and 5.0 show increased number of isolated domains of aggregated nanoparticles (size ranging between 100 and 800 nm) atop the first bilayer of nanoparticles. On the other hand, the surface topology of the multilayer assembled at pH 3.0 became rougher over the entire area indicating that a layer of densely adsorbed nanoparticles was formed on top of the first bilayer. After the third deposition cycle, the trend continues. The multilayers assembled at pH 2.0 and 5.0 show increased number of isolated domains of nanoparticles, whereas the multilayer assembled at pH 3.0 exhibits increased surface roughness over the entire area. These observations indicate that multilayers assembled at non-optimized conditions tend to grow in a "fill-in" mode, producing isolated domains of aggregated nanoparticles at each deposition cycle instead of a continuous layer of nanoparticles. Due to the incomplete coverage at these non-optimized conditions, the increase in the thickness determined via ellipsometry is significantly smaller than the size of nanoparticles assembled. While Kotov et al. was able to create continuous layers of densely packed nanoparticles at each deposition step by modifying the surface of YIG nanoparticles[52], the results in this chapter show that the same effect can be achieved by optimizing the assembly conditions.

---

[h] These conditions were chosen because each condition represents three different regimes of growth; that is, at pH 2.0, 3.0 and 5.0, multilayers showed negligible (average bilayer thickness significantly smaller than the size of both nanoparticles), maximum (average bilayer thickness commensurate with the larger particle (TM-40)) and intermediate growth (average bilayer thickness in between the size of two nanoparticles), respectively.

Figure 8.4 provides important information about the surface charge density of the nanoparticles as a function of pH, and it points to a guiding framework for successful LbL assembly of charged nanoparticles. It can be seen in Figure 8.4 that the variation in surface charge density for the three negatively charged nanoparticles is quite different. At pH 3.0, for example, 15.4 nm and 8.6 nm SiO_2 nanoparticles have less surface charge than 24.2 nm silica nanoparticles. Most importantly, the zeta-potentials of all three negatively charged silica nanoparticles at the solution pH that results in the maximum growth are approximately the same (zeta potential of ca. -15 ~ -17 mV). Variations in the surface charge density of the negatively charged particles are the only factor that is affecting the growth of these multilayers since the surface charge density of AP-SiO_2 nanoparticles does not change within the pH range between 2 and 6. These results suggest it is the surface charge density that is crucial in determining the optimal LbL growth condition for a selected pair of nanoparticles. While extremely low surface charge on nanoparticles results in little growth due to weak electrostatic interactions, too much charge also results in little growth presumably due to strong electrostatic repulsion between highly charged nanoparticles that are being added in each subsequent assembly step.

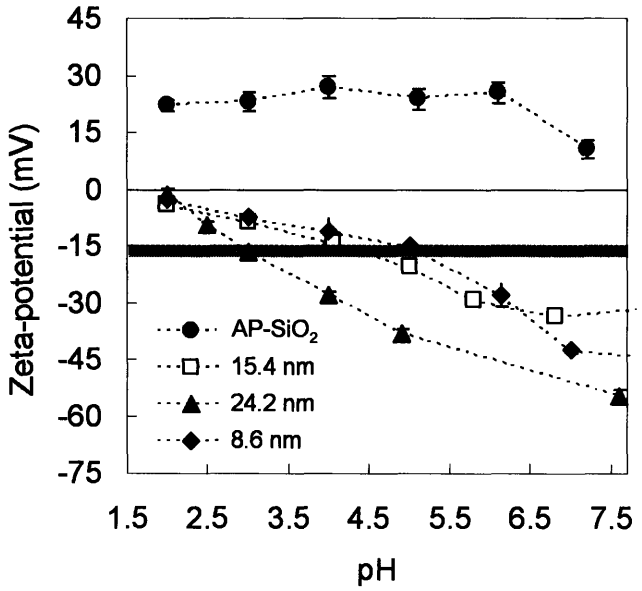

Figure 8.4. Zeta-potential of SiO_2 nanoparticles as a function of pH. The gray area shows the region of optimized assembly condition (zeta-potential -15 ~ -17 mV) for the AP-SiO_2/SiO_2 multilayer systems.

Based on Figure 8.2 and Figure 8.4, a non-dimensional plot was created to determine if any general behavior could be deduced from these results. Figure 8.5 shows the variation in the normalized thickness (reference (t_0) = maximum thickness of each system) as a function of normalized zeta-potential (reference (z_0) = + 23 mV, zeta-potential of positively charged silica nanoparticles in the pH range between 2 and 6). The three curves superpose reasonably well onto a single mater curve, indicating that in all three cases the maximum in the thickness (relative thickness = 1) occurs when the surface charge (absolute value of zeta-potential) of the negatively charged particles is about $0.7z_0$. The universality of the behavior observed in Figure 8.5 can be examined by varying z_0, the charge density of positively charged nanoparticles. Positively charged silica with varying charge density may be generated by modifying the surface of SiO_2 nanoparticles with a different ratio of 3-aminopropyltriethoxysilane (APTES) and alkylsilane compound.

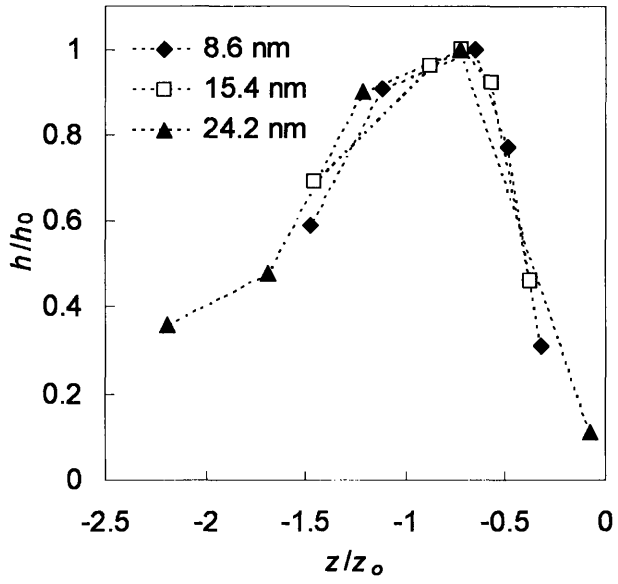

Figure 8.5. Normalized average bilayer thickness as a function of normalized zeta-potential for each multilayer system. Average bilayer thickness (h) and zeta-potential of negatively charged particles (z) were normalized by the maximum thickness of each system (h_0) and zeta-potential of positively charged silica nanoparticle (z_0; determined in the range of pH 2 and 6), respectively.

8.3.2 Effect of Size of Nanoparticles on Structure of All-Silica Nanoparticle Multilayers

The all-nanoparticle multilayer thin films are porous in nature due to the presence of interstitial void volume.[59,259] Nanoporosity leads to potentially useful antifogging and antireflection properties. Antireflection behavior, in particular, is sensitive to the refractive index and thickness of thin films. For example, optical thickness (product of refractive index and thickness) determines the wavelength of maximum suppression of reflectance. The ability to tune these two structural parameters, therefore, is crucial in designing antireflection coatings suitable for specific applications. Also by controlling the porosity in these films, it would be possible to study the effect of porosity on wetting behavior.

The effect of nanoparticle size on porosity and average bilayer thickness was investigated using the method described in Chapter 6.[259] In brief, the effective refractive indices[i] of the multilayer thin films were measured in two different media (i.e., air and ethanol). Based on the simplest form of an effective medium approximation, the porosity and refractive index of the constituent silica nanoparticles can be expressed as follows (for detailed derivation of the equations, see Chapter 6):

$$p = \frac{n_{f,2} - n_{f,1}}{n_{f,ethanol} - n_{f,air}} = \frac{n_{f,2} - n_{f,1}}{0.36} \qquad (8.1)$$

$$n_{f,nanoparticles} = \frac{n_{f,1} - n_{f,air} \cdot p}{1 - p} \qquad (8.2)$$

where p represents the porosity (or the fraction of void volume) of the porous thin films, and $n_{f,air}$ (1.00), $n_{f,ethanol}$ (1.36), and $n_{f,\ nanoparticles}$ represent the refractive indices of air, ethanol and the constituent silica nanoparticles, respectively. $n_{f,1}$ and $n_{f,2}$ represent the experimentally measured effective refractive indices of the porous thin films in media 1 (in air) and 2 (in ethanol), respectively.

Table 8.1 summarizes the dependence of some of the physical properties determined using an ellipsometer on the size of the SiO_2 nanoparticles. Each multilayer was assembled at the pH that results in the maximum growth behavior. The growth behavior of the multilayers depends on the size of nanoparticles as shown in Figure 8.2; that is, the use of larger particles leads to thicker bilayers. The porosities and effective refractive indices of three systems, however, do not differ significantly. Small changes in the porosity, nevertheless, indicate that multilayers containing larger negatively charged silica nanoparticles (i.e., 24.2 nm SiO_2) tend to have somewhat greater porosity. This result is also consistent with the previous findings in Chapter 6, where multilayers comprising 7 nm TiO_2 nanoparticles and 8.6 nm SiO_2 nanoparticles exhibited smaller porosity than the multilayers

[i] The term "effective refractive index" ($n_{f,1\ and\ 2}$) refers to the refractive index of the entire porous thin film experimentally measured via ellipsometry.

assembled with larger 24.2 nm SiO_2 nanoparticles.[259] The fact that the multilayers consisting of two oppositely charged nanoparticles of similar sizes (i.e., 16.2 nm AP-SiO_2/15.4 nm SiO_2 multilayers) have porosity of ca. 0.45 indicate that the packing density of these nanoparticles via LbL process is well below the maximum packing (i.e., hexagonal close packing) density of equally sized spheres, which would result in the porosity of 0.26.[272] The refractive index values of the constituent SiO_2 nanoparticles in all three cases examined here were determined to be ca. 1.46, which is consistent with the reported values for bulk SiO_2.[273] The fact that the refractive indices of silica nanoparticles from the three systems do not differ indicates that the variations observed in the effective refractive indices of three systems is due entirely to differences in the packing of nanoparticles. This result demonstrates that it is possible to vary, albeit by a small extent, the porosity of all-nanoparticle thin films by changing the sizes of the selected nanoparticle.

Table 8.1. Some physical properties of AP-SiO_2/SiO_2 multilayers as determined via the ellipsometry method.

Size of negatively charged SiO_2	8.6 nm	15.4 nm	24.2 nm
Assembly pH	5.0	4.5	3.0
Porosity	0.42 ± 0.02	0.45 ± 0.03	0.49 ± 0.03
Effective refractive index at 633 nm	1.26 ± 0.01	1.25 ± 0.02	1.22 ± 0.01
Average bilayer thickness (nm)	14.0	15.2	27.4
Refractive index of nanoparticles	1.46 ± 0.01	1.46 ± 0.01	1.45 ± 0.01

8.4 Conclusion

In summary, it was demonstrated that multilayers comprising oppositely charged silica nanoparticles can be assembled using the LbL technique. The effect of size of nanoparticles on multilayer structure was studied by depositing negatively charged silica nanoparticles of three different sizes paired with one type of positively charged silica nanoparticle. A narrow window of

assembly conditions existed for successful assembly, and the location of this processing window on the pH scale varied with the size of the nanoparticles. Atomic force microscopy study of multilayers in the early stages showed that unoptimized assembly conditions leads to the formation of domains of clustered nanoparticles instead of continuous layer of nanoparticles at each deposition cycle. The optimal assembly conditions which result in the maximum growth depended on the zeta-potential of the negatively charged silica nanoparticles. When $|z|$ of the negatively charged nanoparticles reached $0.7z_0$ (where z_0 is the value of the zeta-potential of the positively charged nanoparticles used in this study), the multilayers showed the maximum growth. This result provides some useful guidance in the search for the optimal conditions for LbL processing of all-nanoparticle thin films. The effect of the size of nanoparticles on film structure was also studied. While the average bilayer thickness of the all-silica nanoparticle multilayers exhibited a strong dependence on the size of nanoparticles, the difference in the porosity between different systems was rather small, ranging from 42 to 49 %. This study also has shown that by depositing one type of nanoparticle with opposite surface chemistry charge, one-component all-nanoparticle multilayers can be assembled successfully.

Chapter 9
Summary and Outlook

9.1 Summary

In this thesis, aqueous-based layer-by-layer (LbL) assembly was utilized as a tool for surface engineering of a variety of substrates including planar supports, spherical colloids and porous membranes. It was demonstrated that different types of functional (or multifunctional) coatings can be created via LbL deposition of pH-sensitive polyelectrolytes and nanoparticles.

The surface modification of colloidal particles is challenging due to the difficulty in achieving precise control over the surface chemistry involved without causing colloidal instability. To address this issue, LbL-assembled hydrogen-bonded multilayers were utilized to engineer the surface properties of colloidal particles. The multilayer-coated microparticles exhibited resistance toward mammalian cell adhesion with excellent long-term stability, which would favor the use of these coatings over the conventional bio-inert coatings such as poly(ethylene glycol). The multilayer coatings assembled on colloidal particles could also be used as templates for the *in situ* synthesis of metal nanoparticles. The concentration and size of nanoparticles grown within the coatings could be controlled by the number of loading and reduction cycles. This method provides a general approach to create nanocomposite microcapsules that contain various types of nanoparticles including magnetic, catalytic and semiconductor nanoparticles. By creating silver nanoparticle-loaded multilayer coatings on magnetic microspheres, antibacterial agents that can be delivered to specific locations using magnetic fields could be prepared. Although not mentioned in this thesis, asymmetric functionalization of colloidal particles was also achieved using the LbL assembly and polymer-on-polymer stamping techniques. These asymmetric structures (also known as Janus particles) will

enable the assembly of complex suprastructures that may find applications in fields such as photonics and biomedical engineering.

In the second part of the thesis, the layer-by-layer assembly was further extended to functionalize the surfaces of track-etched polycarbonate (TEPC) membranes to create stimuli responsive membranes and magnetic nanotubes. Multilayers that exhibit discontinuous swelling transition as a function of solution pH were coated in the pores of TEPC membranes to create pH-responsive membranes. The multilayer-modified membranes exhibited hysteretic gating behavior; i.e., these membranes show a large discontinuous and reversible transition in the trans-membrane flux as a function of solution pH. The hysteretic gating property of the multilayer-modified TEPC membrane was utilized to achieve either a "closed" or "open" state at a single pH condition. The degree of swelling of the pore-confined multilayers as estimated by simple models was significantly smaller than that of the multilayers on planar substrates under the same conditions. Suppression of the swelling of multilayers in the confined geometry is likely due to the stress formation in the multilayer-liquid interface in the cylindrical pores of TEPC. While it has been shown that stimuli responsive membranes can be fabricated using different approaches, this work reports, for the first time, the concept of hysteretic gating, which would be extremely important for the filtration of pH sensitive materials such as proteins and nanoparticles.

PAH/PSS multilayer coated TEPC membranes were further modified with additional layers of iron oxide nanoparticles and PAH to create heterostructured magnetic tubes with sub-micron dimensions. The magnetic nanotubes could be isolated from the template (i.e., TEPC membranes) by dissolving the membranes in an organic solvent. The magnetic nanotubes could be successfully used to separate (or remove) a high concentration of dye molecules from solution by activating the nanotubes in acidic solution. Also the nanotubes could be utilized as delivery vehicles of anionic molecules including pharmaceuticals. The combination of the template method and LbL assembly of

polyelectrolytes and nanoparticles allowed the formation of multifunctional magnetic colloidal structure, which was not possible using conventional LbL assembly onto colloidal particles, and enabled the fabrication of multifunctional colloidal structures.

Although the layer-by-layer assembly research has experienced a rapid growth, the possibility of creating multilayers from two oppositely charged nanoparticles without any organic processing agents has not been heavily exploited. Ironically, the very first report of multilayer assembly via LbL technique involved the creation of multilayers of oppositely charged colloidal particles. In the last part of the thesis, it was shown that all-nanoparticle thin film coatings via the assembly of two oppositely charged nanoparticles is not only possible but can also lead to a number of potentially useful functionalities. A self-cleaning anti-reflection (AR) coating with anti-fogging properties has been fabricated using the layer-by-layer deposition of positively charged titanium oxide (TiO_2) and negatively charged silicon dioxide (SiO_2) nanoparticles. The reflection of light by glass ($8 \sim 9\%$ with untreated glass) can be suppressed to achieve over 99% transmission in the visible region. These coatings are also superhydrophilic due to the presence of nanopores. The superhydrophilic nature of the coatings prevents formation of light scattering condensed water droplets on glass surfaces and results in anti-fogging properties. In addition, these coatings can "self-clean" or oxidize organic contaminants under UV irradiation.

The fundamental issues involved in the LbL assembly of oppositely charged nanoparticles were also investigated. Specifically, the dependence of multilayer (made from 7 nm TiO_2 and 22 nm SiO_2 nanoparticles) growth behavior and structure on assembly conditions (i.e., pH of each nanoparticle suspension) was studied. The growth behavior as represented by the average bilayer thickness of multilayers was stongly influenced by the assembly conditions. Average bilayer thickness varied from 2 to 30 nm depending on the pH condition of nanoparticle suspensions. It was found that a narrow window of processing conditions exists and that outside this window of opportunity very little

film growth was observed. Zeta-potential measurements of polystyrene microspheres coated with TiO_2/SiO_2 nanoparticle multilayers indicated that incomplete charge reversal after the deposition of nanoparticles leads to a very small thickness increase at each adsorption step, whereas complete charge reversal results in significantly larger thickness increments. Other characteristics (e.g., average bilayer thickness, refractive index, chemical composition, and porosity) of TiO_2/SiO_2 nanoparticle multilayer thin films could be controlled by varying the assembly conditions (i.e., pH of each nanoparticle suspension). In Chapter 8, the growth behavior of all-silica nanoparticle multilayers was studied. One type of positively charged silica nanoparticle was paired with three different types of negatively charged silica nanoparticles. The results indicated that it is the zeta-potential of the nanoparticles, rather than the absolute value of pH units, that determines the growth behavior of these all-nanoparticle multilayers. Also the results obtained in Chapter 8 indicated that there may exist a universal trend in the effect of surface charge density on the growth of multilayers. These fundamental studies will provide an important blueprint for the fabrication of all-nanoparticle multilayers and also enable the formation of different multifunctional nanoparticle thin films by incorporating a variety of nanoparticles.

In summary, my thesis has demonstrated that functional coatings can be created using the molecular-level layer-by-layer assembly of pH-sensitive polymers and nanoparticles. A number of new systems have been developed that led to novel applications in the areas of biomaterials, separation, drug delivery, and optics. Also the results have provided valuable insights into a number of important fundamental issues in polymer and colloid/interface science.

9.2 Outlook

The first part of this thesis has demonstrated that multilayer coatings containing a partially ionized weak polyacid can be created on colloidal particles. Others also have shown that, by using

different means and systems, weak polyelectrolyte multilayers can be assembled on colloidal particles. Formation of these types of weak polyelectrolyte multilayers will enable creating coatings with functionalities that are not readily achievable by other means. By applying coatings that can undergo porosity transition in response to certain stimuli, for example, it will be possible to trigger the release of core materials which can range from pharmaceutical ingredients to large molecular weight biomolecules including DNA and proteins. However, one of the major obstacles to real application of layer-by-layer deposition to engineer particle surface is the fact that LbL assembly has to be performed manually. Thus, I believe one of the most important issues that need to be addressed is the development of a means to automate the LbL process for particles. At the moment, only a few ml of suspension, the particle concentration of which is on the order of 1 vol. %, can be processed at a time, and it takes anywhere between 20 to 60 min to deposit just a single layer. As automatic dipping machines have enabled creation of thick multilayers with a wide range of properties, automation of particle coatings will lead to formation of a number of potentially useful coatings by allowing a rapid scanning through different assembly parameters. To achieve automation and scale-up of the process, some of the conventional chemical engineering process units may be utilized. For example, by modifying a fluidized bed type reactor, it may be possible to sequentially introduce solutions containing oppositely charged species to create multilayer coatings on colloidal particles.

This thesis also has shown that layer-by-layer deposition of multilayers is a versatile means to engineer surface properties of non-planar supports including spherical colloids and porous membranes. Recently, this technique has been extended to create functional coatings on woven/non-woven fibers. By creating silica nanoparticle-containing multilayer coatings on fibers, a number of silane based chemistry can be easily applied to the fiber surface. For example, woven fibers of poly(ethylene terephthalate) (PET) could be readily modified to exhibit either superhydrophilicity or superhydrophobicity by using such an approach. Taking advantage of the rich library of silane

compounds, it will be possible to engineer the surface properties of fibers and textiles suitable for specific applications.

In collaboration with Professor Jongyoon Han's group in the Electrical Engineering and Computer Science Department at MIT, I have shown that the surface of nanofluidic channels can be coated with uniform films of polyelectrolyte multilayers. Figure 9.1 shows that 100 nm thick multilayers consisting of PSS and PAH conformally coat nanofluidic structures without causing any clogging of the channels. The surface modification of micro-/nanofluidic channels is, by no means, a trivial matter and poses a significant challenge. In this respect, layer-by-layer deposition of multilayers provides a versatile means to create functional surfaces in these microscopic structures. A number of potentially useful micro-/nanofluidic systems can be developed by creating multilayer systems that contain partially ionized weak polyelectrolyte. For example, by creating the multilayer system that undergoes swelling transition (described in Chapter 4), it will be possible to gate and regulate the flow of liquids in the nanofluidic channels. Also, by changing the surface charge density and roughness of nanofluidic channels, it will be possible to study the diffusion characteristics of ionic species including ions and charged biomacromolecules (e.g., proteins, DNA, etc.) in these confinement environments.

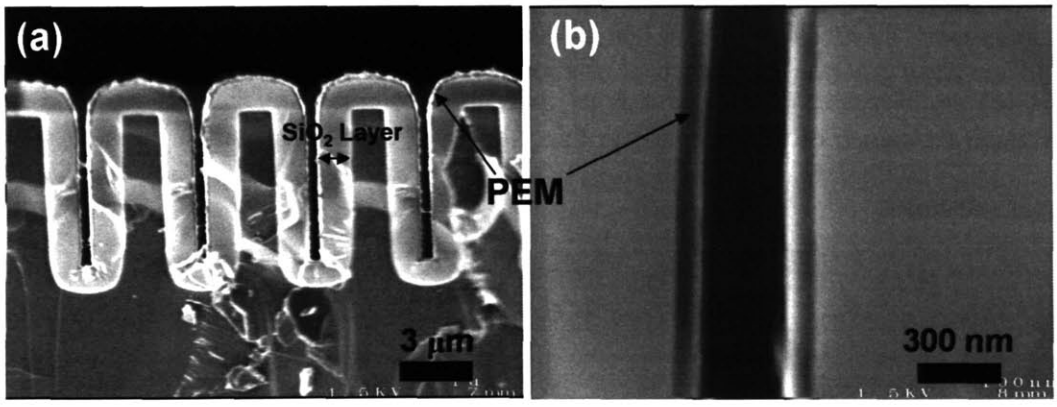

Figure 9.1. Cross-section SEM images of nanofluidic channels coated with 60 bilayers of (PAH/PSS) multilayers. PEM denotes polyelectrolyte multilayer.

In the last part of this thesis, it was demonstrated that all-nanoparticle multilayer thin films provide a simple yet powerful means to prepare thin films of multiple types of nanoparticles. Despite Iler's initial report of preparing multilayers of oppositely charged nanoparticles in 1966[18], research activities in the field have mainly focused on creating polymer-containing multilayer thin films. Among many reasons for such neglect of the all-nanoparticle multilayer systems, the most important reason likely is the fact that there is a very narrow processing window where all-nanoparticle multilayers can be assembled in a true layer-by-layer manner. Therefore, it may have been very difficult to make multilayers without any prior knowledge about the assembly behavior of oppositely charged nanoparticles. To exploit the full potential of assembling all-nanoparticle thin films, it is essential to understand in detail the effects of various assembly parameters on the formation of all-nanoparticle multilayers. Characterization tools including *in situ* atomic force microscopy, cross-sectional transmission electron microscopy, scattering and quartz crystal microbalance will provide important insights into the structure and dynamics of these all-nanoparticle thin films during and after assembly.

For practical application of all-nanoparticle thin films, mechanical robustness of the films is crucial. The mechanical stability of the multilayers studied in this thesis could be easily improved by a high temperature calcination; however this process is limited to materials that can withstand such a high temperature process. Development of a low temperature process that can improve the adhesion and scratch resistance of all-nanoparticle thin films will enable application of these structures on polymer substrates.

Appendix A

Supporting Information for Chapter 4

Two-region flow model. The two-region flow (TRF) model divides the flow field within the multilayer coated cylindrical pores into two distinct regions (Figure A). In region A, there is fully developed laminar flow through the physically open space, whereas in region B water flow through the hydrated multilayers is hindered by the presence of the polymer matrix. The velocity profile in region A cab be described by the equation of motion,

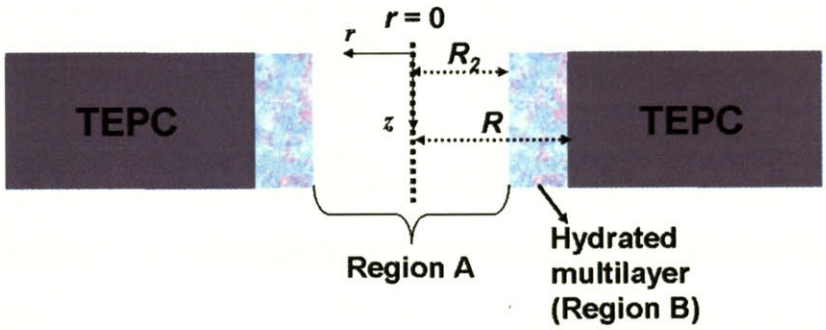

Figure A.1. Schematic illustration of two-region flow model in the cylindrical pores of multilayer modified TEPC membranes.

$$\frac{1}{r}\frac{d}{dr}\left(r\frac{du^A}{dr}\right)-\frac{1}{\eta}\frac{dP}{dz}=0 \qquad \text{(A.1)}$$

where, u^A is the velocity of water in the central region (multilayer-free region), η is the viscosity of water, P is the hydraulic pressure, and z and r are the axial and radial variable of the cylindrical pores. Transport of water through the hydrated multilayer (region B) can be described by the Debye-Brinkman equation,

$$\frac{1}{r}\frac{d}{dr}\left(r\frac{du^B}{dr}\right)-\frac{u^B}{\kappa}-\frac{1}{\eta}\frac{dP}{dz}=0 \qquad \text{(A.2)}$$

where, u^B is the velocity of water in region B and κ is the solvent-specific hydraulic permeability coefficient associated with the multilayer region. The Debye-Brinkman (also known as the Brinkman equation) equation has been used to model flow of water through capillary channels filled with polymer gels by others.[274-276] Equation (A.1) and (A.2) are solved simultaneously to obtain velocity profiles in the two regions with the following boundary conditions

$$\begin{aligned} & u^B(R) = 0 \\ & \frac{du^A}{dr}(0) = 0 \\ & u^A(R_2) = u^B(R_2) \\ & \frac{du^A}{dr}(R_2) = \frac{du^B}{dr}(R_2) \end{aligned} \tag{A.3}$$

where, R is the radius of unmodified cylindrical pores of TEPC membranes and R_2 is the constricted radius after multilayer have been swollen (or hydrated). Permeability coefficient (κ) can be estimated from the following empirical relationship, [164,165]

$$\kappa = c\left(\frac{1-\phi}{\phi}\right) \tag{A.4}$$

where, c is an empirical constant determined from polymer sedimentation data for each polymer-solvent pair and ϕ is the polymer volume fraction in the region B. Note that this relation has correct limiting behavior, both at ϕ = 0 or 1, that is, when ϕ = 0, equation (A.2) reverts back to equation (A.1) meaning no hindrance to flow is present. When ϕ = 1, the second term in the equation (A.2) assumes the largest value representing the greatest hindrance to the flow of water due to the presence of polymer matrix. While the value of c for the multilayer system (PAH/PSS multilayer-water) is unknown, a previous study by Mijnlieff and Wiegel has shown that c is of the order of 1 nm^2.[277,278] Since the goal in this study is to qualitatively show the trend in swelling behavior of

multilayers from flux experiments on the assumption that there is some penetration of water through the hydrated multilayers rather than to make precise predictions, the value of c will be assumed to be 1 nm^2. For comparison, the values of c for poly(vinylpyrrolidone) and poly((L-glutamic acid)) brushes, which are both water soluble polymers, are reported to be approximately 0.6 nm^2 and 4 nm^2, respectively. [164,165] The polymer volume fraction (ϕ) also is assumed to be uniform throughout the Region B. Polymer volume fraction is defined as

$$\phi = \frac{R^2 - R_1^{\,2}}{R^2 - R_2^{\,2}} \tag{A.5}$$

where R_1 is the radius of multilayer coated pores in dry state (determined from SEM).

Velocity profiles obtained from the above equations can be used to calculate flux using the following equation:

$$J = \left(\frac{\varepsilon}{\tau}\right)\frac{\int_0^{R_2} u^A(r)rdr + \int_{R_2}^{R} u^B(r)rdr}{\int_0^R rdr} \tag{A.6}$$

where, ε ($= n\pi(D/2)^2$) is the porosity of the TEPC membrane and τ ($= \frac{L}{L_m}$ where L_m is the thickness of the membrane) is the tortuosity of the membrane. The value for ε/τ can be estimated from Hagen-Poiseuille equation (A.7) by measuring the trans-membrane flux of bare membrane.

$$J = \frac{n\pi(D/2)^4 \Delta P}{8\eta L} = \left(\frac{\varepsilon}{\tau}\right)\frac{(D/2)^2 \Delta P}{8\eta L_m} \tag{A.7}$$

It is possible to use equation (A.6) in connection with equations (A.1) and (A.2) to numerically calculate the pore radii from experimental flux values.

Table A.1 summarizes the parameters used in the TRF model to estimate the pore radius from experimental flux values.

Table A.1. Parameters used in the two-region flow model calculation.

Nominal pore diameter of TEPC membrane	R^a (nm)	$R_1{}^b$ (nm)	$L_m{}^c$ (μm)	ΔP (psi)	ε/τ	Maximum % swelling attainable
400 nm	187.5	157.5	10	10	0.23[d]	240
800 nm	400	300	9	20	0.15[e]	129

[a, b] Determined using SEM. [c] Value provided by the supplier of the TEPC membranes. [d] Determined using Eq. A.7. [e] Value obtained using Eq. A.7 led to unreasonable value of R_2 (with the value obtained with Eq. A.7, the radius of the pores (R_2) is estimated to be larger than 300 nm, which is contradictory to the SEM observation; thus the smallest ε/τ that would result in reasonable value of R_2 was used)[j], thus this value was estimated from the SEM observation.

Definition of percent (%) swelling. The percent (%) swelling of multilayers is defined as $\frac{V_f - V_0}{V_0} \times 100\,\%$, where V_f = final volume of multilayers after swelling and V_0 = volume of dry multilayers. The % swelling of multilayers on planar substrates (Figure A.(a)) and in cylindrical pores (Figure A.(b)) are defined as follows:

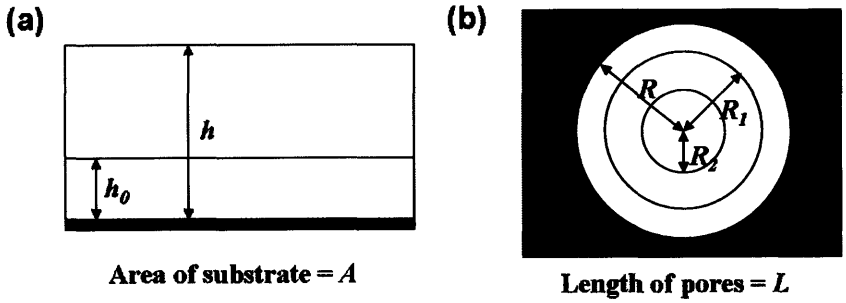

Figure A.2. Illustration of multilayers swelling in (a) planar thin films and (b) in cylindrical pores.

[j] As stated in Chapter 4, the Hagen-Poiseulle equation is inadequate to describe the flux across TEPC membranes with 800 nm pores; therefore, ε/τ for this particular membrane was estimated from the observation based on SEM.

For planar multilayer thin films (Figure A.(a)): % swelling = $\frac{(h-h_0)A}{h_0 A}\times 100 = \frac{h-h_0}{h_0}\times 100$ (where h_0 = thickness of as-prepared film in dry state and h = thickness of swollen thin films determined by in-situ ellipsometry)

For multilayers in cylindrical pores (Figure A.(b)): % swelling = $\frac{\pi L\left(R_1^{\,2}-R_2^{\,2}\right)}{\pi L\left(R^2-R_1^{\,2}\right)}\times 100 = \frac{\left(R_1^{\,2}-R_2^{\,2}\right)}{\left(R^2-R_1^{\,2}\right)}\times 100$ (where R is the radius of unmodified pore, R_1 is the radius of pore after multilayer coating in dry state, and R_2 is the radius of pore after multilayer is swollen)

The % swelling can be converted to a swelling ratio ($q = \frac{V_f}{V_0}$) by the following relation:

$$\text{Swelling ratio } (q) = \frac{\%\,\text{swelling}}{100} + 1 \qquad \text{(A.8)}$$

Appendix B
MATLAB® Source Code

This appendix contains the MATLAB® source code used for the estimation of pore radius (R_2; see Appendix A for notations) using Two-Region Flow (TRF) model descried in Appendix A. The code consists of seven separate Matlab (m) files. All of these m files need to be placed under one working directory (e.g., c:\program files\matlab704\work\daeyeon\). Table B.1 summarizes the constants that must be specified in each m file before executing the code.

Table B.1. Constants in Matlab code for TRF model calculation.

m file	Constants [units]
daeyeonINT.m	None
daeyeonFCT.m	None
daeyeonODE.m	h0 (thickness of multilayer) [nm], R (radius of pores) [nm], dPdx (pressure drop) [cP/(nm·s)]
daeyeonRES.m	dPdx [cP/(nm·s)]
DYL.m	None
findDYL.m	R [nm], eps_over_tau (ε/τ)
goDYL.m	None

The code can be used to estimate R_2 (radius of physically open region), fractional flux, and velocity profiles.

Estimation of R_2.

1. Input the experimental flux values and estimates. This process can be done by entering "Input=[enter experiemtnal flux values here]" and "guess=[enter estimates here]"
2. R_2 is determined by entering "[Rcalc, FLUXcalc]=goDYL(input, guess)"
3. To stop the calculation press ctrl + C

Estimation of fractional flux and plotting velocity profile for predetermined R_2.

1. To generate no plot, velocity profile from r = 0 to R, and velocity profile from r = -R to R, change the value after "numside =" to 0, 1, and 2, respectively, in DYL.m.
2. To obtain ASCII data for velocity profile, remove "%" in front of r' and u' in DYL.m.
3. To calculate fractional flux (i.e., flux through open region/total flux (x_A) and flux through multilayers/total flux (x_B)), remove ";" at the end of the lines that start with xA and xB in findDYL.m
4. Run by entering "findDYL(R_2)"

The following are seven Matlab (m) files used for the estimation of R_2 (constants should be entered in place of §description§ as summarized in Table B.1):

daeyeonINT.m

```
function uinit = daeyeonINT(r)
uinit = [1.8 0];
```

daeyeonFCT.m

```
function value = daeyeonFCT(sol,x,n)
 temp = deval(sol,x);
 value = temp(n);
```

daeyeonODE.m

```
function dudr = daeyeonODE(r,u,Rprime)
c = 1;
h0 = §thickness of multilayer§;
R = §radius of pores§;
mu = 1;
dPdx = §pressure drop across membrane§; %dPdx in cP/(nm*s)

phi = (R^2-(R-h0)^2)/(R^2-Rprime^2);
K=c*(1-phi)/phi;
A=dPdx/mu; %A's units are 1/(nm*s)
%-----------------------------------
if r < Rprime,
   dudr = [u(2) -u(2)/r + A]';
else
   dudr = [u(2) u(1)/K - u(2)/r + A]';
end
```

daeyeonRES.m

```
function res = daeyeonRES(u0,uR,Rprime)
mu = 1;
dPdx = §pressure drop across membrane§; %dPdx in cP/(nm*s)
A = dPdx/mu;
res = [ u0(2)+A/2*.0001 uR(1)]';
```

DYL.m

```
function sol = DYL(Rprime)
numsides = 0; %plot no graph (0), a half graph (1), or a full graph (2)
R = §raidus of pores§;
solinit = bvpinit(linspace(.0001,R,20),@daeyeonINT);
sol = bvp4c(@daeyeonODE,@daeyeonRES,solinit,[],Rprime);
r=[.0001:.5:R];
u=deval(sol,r);
u=u(1,:);
%u is in nm/sec... convert to cm/sec:
u=u/10^7;
if numsides == 1
   figure('color', 'white');
   plot(r,u);
   xlabel('Channel radius (nm)');
   ylabel('Fluid velocity (cm/sec)');
else if numsides == 2
      r = horzcat(-fliplr(r),r(1),r);
      u = horzcat(fliplr(u),u(1),u);
      figure('color', 'white');
      plot(r,u);
      xlabel('Channel radius (nm)');
      ylabel('Fluid velocity (cm/sec)');
   end
end

%r';
%u';
```

findDYL.m

```
function FluxTotal = findDYL(Rprime)
R = §radius of pores§;
eps_over_tau = §ε/τ§;
sol = DYL(Rprime);
fluxA = eps_over_tau * quad(@(r)daeyeonFCT(sol,r,1)*r,.0001,Rprime,1e6)/(R^2/2)/10^7*60; %flux in
mL/min/cm^2
fluxB = eps_over_tau * quad(@(r)daeyeonFCT(sol,r,1)*r,Rprime,R,1e6)/(R^2/2)/10^7*60;
FluxTotal = fluxA + fluxB; %flux in mL/min/cm^2
xA = fluxA / FluxTotal;
xB = fluxB / FluxTotal;
```

goDYL.m

```
function [Rcalc FLUXcalc] = goDYL(input,guess)
len = length(input);
for I = 1:len,
   [answer1 answer2] = fzero(@(x)findDYL(x)-input(I),guess(I));
   Rcalc(I) = answer1;
   FLUXcalc(I) = answer2+input(I);
   disp(strcat('Step_',num2str(I),'_completed'))
end
Rcalc = Rcalc';
FLUXcalc = FLUXcalc';
```

References

1 Strafford, K.N., Datta, P.K. & Gray, J.S. *Surface Engineering Practice: Processes, Fundamentals and Applications in Corrosion and Wear*, Ellis Horwood, Chichester, 1990.

2 Jagur-Grodzinski, J. Polymers for tissue engineering, medical devices, and regenerative medicine. Concise general review of recent studies. *Polymers for Advanced Technologies* 2006, **17**(6), 395-418.

3 Gollwitzer, H., Ibrahim, K., Meyer, H., Mittelmeier, W., Busch, R. & Stemberger, A. Antibacterial poly(D,L-lactic acid) coating of medical implants using a biodegradable drug delivery technology. *Journal of Antimicrobial Chemotherapy* 2003, **51**(3), 585-591.

4 Sosa, S. Silica-based nanocomposite turns cotton into superhydrophobic fabric. *Mrs Bulletin* 2004, **29**(12), 910-910.

5 Schuyten, H.A., Reid, D.J., Weaver, J.W. & Frick, J.G. Imparting Water-Repellency to Textiles by Chemical Methods: A Review of the Literature. *Text. Res. J.* 1948, **18**, 490-503.

6 Schuyten, H.A., Reid, D.J., Weaver, J.W. & Frick, J.G. Imparting Water-Repellency to Textiles by Chemical Methods: A Review of the Literature. *Text. Res. J.* 1948, **18**, 396-415.

7 Gelinck, G.H., Huitema, H.E.A., Van Veenendaal, E. *et al.* Flexible active-matrix displays and shift registers based on solution-processed organic transistors. *Nature Materials* 2004, **3**(2), 106-110.

8 Rogers, J.A. & Bao, Z. Printed plastic electronics and paperlike displays. *Journal of Polymer Science Part a-Polymer Chemistry* 2002, **40**(20), 3327-3334.

9 Nolte, A.J., Rubner, M.F. & Cohen, R.E. Creating effective refractive index gradients within polyelectrolyte multilayer films: Molecularly assembled rugate filters. *Langmuir* 2004, **20**(8), 3304-3310.

10 Wang, T.C., Cohen, R.E. & Rubner, M.F. Metallodielectric photonic structures based on polyelectrolyte multilayers. *Advanced Materials* 2002, **14**(21), 1534-1537.

11 Zhai, L., Nolte, A.J., Cohen, R.E. & Rubner, M.F. pH-gated porosity transitions of polyelectrolyte multilayers in confined geometries and their application as tunable Bragg reflectors. *Macromolecules* 2004, **37**(16), 6113-6123.

12 Ulman, A. Formation and structure of self-assembled monolayers. *Chemical Reviews* 1996, **96**(4), 1533-1554.

13 Stafford, C.M., Harrison, C., Beers, K.L. *et al.* A buckling-based metrology for measuring the elastic moduli of polymeric thin films. *Nature Materials* 2004, **3**(8), 545-550.

14 Uyama, Y., Kato, K. & Ikada, Y. Surface modification of polymers by grafting. *Grafting/Characterization Techniques/Kinetic Modeling* 1998, **137**, 1-39.

15 Peterson, I.R. Langmuir-Blodgett-Films. *Journal of Physics D-Applied Physics* 1990, **23**(4), 379-395.

16 Decher, G. Fuzzy nanoassemblies: Toward layered polymeric multicomposites. *Science* 1997, **277**(5330), 1232-1237.

17 Decher, G. & Schlenoff, J.B. (eds.). *Multilayer Thin Films: Sequential Assembly of Nanocomposite Materials*, Wiley-VCH Verlag GmbH & Co., Weinheim, 2003.

18 Iler, R.K. Multilayers of Colloidal Particles. *J Colloid Interf Sci* 1966, **21**, 569-594.

19 Lvov, Y., Decher, G. & Sukhorukov, G. Assembly of Thin-Films by Means of Successive Deposition of Alternate Layers of DNA and Poly(Allylamine). *Macromolecules* 1993, **26**(20), 5396-5399.

20 Netz, R.R. & Joanny, J.F. Adsorption of semiflexible polyelectrolytes on charged planar surfaces: Charge compensation, charge reversal, and multilayer formation. *Macromolecules* 1999, **32**(26), 9013-9025.

21 Abu-Sharkh, B. Structure and mechanism of the deposition of multilayers of polyelectrolytes and nanoparticles. *Langmuir* 2006, **22**(7), 3028-3034.

22 Cho, J., Char, K., Hong, J.D. & Lee, K.B. Fabrication of highly ordered multilayer films using a spin self-assembly method. *Advanced Materials* 2001, **13**(14), 1076-1078.

23 Chiarelli, P.A., Johal, M.S., Casson, J.L., Roberts, J.B., Robinson, J.M. & Wang, H.L. Controlled fabrication of polyelectrolyte multilayer thin films using spin-assembly. *Advanced Materials* 2001, **13**(15), 1167-+.

24 Schlenoff, J.B., Dubas, S.T. & Farhat, T. Sprayed polyelectrolyte multilayers. *Langmuir* 2000, **16**(26), 9968-9969.

25 Izquierdo, A., Ono, S.S., Voegel, J.C., Schaaff, P. & Decher, G. Dipping versus spraying: Exploring the deposition conditions for speeding up layer-by-layer assembly. *Langmuir* 2005, **21**(16), 7558-7567.

26 Caruso, F., Caruso, R.A. & Mohwald, H. Nanoengineering of inorganic and hybrid hollow spheres by colloidal templating. *Science* 1998, **282**(5391), 1111-1114.

27 Donath, E., Sukhorukov, G.B., Caruso, F., Davis, S.A. & Mohwald, H. Novel hollow polymer shells by colloid-templated assembly of polyelectrolytes. *Angewandte Chemie-International Edition* 1998, **37**(16), 2202-2205.

28 Balachandra, A.M., Dai, J.H. & Bruening, M.L. Enhancing the anion-transport selectivity of multilayer polyelectrolyte membranes by templating with Cu2+. *Macromolecules* 2002, **35**(8), 3171-3178.

29 Ai, S.F., Lu, G., He, Q. & Li, J.B. Highly flexible polyelectrolyte nanotubes. *Journal of the American Chemical Society* 2003, **125**(37), 11140-11141.

30 Lee, D., Nolte, A.J., Kunz, A.L., Rubner, M.F. & Cohen, R.E. pH-induced hysteretic gating of track-etched polycarbonate membranes: Swelling/deswelling behavior of polyelectrolyte multilayers in confined geometry. *Journal of the American Chemical Society* 2006, **128**(26), 8521-8529.

31 Lee, S.B. & Martin, C.R. pH-switchable, ion-permselective gold nanotubule membrane based on chemisorbed cysteine. *Analytical Chemistry* 2001, **73**(4), 768-775.

32 Liang, Z.J., Susha, A.S., Yu, A.M. & Caruso, F. Nanotubes prepared by layer-by-layer coating of porous membrane templates. *Advanced Materials* 2003, **15**(21), 1849-1853.

33 Liu, Y.X., He, T. & Gao, C.Y. Layer-by-layer assembly to modify poly(ethylene terephthalate) fiber fabrics toward promoting its endothelial cells adhesion. *Tissue Engineering* 2006, **12**(4), 1067-1068.

34 Zheng, Z.Q., Lvov, Y.M. & Shutava, T. Layer-by-layer self-assembly modification for pulp fiber. *Abstracts of Papers of the American Chemical Society* 2005, **229**, U296-U296.

35 Krol, S., Diaspro, A., Magrassi, R. *et al.* Nanocapsules: Coating for living cells. *Ieee Transactions on Nanobioscience* 2004, **3**(1), 32-38.

36 Hillberg, A.L. & Tabrizian, M. Biorecognition through layer-by-layer polyelectrolyte assembly: In-situ hybridization on living cells. *Biomacromolecules* 2006, **7**(10), 2742-2750.

37 Netz, R.R. Charge regulation of weak polyelectrolytes at low- and high-dielectric-constant substrates. *Journal of Physics-Condensed Matter* 2003, **15**(1), S239-S244.

38 Mandel, M. Polyelectrolytes. In *Encyclopedia of Polymer Science and Engineering* (Ed. Kroschwitz, J.I.) John Wiley & Sons, New York, 1989. 739-829.

39 Choi, J. & Rubner, M.F. Influence of the degree of ionization on weak polyelectrolyte multilayer assembly. *Macromolecules* 2005, **38**(1), 116-124.

40 Shiratori, S.S. & Rubner, M.F. pH-dependent thickness behavior of sequentially adsorbed layers of weak polyelectrolytes. *Macromolecules* 2000, **33**(11), 4213-4219.

41 Yoo, D., Shiratori, S.S. & Rubner, M.F. Controlling bilayer composition and surface wettability of sequentially adsorbed multilayers of weak polyelectrolytes. *Macromolecules* 1998, **31**(13), 4309-4318.

42 Choi, J.Y. & Rubner, M.F. Selective adsorption of amphiphilic block copolymers on weak polyelectrolyte multilayers. *Journal of Macromolecular Science-Pure and Applied Chemistry* 2001, **38**(12), 1191-1206.

43 Yue, J. & Cohen, R.E. *Supramolecular Science* 1994, **1**, 117-122.

44 Wang, T.C., Rubner, M.F. & Cohen, R.E. Polyelectrolyte multilayer nanoreactors for preparing silver nanoparticle composites: Controlling metal concentration and nanoparticle size. *Langmuir* 2002, **18**(8), 3370-3375.

45 Joly, S., Kane, R., Radzilowski, L. *et al.* Multilayer nanoreactors for metallic and semiconducting particles. *Langmuir* 2000, **16**(3), 1354-1359.

46 Clay, R.T. & Cohen, R.E. Synthesis of metal nanoclusters within microphase-separated diblock copolymer: ICP-AES analysis of metal ion uptake. *Supramolecular Science* 1997, **4**(1-2), 113-119.

47 Mendelsohn, J.D., Yang, S.Y., Hiller, J., Hochbaum, A.I. & Rubner, M.F. Rational design of cytophilic and cytophobic polyelectrolyte multilayer thin films. *Biomacromolecules* 2003, **4**(1), 96-106.

48 Yang, S.Y., Mendelsohn, J.D. & Rubner, M.F. New class of ultrathin, highly cell-adhesion-resistant polyelectrolyte multilayers with micropatterning capabilities. *Biomacromolecules* 2003, **4**(4), 987-994.

49 Hiller, J., Mendelsohn, J.D. & Rubner, M.F. Reversibly erasable nanoporous anti-reflection coatings from polyelectrolyte multilayers. *Nature Materials* 2002, **1**(1), 59-63.

50 Hiller, J. & Rubner, M.F. Reversible molecular memory and pH-switchable swelling transitions in polyelectrolyte multilayers. *Macromolecules* 2003, **36**(11), 4078-4083.

51 Kotov, N.A., Dekany, I. & Fendler, J.H. Layer-by-Layer Self-Assembly of Polyelectrolyte-Semiconductor Nanoparticle Composite Films. *Journal of Physical Chemistry* 1995, **99**(35), 13065-13069.

52 Ostrander, J.W., Mamedov, A.A. & Kotov, N.A. Two modes of linear layer-by-layer growth of nanoparticle-polylectrolyte multilayers and different interactions in the layer-by-layer deposition. *Journal of the American Chemical Society* 2001, **123**(6), 1101-1110.

53 Lvov, Y., Ariga, K., Onda, M., Ichinose, I. & Kunitake, T. Alternate assembly of ordered multilayers of SiO2 and other nanoparticles and polyions. *Langmuir* 1997, **13**(23), 6195-6203.

54 Caruso, R.A., Susha, A. & Caruso, F. Multilayered titania, silica, and Laponite nanoparticle coatings on polystyrene colloidal templates and resulting inorganic hollow spheres. *Chemistry of Materials* 2001, **13**(2), 400-409.

55 Caruso, F., Spasova, M., Susha, A., Giersig, M. & Caruso, R.A. Magnetic nanocomposite particles and hollow spheres constructed by a sequential layering approach. *Chemistry of Materials* 2001, **13**(1), 109-116.

56 Guldi, D.M., Zilberman, I., Anderson, G., Kotov, N.A., Tagmatarchis, N. & Prato, M. Nanosized inorganic/organic composites for solar energy conversion. *Journal of Materials Chemistry* 2005, **15**(1), 114-118.

57 Liang, Z.Q., Dzienis, K.L., Xu, J. & Wang, Q. Covalent layer-by-layer assembly of conjugated polymers and CdSe nanoparticles: Multilayer structure and photovoltaic properties. *Advanced Functional Materials* 2006, **16**(4), 542-548.

58 Kommireddy, D.S., Patel, A.A., Shutava, T.G., Mills, D.K. & Lvov, Y.M. Layer-by-layer assembly of TiO2 nanoparticles for stable hydrophilic biocompatible coatings. *Journal of Nanoscience and Nanotechnology* 2005, **5**(7), 1081-1087.

59 Cebeci, F.C., Wu, Z.Z., Zhai, L., Cohen, R.E. & Rubner, M.F. Nanoporosity-driven superhydrophilicity: A means to create multifunctional antifogging coatings. *Langmuir* 2006, **22**(6), 2856-2862.

60 Decher, G. & Hong, J.D. Buildup of Ultrathin Multilayer Films by a Self-Assembly Process .1. Consecutive Adsorption of Anionic and Cationic Bipolar Amphiphiles on Charged Surfaces. *Makromolekulare Chemie-Macromolecular Symposia* 1991, **46**, 321-327.

61 Kato, N., Schuetz, P., Fery, A. & Caruso, F. Thin multilayer films of weak polyelectrolytes on colloid particles. *Macromolecules* 2002, **35**(26), 9780-9787.

62 McClements, D.J. Theoretical analysis of factors affecting the formation and stability of multilayered colloidal dispersions. *Langmuir* 2005, **21**(21), 9777-9785.

63 Schuetz, P. & Caruso, F. Copper-assisted weak polyelectrolyte multilayer formation on microspheres and subsequent film crosslinking. *Advanced Functional Materials* 2003, **13**(12), 929-937.

64 Sukhishvili, S.A. & Granick, S. Layered, erasable polymer multilayers formed by hydrogen-bonded sequential self-assembly. *Macromolecules* 2002, **35**(1), 301-310.

65 Yang, S.Y. & Rubner, M.F. Micropatterning of polymer thin films with pH-sensitive and cross-linkable hydrogen-bonded polyelectrolyte multilayers. *Journal of the American Chemical Society* 2002, **124**(10), 2100-2101.

66 Serizawa, T., Nanameki, K., Yamamoto, K. & Akashi, M. Thermoresponsive ultrathin hydrogels prepared by sequential chemical reactions. *Macromolecules* 2002, **35**(6), 2184-2189.

67 Richert, L., Boulmedais, F., Lavalle, P. *et al.* Improvement of stability and cell adhesion properties of polyelectrolyte multilayer films by chemical cross-linking. *Biomacromolecules* 2004, **5**(2), 284-294.

68 Mrksich, M., Chen, C.S., Xia, Y.N., Dike, L.E., Ingber, D.E. & Whitesides, G.M. Controlling cell attachment on contoured surfaces with self-assembled monolayers of alkanethiolates on gold. *Proceedings of the National Academy of Sciences of the United States of America* 1996, **93**(20), 10775-10778.

69 Crouzet, C., Decker, C. & Marchal, J. Characterization of Primary Reactions of Oxidative-Degradation in Course of Autoxidation of Poly(Oxyethlene)S at 25degreesc - Study in

Aqueous-Solution with Initiation by Irradiation of Solvent .8. Kinetic Studies at Ph between 1 and 1. *Makromolekulare Chemie-Macromolecular Chemistry and Physics* 1976, **177**(1), 145-157.

70 Kane, R.S., Cohen, R.E. & Silbey, R. Synthesis of PbS nanoclusters within block copolymer nanoreactors. *Chemistry of Materials* 1996, **8**(8), 1919-1924.

71 Kane, R.S., Cohen, R.E. & Silbey, R. Synthesis of doped ZnS nanoclusters within block copolymer nanoreactors. *Chemistry of Materials* 1999, **11**(1), 90-93.

72 Kerker, M. (ed.) *Colloid and Interface Science: Proceedings of International Conference on Colloids and Surfaces*, Academic Press, New York, 1976, 413.

73 Ohde, H., Hunt, F. & Wai, C.M. Synthesis of silver and copper nanoparticles in a water-in-supercritical-carbon dioxide microemulsion. *Chemistry of Materials* 2001, **13**(11), 4130-4135.

74 Kreibig, U. & Vollmer, M. *Optical Properties of Metal Clusters*, Springer-Verlag, New York, 1995.

75 Ohde, H., Wai, C.M., Kim, H., Kim, J. & Ohde, M. Hydrogenation of olefins in supercritical CO2 catalyzed by palladium nanoparticles in a water-in-CO2 microemulsion. *Journal of the American Chemical Society* 2002, **124**(17), 4540-4541.

76 Chen, S.W., Huang, K. & Stearns, J.A. Alkanethiolate-protected palladium nanoparticles. *Chemistry of Materials* 2000, **12**(2), 540-547.

77 Pavoor, P.V., Bellare, A., Strom, A., Yang, D. & Cohen, R.E. Mechanical Characterization of Polyelectrolyte Multilayers Using Quasi-Static Nanoindentation. *Macromolecules* 2004, **37**(13), 4865-4871.

78 Nolte, A.J., Rubner, M.F. & Cohen, R.E. Measuring the Young's modulus of polyelectrolyte multilayer films using buckling instabilities. *Abstracts of Papers of the American Chemical Society* 2005, **230**, U3524-U3525.

79 Kane, R.S., Cohen, R.E. & Silbey, R. Semiconductor nanocluster growth within polymer films. *Langmuir* 1999, **15**(1), 39-43.

80 Costerton, J.W., Stewart, P.S. & Greenberg, E.P. Bacterial biofilms: A common cause of persistent infections. *Science* 1999, **284**(5418), 1318-1322.

81 Keleher, J., Bashant, J., Heldt, N., Johnson, L. & Li, Y.Z. Photo-catalytic preparation of silver-coated TiO2 particles for antibacterial applications. *World Journal of Microbiology & Biotechnology* 2002, **18**(2), 133-139.

82 Kim, J.W., Lee, J.E., Kim, S.J. *et al.* Synthesis of silver/polymer colloidal composites from surface-functional porous polymer microspheres. *Polymer* 2004, **45**(14), 4741-4747.

83 Kawashita, M., Toda, S., Kim, H.M., Kokubo, T. & Masuda, N. Preparation of antibacterial silver-doped silica glass microspheres. *Journal of Biomedical Materials Research Part A* 2003, **66A**(2), 266-274.

84 Davies, P., Schurr, G.A., Meenan, P. *et al.* Engineered particle surfaces. *Advanced Materials* 1998, **10**(15), 1264-1270.

85 Hafeli, U., Schutt, W., Teller, J. & Zborowski, M. (eds.). *Scientific and Clinical Applications of Magnetic Carriers*, Plenum Press, New York, 1997.

86 Feng, Q.L., Wu, J., Chen, G.Q., Cui, F.Z., Kim, T.N. & Kim, J.O. A mechanistic study of the antibacterial effect of silver ions on Escherichia coli and Staphylococcus aureus. *Journal of Biomedical Materials Research* 2000, **52**(4), 662-668.

87 Sykes, G. *Disinfection and Sterilization*, Van Nostrand, Princeton, NJ, 1958.

88 Clement, J.L. & Jarrett, P.S. Antibacterial Silver. *Metal-based Drugs* 1994, **1**(5-6), 467.

89 Dowling, D.P., Donnelly, K., McConnell, M.L., Eloy, R. & Arnaud, M.P. Deposition of anti-bacterial silver coatings on polymeric substrates. *Thin Solid Films* 2001, **398**, 602-606.

90 Balogh, L., Swanson, D.R., Tomalia, D.A., Hagnauer, G.L. & McManus, A.T. Dendrimer-silver complexes and nanocomposites as antimicrobial agents. *Nano Letters* 2001, **1**(1), 18-21.

91 Kawashita, M., Tsuneyama, S., Miyaji, F., Kokubo, T., Kozuka, H. & Yamamoto, K. Antibacterial silver-containing silica glass prepared by sol-gel method. *Biomaterials* 2000, **21**(4), 393-398.

92 Jeon, H.J., Yi, S.C. & Oh, S.G. Preparation and antibacterial effects of Ag-SiO2 thin films by sol-gel method. *Biomaterials* 2003, **24**(27), 4921-4928.

93 Lee, D., Rubner, M.F. & Cohen, R.E. Formation of nanoparticle-loaded microcapsules based on hydrogen-bonded multilayers. *Chemistry of Materials* 2005, **17**(5), 1099-1105.

94 Dai, J.H. & Bruening, M.L. Catalytic nanoparticles formed by reduction of metal ions in multilayered polyelectrolyte films. *Nano Letters* 2002, **2**(5), 497-501.

95 Grunlan, J.C., Choi, J.K. & Lin, A. Antimicrobial Behavior of Polyelectrolyte Multilayer Films Containing Cetrimide and Silver. *Biomacromolecules* 2005, **6**(2), 1149-1153.

96 Barry, A.L. Procedure for Testing Antimicrobial Agents in Agar Media: Theoretical Considerations. In *Antibiotics in Laboratory Medicine* (Ed. Lorian, V.) Williams & Wilkins, Baltimore, 1986. 1-25.

97 Widder, K.J., Senyei, A.E. & Ranney, D.F. Magnetically responsive microspheres and other carriers for the biophysical targeting of antitumor agents. In *Advances in Pharmacology and*

Chemotherapy (Eds. Garattini, S., Goldin, A., Howking, F., Kopin, I.J. & Schnitzer, R.J.) Academic, New York, 1979.

98 Pankhurst, Q.A., Connolly, J., Jones, S.K. & Dobson, J. Applications of magnetic nanoparticles in biomedicine. *J Phys D: Appl Phys* 2003, **36**, R167-R181.

99 Morisada, S., Miyata, N. & Iwahori, K. Immunomagnetic separation of scum-forming bacteria using polyclonal antibody that recongnizes mycolic acids. *J Microbiol Methods* 2002, **51**(2), 141-148.

100 Yang, S.Y., Lee, D., Cohen, R.E. & Rubner, M.F. Bioinert Solution-Cross-Linked Hydrogen-Bonded Multilayers on Colloidal Particles. *Langmuir* 2004, **20**(14), 5978-5981.

101 Lavalle, P., Gergely, C., Cuisinier, F.J.G. *et al.* Comparison of the structure of polyelectrolyte multilayer films exhibiting a linear and an exponential growth regime: An in situ atomic force microscopy study. *Macromolecules* 2002, **35**(11), 4458-4465.

102 Ruths, J., Essler, F., Decher, G. & Riegler, H. Polyelectrolytes I: Polyanion/polycation multilayers at the air/monolayer/water interface as elements for quantitative polymer adsorption studies and preparation of hetero-superlattices on solid surfaces. *Langmuir* 2000, **16**(23), 8871-8878.

103 Crank, J. *The Mathematics of Diffusion*, Clarendon Press, Oxford, England, 1975.

104 Cooper, K.E. The Theory of Antibiotic Inhibition Zone. In *Analytical Microbiology*, Vol. 1 (Ed. Kavanagh, F.) Academic Press, New York, 1963. 1-86.

105 Cioffi, N., Torsi, L., Ditaranto, N. *et al.* Antifungal activity of polymer-based copper nanocomposite coatings. *Applied Physics Letters* 2004, **85**(12), 2417-2419.

106 Barton, A.J., Sagers, R.D. & Pitt, W.G. Measurement of bacterial growth rates on polymers. *Journal of Biomedical Materials Research* 1996, **32**(2), 271-278.

107 Kozlovskaya, V., Yakovlev, S., Libera, M. & Sukhishvili, S.A. Surface priming and the self-assembly of hydrogen-bonded multilayer capsules and films. *Macromolecules* 2005, **38**(11), 4828-4836.

108 Schierholz, J.M., Lucas, L.J., Rump, A. & Pulverer, G. Efficacy of sliver-coated medical devices. *Journal of Hospital Infection* 1998, **40**(4), 257-262.

109 Khopade, A.J., Arulsudar, N., Khopade, S.A. & Hartmann, J. Ultrathin antibiotic walled microcapsules. *Biomacromolecules* 2005, **6**(1), 229-234.

110 Zebli, B., Susha, A.S., Sukhorukov, G.B., Rogach, A.L. & Parak, W.J. Magnetic targeting and cellular uptake of polymer microcapsules simultaneously functionalized with magnetic and luminescent nanocrystals. *Langmuir* 2005, **21**(10), 4262-4265.

111 Dowling, D.P., Betts, A.J., Pope, C., McConnell, M.L., Eloy, R. & Arnaud, M.N. Anti-bacterial silver coatings exhibiting enhanced activity through the addition of platinum. *Surface & Coatings Technology* 2003, **163**, 637-640.

112 Zhang, H.J. & Ito, Y. pH control of transport through a porous membrane self-assembled with a poly(acrylic acid) loop brush. *Langmuir* 2001, **17**(26), 8336-8340.

113 Ito, Y., Inaba, M., Chung, D.J. & Imanishi, Y. Control of Water Permeation by Ph and Ionic-Strength through a Porous Membrane Having Poly(Carboxylic Acid) Surface-Grafted. *Macromolecules* 1992, **25**(26), 7313-7316.

114 Ito, Y., Nishi, S., Park, Y.S. & Imanishi, Y. Oxidoreduction-sensitive control of water permeation through a polymer brushes-grafted porous membrane. *Macromolecules* 1997, **30**(19), 5856-5859.

115 Ito, Y., Park, Y.S. & Imanishi, Y. Visualization of critical pH-controlled gating of a porous membrane grafted with polyelectrolyte brushes. *Journal of the American Chemical Society* 1997, **119**(11), 2739-2740.

116 Ito, Y., Park, Y.S. & Imanishi, Y. Imaging of a pH-sensitive polymer brush on a porous membrane using atomic force microscopy in aqueous solution. *Macromolecular Rapid Communications* 1997, **18**(3), 221-224.

117 Ito, Y., Ochiai, Y., Park, Y.S. & Imanishi, Y. pH-sensitive gating by conformational change of a polypeptide brush grafted onto a porous polymer membrane. *Journal of the American Chemical Society* 1997, **119**(7), 1619-1623.

118 Ito, Y. Signal-responsive gating by a polyelectrolyte pelage on a nanoporous membrane. *Nanotechnology* 1998, **9**(3), 205-207.

119 Ito, T., Hioki, T., Yamaguchi, T., Shinbo, T., Nakao, S. & Kimura, S. Development of a molecular recognition ion gating membrane and estimation of its pore size control. *Journal of the American Chemical Society* 2002, **124**(26), 7840-7846.

120 Ito, Y., Kotera, S., Inaba, M., Kono, K. & Imanishi, Y. Control of Pore-Size of Polycarbonate Membrane with Straight Pores by Poly(Acrylic Acid) Grafts. *Polymer* 1990, **31**(11), 2157-2161.

121 Okahata, Y., Ozaki, K. & Seki, T. Ph-Sensitive Permeability Control of Polymer-Grafted Nylon Capsule Membranes. *Journal of the Chemical Society-Chemical Communications* 1984, (8), 519-521.

122 Mika, A.M., Childs, R.F. & Dickson, J.M. Chemical valves based on poly(4-vinylpyridine)-filled microporous membranes. *Journal of Membrane Science* 1999, **153**(1), 45-56.

123 Mika, A.M. & Childs, R.F. Acid/base properties of poly(4-vinylpyridine) anchored within microporous membranes. *Journal of Membrane Science* 1999, **152**(1), 129-140.

124 Li, Y., Chu, L.Y., Zhu, J.H., Wang, H.D., Xia, S.L. & Chen, W.M. Thermoresponsive gating characteristics of Poly(N-isopropylacrylamide)-grafted porous poly(vinylidene fluoride) membranes. *Industrial & Engineering Chemistry Research* 2004, **43**(11), 2643-2649.

125 Park, Y.S., Ito, Y. & Imanishi, Y. Permeation control through porous membranes immobilized with thermosensitive polymer. *Langmuir* 1998, **14**(4), 910-914.

126 Park, Y.S., Ito, Y. & Imanishi, Y. Photocontrolled gating by polymer brushes grafted on porous glass filter. *Macromolecules* 1998, **31**(8), 2606-2610.

127 Hester, J.F., Olugebefola, S.C. & Mayes, A.M. Preparation of pH-responsive polymer membranes by self-organization. *Journal of Membrane Science* 2002, **208**(1-2), 375-388.

128 Chu, L.Y., Li, Y., Zhu, J.H. & Chen, W.M. Negatively thermoresponsive membranes with functional gates driven by zipper-type hydrogen-bonding interactions. *Angewandte Chemie-International Edition* 2005, **44**(14), 2124-2127.

129 Iwata, H., Oodate, M., Uyama, Y., Amemiya, H. & Ikada, Y. Preparation of Temperature-Sensitive Membranes by Graft-Polymerization onto a Porous Membrane. *Journal of Membrane Science* 1991, **55**(1-2), 119-130.

130 Bhaskar, R.K., Sparer, R.V. & Himmelstein, K.J. Effect of an Applied Electric-Field on Liquid-Crystalline Membranes - Control of Permeability. *Journal of Membrane Science* 1985, **24**(1), 83-96.

131 Chu, L.Y., Yamaguchi, T. & Nakao, S. A molecular-recognition microcapsule for environmental stimuli-responsive controlled release. *Advanced Materials* 2002, **14**(5), 386-389.

132 Mika, A.M., Childs, R.F., Dickson, J.M., Mccarry, B.E. & Gagnon, D.R. A New Class of Polyelectrolyte-Filled Microfiltration Membranes with Environmentally Controlled Porosity. *Journal of Membrane Science* 1995, **108**(1-2), 37-56.

133 Kang, M.S. & Martin, C.R. Investigations of potential-dependent fluxes of ionic permeates in gold nanotubule membranes prepared via the template method. *Langmuir* 2001, **17**(9), 2753-2759.

134 Lee, S.B. & Martin, C.R. Electromodulated molecular transport in gold-nanotube membranes. *Journal of the American Chemical Society* 2002, **124**(40), 11850-11851.

135 Yang, A.S. & Honig, B. On the Ph-Dependence of Protein Stability. *Journal of Molecular Biology* 1993, **231**(2), 459-474.

136 Roux, S., Garcia, B., Bridot, J.L. *et al.* Synthesis, characterization of dihydrolipoic acid capped gold nanoparticles, and functionalization by the electroluminescent luminol. *Langmuir* 2005, **21**(6), 2526-2536.

137 Yu, A.M., Liang, Z.J. & Caruso, F. Enzyme multilayer-modified porous membranes as biocatalysts. *Chemistry of Materials* 2005, **17**(1), 171-175.

138 Hou, S.F., Wang, J.H. & Martin, C.R. Template-synthesized protein nanotubes. *Nano Letters* 2005, **5**(2), 231-234.

139 Hou, S.F., Wang, J.H. & Martin, C.R. Template-synthesized DNA nanotubes. *Journal of the American Chemical Society* 2005, **127**(24), 8586-8587.

140 Sukhishvili, S.A. Responsive polymer films and capsules via layer-by-layer assembly. *Current Opinion in Colloid & Interface Science* 2005, **10**(1-2), 37-44.

141 Itano, K., Choi, J.Y. & Rubner, M.F. Mechanism of the pH-induced discontinuous swelling/deswelling transitions of poly(allylamine hydrochloride)-containing polyelectrolyte multilayer films. *Macromolecules* 2005, **38**(8), 3450-3460.

142 Mendelsohn, J.D., Barrett, C.J., Chan, V.V., Pal, A.J., Mayes, A.M. & Rubner, M.F. Fabrication of microporous thin films from polyelectrolyte multilayers. *Langmuir* 2000, **16**(11), 5017-5023.

143 Antipov, A.A., Sukhorukov, G.B. & Mohwald, H. Influence of the ionic strength on the polyelectrolyte multilayers' permeability. *Langmuir* 2003, **19**(6), 2444-2448.

144 Mauser, T., Dejugnat, C. & Sukhorukov, G.B. Reversible pH-dependent properties of multilayer microcapsules made of weak polyelectrolytes. *Macromolecular Rapid Communications* 2004, **25**(20), 1781-1785.

145 Dejugnat, C. & Sukhorukov, G.B. PH-responsive properties of hollow polyelectrolyte microcapsules templated on various cores. *Langmuir* 2004, **20**(17), 7265-7269.

146 Quinn, J.F. & Caruso, F. Facile tailoring of film morphology and release properties using layer-by-layer assembly of thermoresponsive materials. *Langmuir* 2004, **20**(1), 20-22.

147 Kharlampieva, E., Kozlovskaya, V., Tyutina, J. & Sukhishvili, S.A. Hydrogen-bonded multilayers of thermoresponsive polymers. *Macromolecules* 2005, **38**(25), 10523-10531.

148 Bruening, M.L. & Sullivan, D.M. Enhancing the ion-transport selectivity of multilayer polyelectrolyte membranes. *Chemistry-a European Journal* 2002, **8**(17), 3833-3837.

149 Park, M.K., Deng, S.X. & Advincula, R.C. pH-sensitive bipolar ion-permselective ultrathin films. *Journal of the American Chemical Society* 2004, **126**(42), 13723-13731.

150 Rmaile, H.H., Farhat, T.R. & Schlenoff, J.B. H-P-gated permeability of variably charged species through polyelectrolyte multilayer membranes. *Journal of Physical Chemistry B* 2003, **107**(51), 14401-14406.

151 Dubas, S.T., Farhat, T.R. & Schlenoff, J.B. Multiple membranes from "true" polyelectrolyte multilayers. *Journal of the American Chemical Society* 2001, **123**(22), 5368-5369.

152 Hollman, A.M. & Bhattacharyya, D. Pore assembled multilayers of charged polypeptides in microporous membranes for ion separation. *Langmuir* 2004, **20**(13), 5418-5424.

153 Kurata, M. & Tsunashima, Y. Viscosity-Molecular Relationships and Unperturbed Dimensions of Linear Chain Molecules. In *Polymer Handbook* (Eds. Brandrup, J. & Immergut, E.H.) John Wiley and Sons, Inc., New York, 1989.

154 Nolte, A.J., Rubner, M.F. & Cohen, R.E. Determining the young's modulus of polyelectrolyte multilayer films via stress-induced mechanical buckling instabilities. *Macromolecules* 2005, **38**(13), 5367-5370.

155 Brunner, H., Vallant, T., Mayer, U. & Hoffmann, H. Formation of ultrathin films at the solid-liquid interface studied by in situ ellipsometry. *Journal of Colloid and Interface Science* 1999, **212**(2), 545-552.

156 Delcorte, A., Bertrand, P., Wischerhoff, E. & Laschewsky, A. Adsorption of polyelectrolyte multilayers on polymer surfaces. *Langmuir* 1997, **13**(19), 5125-5136.

157 Cong, R., Temyanko, E. & Russo, P.S. Diffusion of Labeled Polyelectrolyte Probes in Unlabeled Polyelectrolyte Matrix Solutions. *Macromolecules* 2005, **38**(26), 10627-10630.

158 Jiang, X. Ph. D., MIT 2002.

159 Denn, M.M. *Process fluid mechanics*, PTR Prentice Hall, Englewood Cliffs, NJ, 1980.

160 Smuleac, V., Butterfield, D.A. & Bhattacharyya, D. Permeability and separation characteristics of polypeptide-functionalized polycarbonate track-etched membranes. *Chemistry of Materials* 2004, **16**(14), 2762-2771.

161 Hou, Z.Z., Abbott, N.L. & Stroeve, P. Self-assembled monolayers on electroless gold impart pH-responsive transport of ions in porous membranes. *Langmuir* 2000, **16**(5), 2401-2404.

162 Kim, K.J. & Stevens, P.V. Hydraulic and surface characteristics of membranes with parallel cylindrical pores. *Journal of Membrane Science* 1997, **123**(2), 303-314.

163 Glinel, K., Prevot, M., Krustev, R., Sukhorukov, G.B., Jonas, A.M. & Mohwald, H. Control of the water permeability of polyelectrolyte multilayers by deposition of charged paraffin particles. *Langmuir* 2004, **20**(12), 4898-4902.

164 Castro, R.P., Monbouquette, H.G. & Cohen, Y. Shear-induced permeability changes in a polymer grafted silica membrane. *Journal of Membrane Science* 2000, **179**(1-2), 207-220.

165 Hollman, A.M., Scherrer, N.T., Cammers-Goodwin, A. & Bhattacharyya, D. Separation of dilute electrolytes in poly(amino acid) functionalized microporous membranes: model evaluation and experimental results. *Journal of Membrane Science* 2004, **239**(1), 65-79.

166 Nishizawa, M., Menon, V.P. & Martin, C.R. Metal Nanotubule Membranes with Electrochemically Switchable Ion-Transport Selectivity. *Science* 1995, **268**(5211), 700-702.

167 Mafe, S., Aguilella, V.M., Alcaraz, A., Cervera, J. & Ramirez, P. Modeling of ion transport in pH dependent fixed charge membranes with narrow pores. *Biophysical Journal* 2003, **84**(2), 95a-95a.

168 Ramirez, P., Mafe, S., Alcaraz, A. & Cervera, J. Modeling of pH-switchable ion transport and selectivity in nanopore membranes with fixed charges. *Journal of Physical Chemistry B* 2003, **107**(47), 13178-13187.

169 Beebe, D.J., Moore, J.S., Bauer, J.M. *et al.* Functional hydrogel structures for autonomous flow control inside microfluidic channels. *Nature* 2000, **404**(6778), 588-590.

170 Hiemenz, P.C. & Rajagopalan, R. *Principles of Colloid and Surface Chemistry*, Marcel Dekker, Inc., New York, 1997.

171 Gupta, A.K. & Gupta, M. Synthesis and surface engineering of iron oxide nanoparticles for biomedical applications. *Biomaterials* 2005, **26**(18), 3995-4021.

172 Thunemann, A.F., Schutt, D., Kaufner, L., Pison, U. & Mohwald, H. Maghemite nanoparticles protectively coated with poly(ethylene imine) and poly(ethylene oxide)-block-poly(glutamic acid). *Langmuir* 2006, **22**(5), 2351-2357.

173 Reiss, G., Brueckl, H., Huetten, A. *et al.* Magnetoresistive sensors and magnetic nanoparticles for biotechnology. *Journal of Materials Research* 2005, **20**(12), 3294-3302.

174 Singh, H., Laibinis, P.E. & Hatton, T.A. Synthesis of flexible magnetic nanowires of permanently linked core-shell magnetic beads tethered to a glass surface patterned by microcontact printing. *Nano Letters* 2005, **5**(11), 2149-2154.

175 Singh, H., Laibinis, P.E. & Hatton, T.A. Rigid, superparamagnetic chains of permanently linked beads coated with magnetic nanoparticles. Synthesis and rotational dynamics under applied magnetic fields. *Langmuir* 2005, **21**(24), 11500-11509.

176 Wirtz, D. & Fermigier, M. One-Dimensional Patterns and Wavelength Selection in Magnetic Fluids. *Physical Review Letters* 1994, **72**(14), 2294-2297.

177 Wirtz, D. & Fermigier, M. Periodic Structures and Substructures in Magnetic Suspensions. *Langmuir* 1995, **11**(2), 398-400.

178 Dimitrov, A.S., Takahashi, T., Furusawa, K. & Nagayama, K. Two-dimensional patterns of magnetic particles at air-water or glass-water interfaces induced by an external magnetic field: Experimental observation and dependencies. *Journal of Physical Chemistry* 1996, **100**(8), 3163-3168.

179 Takahashi, T., Dimitrov, A.S. & Nagayama, K. Two-dimensional patterns of magnetic particles at air-water or glass-water interfaces induced by an external magnetic field: Theory and simulation of the formation process. *Journal of Physical Chemistry* 1996, **100**(8), 3157-3162.

180 Prestvik, W.S., Berge, A., Mork, P.C., Stenstad, P.M. & Ugelstad, J. Preparation and application of monosized magnetic particles in selective cell separation. In *Scientific and Clinical Applications of Magnetic Carriers* (Eds. Hafeli, U., Schutt, W., Teller, J. & Zborowski, M.) Plenum Press, New York, 1997. 11-35.

181 Kim, B.S., Qiu, J.M., Wang, J.P. & Taton, T.A. Magnetomicelles: Composite nanostructures from magnetic nanoparticles and cross-linked amphiphilic block copolymers. *Nano Letters* 2005, **5**(10), 1987-1991.

182 Berret, J.F., Schonbeck, N., Gazeau, F. *et al.* Controlled clustering of superparamagnetic nanoparticles using block copolymers: Design of new contrast agents for magnetic resonance imaging. *Journal of the American Chemical Society* 2006, **128**(5), 1755-1761.

183 Kim, J., Lee, J.E., Lee, J. *et al.* Magnetic fluorescent delivery vehicle using uniform mesoporous silica spheres embedded with monodisperse magnetic and semiconductor nanocrystals. *Journal of the American Chemical Society* 2006, **128**(3), 688-689.

184 Lin, K.J., Chen, L.J., Prasad, M.R. & Cheng, C.Y. Core-shell synthesis of a novel, spherical, mesoporous silica/platinum nanocomposite: Pt/PVP@MCM-41. *Advanced Materials* 2004, **16**(20), 1845-+.

185 Shiho, H., Manabe, Y. & Kawahashi, N. Magnetic compounds as coatings on polymer particles and magnetic properties of the composite particles. *Journal of Materials Chemistry* 2000, **10**(2), 333-336.

186 Pich, A., Bhattacharya, S. & Adler, H.J.P. Composite magnetic particles: 1. Deposition of magnetite by heterocoagulation method. *Polymer* 2005, **46**(4), 1077-1086.

187 Voigt, A., Buske, N., Sukhorukov, G.B. *et al.* Novel polyelectrolyte multilayer micro- and nanocapsules as magnetic carriers. *Journal of Magnetism and Magnetic Materials* 2001, **225**(1-2), 59-66.

188 Lu, Z.H., Prouty, M.D., Guo, Z.H., Golub, V.O., Kumar, C.S.S.R. & Lvov, Y.M. Magnetic switch of permeability for polyelectrolyte microcapsules embedded with Co@Au nanoparticles. *Langmuir* 2005, **21**(5), 2042-2050.

189 Fang, M., Grant, P.S., McShane, M.J., Sukhorukov, G.B., Golub, V.O. & Lvov, Y.M. Magnetic bio/nanoreactor with multilayer shells of glucose oxidase and inorganic nanoparticles. *Langmuir* 2002, **18**(16), 6338-6344.

190 Liu, Z.Q., Zhang, D.H., Han, S. *et al.* Single crystalline magnetite nanotubes. *Journal of the American Chemical Society* 2005, **127**(1), 6-7.

191 Son, S.J., Reichel, J., He, B., Schuchman, M. & Lee, S.B. Magnetic nanotubes for magnetic-field-assisted bioseparation, biointeraction, and drug delivery. *Journal of the American Chemical Society* 2005, **127**(20), 7316-7317.

192 Nielsch, K., Castano, F.J., Matthias, S., Lee, W. & Ross, C.A. Synthesis of cobalt/polymer multilayer nanotubes. *Advanced Engineering Materials* 2005, **7**(4), 217-221.

193 Suber, L., Imperatori, P., Ausanio, G., Fabbri, F. & Hofmeister, H. Synthesis, morphology, and magnetic characterization of iron oxide nanowires and nanotubes. *Journal of Physical Chemistry B* 2005, **109**(15), 7103-7109.

194 Martin, C.R. Nanomaterials - a Membrane-Based Synthetic Approach. *Science* 1994, **266**(5193), 1961-1966.

195 Mitchell, D.T., Lee, S.B., Trofin, L. *et al.* Smart nanotubes for bioseparations and biocatalysis. *Journal of the American Chemical Society* 2002, **124**(40), 11864-11865.

196 Cepak, V.M. & Martin, C.R. Preparation of polymeric micro- and nanostructures using a template-based deposition method. *Chemistry of Materials* 1999, **11**(5), 1363-1367.

197 Caruso, F. (ed.) *Colloids and Colloid Assemblies*, WILEY-VCH Verlag GmbH & Co. KGaA, Weinheim, 2004.

198 Tieke, B., Toutianoush, A. & Jin, W.Q. Selective transport of ions and molecules across layer-by-layer assembled membranes of polyelectrolytes, p-sulfonato-calix[n]arenes and Prussian Blue-type complex salts. *Advances in Colloid and Interface Science* 2005, **116**(1-3), 121-131.

199 Dai, J.H., Baker, G.L. & Bruening, M.L. Use of porous membranes modified with polyelectrolyte multilayers as substrates for protein arrays with low nonspecific adsorption. *Analytical Chemistry* 2006, **78**(1), 135-140.

200 Chung, A.J. & Rubner, M.F. Methods of loading and releasing low molecular weight cationic molecules in weak polyelectrolyte multilayer films. *Langmuir* 2002, **18**(4), 1176-1183.

201 Zhai, L., Cebeci, F.C., Cohen, R.E. & Rubner, M.F. Stable superhydrophobic coatings from polyelectrolyte multilayers. *Nano Letters* 2004, **4**(7), 1349-1353.

202 Tian, Y., He, Q., Tao, C. & Li, J.B. Fabrication of fluorescent nanotubes basel on layer-by-layer assembly via covalent bond. *Langmuir* 2006, **22**(1), 360-362.

203 Kim, D.H., Karan, P., Goring, P. *et al.* Formation of dendrimer nanotubes by layer-by-layer deposition. *Small* 2005, **1**(1), 99-102.

204 Hou, S.F., Harrell, C.C., Trofin, L., Kohli, P. & Martin, C.R. Layer-by-layer nanotube template synthesis. *Journal of the American Chemical Society* 2004, **126**(18), 5674-5675.

205 Bognitzki, M., Hou, H.Q., Ishaque, M. *et al.* Polymer, metal, and hybrid nano- and mesotubes by coating degradable polymer template fibers (TUFT process). *Advanced Materials* 2000, **12**(9), 637-640.

206 Smith, R.N., McCormick, M., Barrett, C.J., Reven, L. & Spiess, H.W. NMR studies of PAH/PSS polyelectrolyte multilayers adsorbed onto silica. *Macromolecules* 2004, **37**(13), 4830-4838.

207 Sahoo, Y., Goodarzi, A., Swihart, M.T. *et al.* Aqueous ferrofluid of magnetite nanoparticles: Fluorescence labeling and magnetophoretic control. *Journal of Physical Chemistry B* 2005, **109**(9), 3879-3885.

208 Porrata, P., Goun, E. & Matsui, H. Size-controlled self-assembly of peptide nanotubes using polycarbonate membranes as templates. *Chemistry of Materials* 2002, **14**(10), 4378-4381.

209 Wirtz, M., Parker, M., Kobayashi, Y. & Martin, C.R. Template-synthesized nanotubes for chemical separations and analysis. *Chemistry-a European Journal* 2002, **8**(16), 3573-3578.

210 Hulteen, J.C. & Martin, C.R. A general template-based method for the preparation of nanomaterials. *Journal of Materials Chemistry* 1997, **7**(7), 1075-1087.

211 Illum, L., Jacobsen, L.O., Muller, R.H., Mak, E. & Davis, S.S. Surface Characteristics and the Interaction of Colloidal Particles with Mouse Peritoneal-Macrophages. *Biomaterials* 1987, **8**(2), 113-117.

212 Khopade, A.J. & Caruso, F. Surface-modification of polyelectrolyte multilayer-coated particles for biological applications. *Langmuir* 2003, **19**(15), 6219-6225.

213 Kim, A.J., Manoharan, V.N. & Crocker, J.C. Swelling-based method for preparing stable, functionalized polymer colloids. *Journal of the American Chemical Society* 2005, **127**(6), 1592-1593.

214 Nawar, S.S. & Doma, H.S. Removal of Dyes from Effluents Using Low-Cost Agricultural by-Products. *Science of the Total Environment* 1989, **79**(3), 271-279.

215 Lee, D., Cohen, R.E. & Rubner, M.F. Antibacterial properties of Ag nanoparticle loaded multilayers and formation of magnetically directed antibacterial microparticles. *Langmuir* 2005, **21**(21), 9651-9659.

216 Kolhe, P., Misra, E., Kannan, R.M., Kannan, S. & Lieh-Lai, M. Drug complexation, in vitro release and cellular entry of dendrimers and hyperbranched polymers. *International Journal of Pharmaceutics* 2003, **259**(1-2), 143-160.

217 Lenard, J., Rabson, A. & Vanderoef, R. Photodynamic Inactivation of Infectivity of Human-Immunodeficiency-Virus and Other Enveloped Viruses Using Hypericin and Rose-Bengal - Inhibition of Fusion and Syncytia Formation. *Proceedings of the National Academy of Sciences of the United States of America* 1993, **90**(1), 158-162.

218 Lenard, J., Rabson, A., Stevenson, N.R. & Vanderoef, R. Photodynamic Inactivation of Viral Fusion and Infectivity by Hypericin and Rose-Bengal - Effects on Hiv and Other Enveloped Viruses. *Journal of Cellular Biochemistry* 1993, 17-17.

219 Fendler, J.H. *Nanoparticles and Nanostructured Films: Preparation, Characterization and Applications*, Wiley-VCH Verlag GmbH, Weinheim, 1998.

220 Zhao, L.Y., Eldridge, K.R., Sukhija, K., Jalili, H., Heinig, N.F. & Leung, K.T. Electrodeposition of iron core-shell nanoparticles on a H-terminated Si(100) surface. *Applied Physics Letters* 2006, **88**(3), 033111.

221 Quinn, B.M., Dekker, C. & Lemay, S.G. Electrodeposition of noble metal nanoparticles on carbon nanotubes. *Journal of the American Chemical Society* 2005, **127**(17), 6146-6147.

222 Paul, S., Pearson, C., Molloy, A. *et al.* Langmuir-Blodgett film deposition of metallic nanoparticles and their application to electronic memory structures. *Nano Letters* 2003, **3**(4), 533-536.

223 Brust, M., Stuhr-Hansen, N., Norgaard, K., Christensen, J.B., Nielsen, L.K. & Bjornholm, T. Langmuir-Blodgett films of alkane chalcogenice (S, Se, Te) stabilized gold nanoparticles. *Nano Letters* 2001, **1**(4), 189-191.

224 Fan, H.Y., Wright, A., Gabaldon, J., Rodriguez, A., Brinker, C.J. & Jiang, Y.B. Three-dimensionally ordered gold nanocrystal/silica superlattice thin films synthesized via sol-gel self-assembly. *Advanced Functional Materials* 2006, **16**(7), 891-895.

225 Segalman, R.A. Patterning with block copolymer thin films. *Materials Science & Engineering R-Reports* 2005, **48**(6), 191-226.

226 Boontongkong, Y. & Cohen, R.E. Cavitated block copolymer micellar thin films: Lateral arrays of open nanoreactors. *Macromolecules* 2002, **35**(9), 3647-3652.

227 Krasteva, N., Besnard, I., Guse, B. *et al.* Self-assembled gold nanoparticle/dendrimer composite films for vapor sensing applications. *Nano Letters* 2002, **2**(5), 551-555.

228 Cant, N.E., Zhang, H.L., Critchley, K., Mykhalyk, T.A., Davies, G.R. & Evans, S.D. Fabrication and characterization of self-assembled nanoparticle/polyelectrolyte multilayer films. *Journal of Physical Chemistry B* 2003, **107**(49), 13557-13562.

229 Tian, S.J., Liu, J.Y., Zhu, T. & Knoll, W. Polyaniline/gold nanoparticle multilayer films: Assembly, properties, and biological applications. *Chemistry of Materials* 2004, **16**(21), 4103-4108.

230 Park, J., Fouche, L.D. & Hammond, P.T. Multicomponent patterning of layer-by-layer assembled polyelectrolyte/nanoparticle composite thin films with controlled alignment. *Advanced Materials* 2005, **17**(21), 2575-2579.

231 Gao, M.Y., Lesser, C., Kirstein, S., Mohwald, H., Rogach, A.L. & Weller, H. Electroluminescence of different colors from polycation/CdTe nanocrystal self-assembled films. *Journal of Applied Physics* 2000, **87**(5), 2297-2302.

232 Rouse, J.H. & Ferguson, G.S. Preparation of thin silica films with controlled thickness and tunable refractive index. *Journal of the American Chemical Society* 2003, **125**(50), 15529-15536.

233 Kumar, A., Mandale, A.B. & Sastry, M. Sequential electrostatic assembly of amine-derivatized gold and carboxylic acid-derivatized silver colloidal particles on glass substrates. *Langmuir* 2000, **16**(17), 6921-6926.

234 Hao, E.C., Yang, B., Zhang, J.H., Zhang, X., Sun, J.Q. & Shen, S.C. Assembly of alternating TiO2/CdS nanoparticle composite films. *Journal of Materials Chemistry* 1998, **8**(6), 1327-1328.

235 Brust, M., Bethell, D., Kiely, C.J. & Schiffrin, D.J. Self-assembled gold nanoparticle thin films with nonmetallic optical and electronic properties. *Langmuir* 1998, **14**(19), 5425-5429.

236 Taton, T.A., Mucic, R.C., Mirkin, C.A. & Letsinger, R.L. The DNA-mediated formation of supramolecular mono- and multilayered nanoparticle structures. *Journal of the American Chemical Society* 2000, **122**(26), 6305-6306.

237 Jeon, J., Panchagnula, V., Pan, J. & Dobrynin, A.V. Molecular dynamics simulations of mutilayer films of polyelectrolytes and nanoparticles. *Langmuir* 2006, **22**(10), 4629-4637.

238 Klar, T., Perner, M., Grosse, S., von Plessen, G., Spirkl, W. & Feldmann, J. Surface-plasmon resonances in single metallic nanoparticles. *Physical Review Letters* 1998, **80**(19), 4249-4252.

239 Biswas, R., Sigalas, M.M., Subramania, G., Soukoulis, C.M. & Ho, K.M. Photonic band gaps of porous solids. *Physical Review B* 2000, **61**(7), 4549-4553.

240 Wang, X.R., Masumoto, H., Someno, Y. & Hirai, T. Helicon plasma deposition of a TiO2/SiO2 multilayer optical filter with graded refractive index profiles. *Applied Physics Letters* 1998, **72**(25), 3264-3266.

241 Garcia-Santamaria, F., Miguez, H., Ibisate, M., Meseguer, F. & Lopez, C. Refractive index properties of calcined silica submicrometer spheres. *Langmuir* 2002, **18**(5), 1942-1944.

242 Tzitzinou, A., Keddie, J.L., Geurts, J.M., Peters, A.C.I.A. & Satguru, R. Film formation of latex blends with bimodal particle size distributions: Consideration of particle deformability and continuity of the dispersed phase. *Macromolecules* 2000, **33**(7), 2695-2708.

243 Henglein, A. Small-Particle Research - Physicochemical Properties of Extremely Small Colloidal Metal and Semiconductor Particles. *Chemical Reviews* 1989, **89**(8), 1861-1873.

244 Alivisatos, A.P. Semiconductor clusters, nanocrystals, and quantum dots. *Science* 1996, **271**(5251), 933-937.

245 Theiss, W. Optical properties of porous silicon. *Surface Science Reports* 1997, **29**(3-4), 95-192.

246 Wegner, K. & Pratsinis, S.E. Nozzle-quenching process for controlled flame synthesis of titania nanoparticles. *Aiche Journal* 2003, **49**(7), 1667-1675.

247 Wenzel, R.N. Resistance of Solid Surfaces to Wetting by Water. *Ind. Eng. Chem.* 1936, **28**(8), 988.

248 Wang, R., Hashimoto, K., Fujishima, A. *et al.* Light-induced amphiphilic surfaces. *Nature* 1997, **388**(6641), 431-432.

249 Stevens, N., Priest, C.I., Sedev, R. & Ralston, J. Wettability of photoresponsive titanium dioxide surfaces. *Langmuir* 2003, **19**(8), 3272-3275.

250 Zhang, X.T., Sato, O., Taguchi, M., Einaga, Y., Murakami, T. & Fujishima, A. Self-cleaning particle coating with antireflection properties. *Chemistry of Materials* 2005, **17**(3), 696-700.

251 Nakajima, A., Hashimoto, K., Watanabe, T., Takai, K., Yamauchi, G. & Fujishima, A. Transparent superhydrophobic thin films with self-cleaning properties. *Langmuir* 2000, **16**(17), 7044-7047.

252 Hoffmann, M.R., Martin, S.T., Choi, W.Y. & Bahnemann, D.W. Environmental Applications of Semiconductor Photocatalysis. *Chemical Reviews* 1995, **95**(1), 69-96.

253 Machida, M., Norimoto, K., Watanabe, T., Hashimoto, K. & Fujishima, A. The effect of SiO2 addition in super-hydrophilic property of TiO2 photocatalyst. *Journal of Materials Science* 1999, **34**(11), 2569-2574.

254 Asahi, R., Morikawa, T., Ohwaki, T., Aoki, K. & Taga, Y. Photocatalysts sensitive to visible light - Response. *Science* 2002, **295**(5555), 627-627.

255 Kim, S., Hwang, S.J. & Choi, W.Y. Visible light active platinum-ion-doped TiO2 photocatalyst. *Journal of Physical Chemistry B* 2005, **109**(51), 24260-24267.

256 Hyeon, T. Chemical synthesis of magnetic nanoparticles. *Chemical Communications* 2003, (8), 927-934.

257 Pellegrino, T., Kudera, S., Liedl, T., Javier, A.M., Manna, L. & Parak, W.J. On the development of colloidal nanoparticles towards multifunctional structures and their possible use for biological applications. *Small* 2005, **1**(1), 48-63.

258 Ai, H., Jones, S.A. & Lvov, Y.M. Biomedical applications of electrostatic layer-by-layer nano-assembly of polymers, enzymes, and nanoparticles. *Cell Biochemistry and Biophysics* 2003, **39**(1), 23-43.

259 Lee, D., Rubner, M.F. & Cohen, R.E. All-Nanoparticle Thin Film Coatings. *Nano Letters* 2006, **6**(10), 2305-2312.

260 Depasse, J. & Watillon, A. The Stability of Amorphous Colloidal Silica. *Journal of Colloid and Interface Science* 1970, **33**(3), 430-438.

261 Depasse, J. Simple experiments to emphasize the main characteristics of the coagulation of silica hydrosols by alkaline cations: Application to the analysis of the model of Colic et al. *Journal of Colloid and Interface Science* 1999, **220**(1), 174-176.

262 Binks, B.P. & Lumsdon, S.O. Stability of oil-in-water emulsions stabilised by silica particles. *Physical Chemistry Chemical Physics* 1999, **1**(12), 3007-3016.

263 Mandzy, N., Grulke, E. & Druffel, T. Breakage of TiO2 agglomerates in electrostatically stabilized aqueous dispersions. *Powder Technology* 2005, **160**(2), 121-126.

264 Tkachenko, N.H., Yaremko, Z.M., Bellmann, C. & Soltys, M.M. The influence of ionic and nonionic surfactants on aggregative stability and electrical surface properties of aqueous suspensions of titanium dioxide. *Journal of Colloid and Interface Science* 2006, **299**(2), 686-695.

265 Zhao, J.C., Hidaka, H., Takamura, A., Pelizzetti, E. & Serpone, N. Photodegradation of Surfactants .11. Zeta-Potential Measurements in the Photocatalytic Oxidation of Surfactants in Aqueous Tio2 Dispersions. *Langmuir* 1993, **9**(7), 1646-1650.

266 Hunter, R.J. *Zeta potential in colloid science: Principles and applications*, Academic Press, London, 1981.

267 Imae, T., Muto, K. & Ikeda, S. The Ph-Dependence of Dispersion of Tio2 Particles in Aqueous Surfactant Solutions. *Colloid and Polymer Science* 1991, **269**(1), 43-48.

268 Grishchenko, L.I., Medvedkova, N.G., Nazarov, V.V. & Frolov, Y.G. Aggregation Stability of Titanium-Dioxide Hydrosols. *Colloid Journal* 1994, **56**(2), 215-217.

269 Lee, D., Cohen, R.E. & Rubner, M.F. Heterostructured Magnetic Nanotubes. *Langmuir* 2006, **ASAP**.

270 Pastoriza-Santos, I., Koktysh, D.S., Mamedov, A.A., Giersig, M., Kotov, N.A. & Liz-Marzan, L.M. One-pot synthesis of Ag@TiO2 core-shell nanoparticles and their layer-by-layer assembly. *Langmuir* 2000, **16**(6), 2731-2735.

271 Fang, M.M., Kim, C.H., Saupe, G.B. *et al.* Layer-by-layer growth and condensation reactions of niobate and titanoniobate thin films. *Chemistry of Materials* 1999, **11**(6), 1526-1532.

272 Torquato, S., Truskett, T.M. & Debenedetti, P.G. Is random close packing of spheres well defined? *Physical Review Letters* 2000, **84**(10), 2064-2067.

273 Palik, E.D. *Handbook of Optical Constants of Solids*, Academic, New York, 1985. 565.

274 Yang, C.H., Grattoni, C.A., Muggeridge, A.H. & Zimmerman, R.W. A model for steady laminar flow through a deformable gel-coated channel. *Journal of Colloid and Interface Science* 2000, **226**(1), 105-111.

275 Yang, C.H., Grattoni, C.A., Muggeridge, A.H. & Zimmerman, R.W. Flow of water through channels filled with deformable polymer gels. *Journal of Colloid and Interface Science* 2002, **250**(2), 466-470.

276 Grattoni, C.A., Al-Sharji, H.H., Yang, C.H., Muggeridge, A.H. & Zimmerman, R.W. Rheology and permeability of crosslinked polyacrylamide gel. *Journal of Colloid and Interface Science* 2001, **240**(2), 601-607.

277 Mijnlieff, P.F. & Wiegel, F.W. Intrinsic-Viscosity and Friction Coefficient of Polymer-Molecules in Solution - Porous Sphere Model. *Journal of Polymer Science Part B-Polymer Physics* 1978, **16**(2), 245-263.

278 Stuart, M.A.C., Waajen, F.H.W.H., Cosgrove, T., Vincent, B. & Crowley, T.L. Hydrodynamic Thickness of Adsorbed Polymer Layers. *Macromolecules* 1984, **17**(9), 1825-1830.